



Calhoun: The NPS Institutional Archive
DSpace Repository

Theses and Dissertations

1. Thesis and Dissertation Collection, all items

2004-06

The role of cloud-top entertainment in coastal stratocumulus topped boundary layers

Eleuterio, Daniel Patrick.

<http://hdl.handle.net/10945/9937>

Downloaded from NPS Archive: Calhoun



Calhoun is a project of the Dudley Knox Library at NPS, furthering the precepts and goals of open government and government transparency. All information contained herein has been approved for release by the NPS Public Affairs Officer.

Dudley Knox Library / Naval Postgraduate School
411 Dyer Road / 1 University Circle
Monterey, California USA 93943

<http://www.nps.edu/library>



NAVAL POSTGRADUATE SCHOOL

MONTEREY, CALIFORNIA

DISSERTATION

**COASTAL STRATOCUMULUS TOPPED BOUNDARY
LAYERS AND THE ROLE OF CLOUD-TOP
ENTRAINMENT**

by

Daniel P. Eleuterio

June 2004

Dissertation Supervisor:

Qing Wang

Approved for public release; distribution is unlimited

THIS PAGE INTENTIONALLY LEFT BLANK

| | | | | |
|--|---|--|---|--|
| REPORT DOCUMENTATION PAGE | | | <i>Form Approved OMB No. 0704-0188</i> | |
| Public reporting burden for this collection of information is estimated to average 1 hour per response, including the time for reviewing instruction, searching existing data sources, gathering and maintaining the data needed, and completing and reviewing the collection of information. Send comments regarding this burden estimate or any other aspect of this collection of information, including suggestions for reducing this burden, to Washington headquarters Services, Directorate for Information Operations and Reports, 1215 Jefferson Davis Highway, Suite 1204, Arlington, VA 22202-4302, and to the Office of Management and Budget, Paperwork Reduction Project (0704-0188) Washington DC 20503. | | | | |
| 1. AGENCY USE ONLY (Leave blank) | | 2. REPORT DATE June 2004 | 3. REPORT TYPE AND DATES COVERED Ph.D. Dissertation | |
| 4. TITLE AND SUBTITLE: Title (Mix case letters) Coastal Stratocumulus Topped Boundary Layers And The Role Of Cloud-Top Entrainment | | | 5. FUNDING NUMBERS N0001403WX20542 N0001403WR20193 | |
| 6. AUTHOR(S) Daniel P. Eleuterio | | | | |
| 7. PERFORMING ORGANIZATION NAME(S) AND ADDRESS(ES) Naval Postgraduate School Monterey, CA 93943-5000 | | | 8. PERFORMING ORGANIZATION REPORT NUMBER | |
| 9. SPONSORING / MONITORING AGENCY NAME(S) AND ADDRESS(ES) N/A | | | 10. SPONSORING / MONITORING AGENCY REPORT NUMBER | |
| 11. SUPPLEMENTARY NOTES The views expressed in this thesis are those of the author and do not reflect the official policy or position of the Department of Defense or the U.S. Government. | | | | |
| 12a. DISTRIBUTION / AVAILABILITY STATEMENT Approved for public release; distribution is unlimited. | | | 12b. DISTRIBUTION CODE | |
| 13. ABSTRACT (maximum 200 words) Several issues associated with vertical grid resolution and the turbulence parameterization in mesoscale models are addressed in this study. Of particular concern is the issue of cloud top entrainment, the entrainment fluxes, and the impact entrainment has on boundary layer development and inversion strength. These issues are studied through careful analysis of in situ data and mesoscale simulations. In this study, we analyze observations to better understand the evolution of the marine boundary layer in various environmental conditions. We then explore the capability of the U.S. Navy's current Coupled Ocean-atmosphere Mesoscale Prediction System (COAMPS TM) using real case studies of summertime conditions along the California coast. We analyze the model's ability to accurately represent the boundary layer turbulence mixing at vertical resolutions feasible for operational prediction. Based on results from the above analysis, we modify the existing parameterizations towards more realistic representations of the cloud top processes and show these modifications improve COAMPS TM predictions in this regime. | | | | |
| 14. SUBJECT TERMS Entrainment, Cloud-Topped Marine Boundary Layer, Mesoscale Modeling, COAMPS. | | | 15. NUMBER OF PAGES 134 | |
| | | | 16. PRICE CODE | |
| 17. SECURITY CLASSIFICATION OF REPORT Unclassified | 18. SECURITY CLASSIFICATION OF THIS PAGE Unclassified | 19. SECURITY CLASSIFICATION OF ABSTRACT Unclassified | 20. LIMITATION OF ABSTRACT UL | |

NSN 7540-01-280-5500

Standard Form 298 (Rev. 2-89)

Prescribed by ANSI Std. Z39-18

THIS PAGE INTENTIONALLY LEFT BLANK

Approved for public release; distribution is unlimited

**THE ROLE OF CLOUD-TOP ENTRAINMENT IN COASTAL
STRATOCUMULUS TOPPED BOUNDARY LAYERS**

Daniel P. Eleuterio
Lieutenant Commander, United States Navy
B.A., Boston University, 1989
M.A., Boston University, 1990
M.S., Naval Postgraduate School, 1998

Submitted in partial fulfillment of the
requirements for the degree of

DOCTOR OF PHILOSOPHY IN METEOROLOGY

from the

**NAVAL POSTGRADUATE SCHOOL
June 2004**

Author:

Daniel P. Eleuterio

Approved by:

Qing Wang
Associate Professor of Meteorology
Dissertation Supervisor

Carlyle H. Wash
Professor of Meteorology

Wendell Nuss
Associate Professor of Meteorology

Doug Miller
Research Professor of Meteorology

Peter C. Chu
Professor of Oceanography

Shouping Wang
Naval Research Lab, Monterey, CA

Approved by:

Carlyle H. Wash, Chair, Department of Meteorology

Approved by:

Julie Filizetti, Associate Provost for Academic Affairs

THIS PAGE INTENTIONALLY LEFT BLANK

ABSTRACT

The ability of the U.S. Navy's Coupled Ocean-Atmosphere Mesoscale Prediction System (COAMPS™) to accurately forecast the height and structure of the Marine Boundary Layer (MBL) in the coastal zone is analyzed and compared to surface and aircraft observations from the Dynamics and Evolution of Coastal Stratus (DECS) field study conducted along the central coast of California from June, 16 to July 22, 1999. The stratus field was found to have significant mesoscale variability within 100 km of the coast due to interaction between the mean flow and the coastal terrain. This structure is consistent with general hydraulic flow theory and the development of a low level coastal jet; however the specific characteristics on any given day were very sensitive to flow direction, inversion height, and synoptic conditions. With some modifications, the model predicted the general evolution of these events with qualitative fidelity but was slow to dissipate the cloud and frequently produced surface fog vice stratus.

A consistent tendency was found in the model predictions of inversion heights 200-300 meters too low, weak inversion strengths, high integrated liquid water content, and weak buoyancy flux near the cloud top. These observed biases are consistent with underestimating the cloud top entrainment velocity and entrainment fluxes in the modeled boundary layer. An explicit entrainment parameterization was developed to better represent the sub-grid scale processes at cloud top and tested in the single column and three-dimensional versions of COAMPS™. The first step in this process is accurate determination of the inversion height. It was found that the current method of determining boundary layer height in COAMPS™ based on the bulk Richardson number frequently misdiagnosed the boundary layer height as occurring in the subcloud layer when a weakly stable surface-based inversion was present. Alternative methods based on the liquid water content and the liquid potential temperature gradient were tested and showed a more consistent diagnosis for the observed conditions in the marine boundary layer. The explicit entrainment parameterization was found to generally improve the boundary layer height and cloud liquid water content as compared to field observations, however the modeled boundary layer still exhibited a low bias and the entrainment velocity was higher than is generally expected from field studies for this regime.

THIS PAGE INTENTIONALLY LEFT BLANK

TABLE OF CONTENTS

| | | |
|-------------|---|-----------|
| I. | INTRODUCTION..... | 1 |
| A. | THE IMPORTANCE OF ACCURATE MARINE BOUNDARY LAYER FORECASTS TO THE U.S. NAVY..... | 1 |
| B. | GENERAL MODEL OF THE COASTAL MARINE BOUNDARY LAYER..... | 1 |
| C. | RECENT STUDIES IN IMPROVING MESOSCALE MODELING USING COAMPS™..... | 2 |
| D. | RESEARCH OBJECTIVES..... | 3 |
| II. | BACKGROUND | 7 |
| A. | CLOUD TOPPED BOUNDARY LAYERS | 7 |
| B. | THE SUMMERTIME CTBL STRUCTURE ALONG THE CALIFORNIA COAST | 11 |
| 1. | The Low Level Coastal Jet (LLCJ) | 11 |
| 2. | The Sea Breeze/ Mountain Valley Circulation (SBMV)..... | 16 |
| 3. | Coastal Fog and Stratus | 16 |
| C. | REPRESENTATION OF BOUNDARY LAYER TURBULENCE IN COAMPS™ | 20 |
| D. | PARAMETERIZATION OF ENTRAINMENT VELOCITY | 22 |
| III. | EVALUATION OF COAMPS™ FOR STRATOCUMULUS TOPPED BOUNDARY LAYERS USING OBSERVATIONS..... | 27 |
| A. | THE DECS FIELD EXPERIMENT AND DECS DATA ANALYSIS | 27 |
| 1. | Observations – The Dynamics and Evolution of Coastal Stratus (DECS) Field Study..... | 27 |
| B. | COAMPS™ SIMULATIONS FOR DECS CASES | 32 |
| 1. | Model Configuration | 32 |
| 2. | Modifications to the Calculation of In-cloud Buoyancy Flux | 36 |
| C. | COAMPS™ – DECS COMPARISON | 38 |
| IV. | DEFINING THE BOUNDARY LAYER HEIGHT..... | 61 |
| A. | OBJECTIVE | 61 |
| B. | COAMPS™ DIAGNOSTIC BOUNDARY LAYER HEIGHT..... | 62 |
| C. | COMPARISON OF OBSERVED AND SIMULATED BOUNDARY LAYER HEIGHT | 64 |
| D. | AN ALTERNATIVE METHOD FOR DIAGNOSING THE MODEL BOUNDARY LAYER HEIGHT | 66 |
| V. | EXPLICIT ENTRAINMENT PARAMETERIZATION..... | 71 |
| A. | EXPLICIT PARAMETERIZATION CONCEPT AND FORMULATION..... | 71 |
| B. | TESTING EEP IN SCM COAMPS™ | 77 |
| VI. | COAMPS™ SIMULATIONS WITH EXPLICIT ENTRAINMENT PARAMETERIZATION | 91 |
| A. | CASE STUDY CONTROL RUN SIMULATIONS..... | 91 |

| | | |
|------|--|-----|
| B. | CASE STUDY SIMULATIONS USING AN EXPLICIT ENTRAINMENT PARAMETERIZATION | 99 |
| 1. | Effects Of Explicit Entrainment On Simulating The Coastal Boundary Layer | 99 |
| 2. | Changes in the Resulting Turbulent Flux Profiles and Boundary Layer Structure | 105 |
| VII. | SUMMARY, CONCLUSIONS, AND RECOMMENDATIONS | 109 |
| A. | SUMMARY AND CONCLUSIONS | 109 |
| B. | RECOMMENDATIONS FOR FURTHER STUDY | 112 |
| | LIST OF REFERENCES | 113 |
| | INITIAL DISTRIBUTION LIST | 121 |

ACKNOWLEDGMENTS

This research received funding from the Office of Naval Research Award # N0001403WR20193 for Evaluation and Improvement of Boundary Layer Parameterizations in COAMPS using aircraft measurements and National Science Foundation Grant # ATM9900496. The author would like to thank Dr. Qing Wang for her invaluable assistance during this research. Her patience, wisdom, and guidance were essential to the completion of this effort. In addition, the author thanks Dr. Wendell Nuss for extensive discussions of coastal meteorology and synoptic and mesoscale forcing of the near shore boundary layer, Mr. Robert Creasey for his assistance with computing issues, Mr. Dick Lind for his assistance with surface observational mesonet data, Ms. Sue Chen, Dr. Douglas Miller, Dr. Shouping Wang and Dr. Kostantinos Rados for their assistance in using the COAMPSTM mesoscale model as a research tool, and Dr. Zhiqiu Gao and Dr. Kostantinos Rados for their assistance in the visualization of observational data and model output. Furthermore, Mr. John Kalogiros provided great assistance with calibration, processing, programming in MATLAB and visualization of the observational aircraft data. Lastly, the author would like to thank his wife, Raphaela, and daughters, Kaelyn and Anna for their sacrifices, patience, and support throughout the last three years, and my family and friends for their tremendous encouragement.

THIS PAGE INTENTIONALLY LEFT BLANK

I. INTRODUCTION

A. THE IMPORTANCE OF ACCURATE MARINE BOUNDARY LAYER FORECASTS TO THE U.S. NAVY

The Navy operates primarily in the Marine Atmospheric Boundary Layer (MABL). Accurate analysis and forecasting of sensible weather elements, especially those that impact aviation such as ceiling and visibility, are critical to safe and efficient operations. In addition, the large temperature and moisture gradients found in the MABL cause rapid and significant changes in refractive conditions that impact radars, electromagnetic and electro-optic surveillance and targeting, and communications. To better understand this environment, several recent field experiments have focused on the MABL cloud cover and dynamics. These include the First ISCCP Regional Experiment (FIRE; Cox et al. 1987), Dynamics and Chemistry of Marine Stratocumulus (DYCOMS I and II; Lenschow et al. 1988; Stevens et al. 2003a) in the California Bight, COAMPS™ Operational Satellite and Aircraft Test (COSAT; Wetzel et al. 2001) off the Oregon coast, Atlantic Stratocumulus Transition Experiment (ASTEX; Albrecht et al. 1995) in the northeast Atlantic near the Azores, and Development and Evolution of Coastal Stratocumulus (DECS; Kalogiros and Wang 2002) in Monterey Bay. Despite improved understanding of the relevant processes, accurate prediction of the MABL diurnal evolution is still limited by the scarcity of meteorological measurements over oceanic regions to correctly prescribe initial conditions and the lag between new understanding from field data and the appropriate realization of this understanding in numerical prediction schemes.

B. GENERAL MODEL OF THE COASTAL MARINE BOUNDARY LAYER

The marine boundary layer inversion height in the subtropical Eastern Pacific is the result of a balance between large-scale subsidence due to the semi-permanent subtropical anticyclones and turbulent transport. Turbulent eddies result in entrainment of free atmosphere air into the boundary layer, which can lead to boundary layer growth and weakening of the stable inversion at the boundary layer top if the free atmosphere

above the entrainment zone is weakly stratified. Because surface sensible heat fluxes are small in the region of cold ocean boundary currents, surface shear, surface moisture flux, in-cloud latent heat release, and cloud-top radiative cooling largely generate the turbulence in the mixed layer. Surface buoyancy flux is primarily generated by moisture flux, and sensible heat flux is usually small and may even be negative. Additional factors in the coastal zone are less well understood and include the role of upwelling and mesoscale variability in the sea surface temperatures, the role of shear at and above cloud top due to the presence of a low level coastal jet, the quantitative effects on entrainment rate due to evaporative cooling as the cloud layer mixes with dry inversion air near cloud top, and the impact of sea breeze and coastal jet circulations on cloud evolution, microphysics and drizzle. Furthermore, local divergence patterns can be greatly affected by flow interaction with the coastal topography leading to complex and diurnally varying mesoscale structure in the inversion strength and height. The rapid change in surface characteristics at the coast also leads to complex coastal circulations and thermal internal boundary layers. This research will focus in particular on the role of cloud-top entrainment and its representation in mesoscale models, the interaction between cloud-top processes and mechanisms particular to the coastal zone such as coastal jet-related vertical shear and on horizontal variability in the forcing and resultant boundary layer structure in the coastal region.

C. RECENT STUDIES IN IMPROVING MESOSCALE MODELING USING COAMPS™

Several researchers supported by the ONR and other agencies in the Department of Defense (DoD) are working on improving the numerical representation in COAMPS™ of various mesoscale aspects of the MABL such as the surface layer parameterization (Wang 2002, Thompson 2002), the radiation scheme (Kong 2002), the cloud microphysics and drizzle parameterizations (Mechem and Kogan 2003), and the turbulence parameterization (Whisenant 2003). Case studies of the Cloud-Topped marine Boundary Layer (CTBL) structure (e.g. Haack and Burk 2001; Burk et al. 2003) and the numerical representation of CTBL (Wetzel et al. 2001) show reasonable

qualitative skill but still do not represent the MABL with sufficient fidelity for operational prediction. Kong (2002) specifically investigated the predictive skill of COAMPS™ for a point verification of stratus and found skill in predicting dissipation driven by short wave radiation, but required very high resolution of 50 m in the vertical and 2 km in the horizontal, a modified radiation scheme, and an auto-conversion threshold of 0.5 g/ kg to force drizzle processes. Furthermore, none of these modifications were evaluated for impact to predictive skill in other geographic areas or regimes. Nowcasting efforts combining mesoscale numerical prediction models with climatology averaged initial structure nontraditional data sources (Leidner et al. 2001) and rules based expert systems (Hilliker and Fritsch 1999), have shown promise but require local training observational data sets and are not suitable for Naval use because the area of interest in Naval operations changes rapidly. A preferable solution that we pursue in this study is to improve the model representation of dynamic processes such as cloud-top entrainment in a physically consistent and numerically efficient way.

D. RESEARCH OBJECTIVES

The overall objective of this study is to better understand the coastal marine stratocumulus evolution and its interaction with the complex flow field resulting from interaction with the adjacent terrain. Particular emphasis has been placed on the role of cloud-top entrainment in this development. This study theorizes that entrainment of warm, dry inversion air into the cloud top driven by cloud-top turbulent processes has a significant impact on the mesoscale structure and evolution of the CTBL. This process occurs at vertical scales of order 10 meters, which is below typical vertical resolution in operational forecast models. It is theorized that better representation of the entrainment processes and resulting dynamic fluxes will improve operational mesoscale prediction. Wetzel et al. (2001), Haack and Burk (2001) and preliminary data from DECS and DYCOMS II have indicated that, at resolutions usable for operational prediction, COAMPS™ reproduces the general structure and trends in the CTBL but the marine boundary layer is too shallow, has too thick a cloud layer, and has liquid water path (LWP) values 3-4 times larger than expected. The forecast model in their study produced

reasonable area coverage but Liquid Water Path (LWP) was 3-4 times larger than observations derived from satellite data. The observed model bias of high LWP could result from either lack of precipitation processes or under-represented cloud top entrainment of warm dry inversion air while the shallowness of the layer is likely due to under-prediction of the turbulent entrainment rate. Mechem and Kogan (2003) demonstrated that high vertical (~ 50 m) and horizontal (2 km) resolution simulations with a 2-moment drizzle scheme (Khairoutdinov and Kogan 2000) can produce a CTBL qualitatively similar in vertical structure, diurnal variability, horizontal inhomogeneity to an observed case and can reproduce drizzle-induced stratocumulus to cumulus transition. Preliminary analysis in this study indicates that, when the auto-conversion threshold for cloud liquid water conversion to drizzle is adjusted in the lower levels from the default value of 1.0 g kg^{-1} suitable for convective rain, to a value of 0.5 g kg^{-1} for marine stratus as recommended by Mechem and Kogan (2003), the model LWC and surface accumulated precipitation amounts better match the observations. Other aspects of the boundary layer structure such as inversion height and strength are not affected and the LWC is generally 20-25% higher than observations rather than the 300-400% found in the COSAT experiment. This study examines if an explicit entrainment parameterization which better represents the effects of sub-grid scale (SGS) processes at cloud top will result in a modeled CTBL structure that more closely resembles the observed CTBL structure.

In support of the overall objective, this research analyzed the observed boundary layer structure during the months of June and July 1999 in the DECS dataset as compared to model simulations under a variety of synoptic conditions and mesoscale coastal processes. Observed and simulated turbulent fluxes and thermodynamic forcing were examined with respect to diurnal evolution and horizontal variability of the CTBL in the coastal zone. An explicit entrainment parameterization was implemented following Grenier and Bretherton (2001) and the resulting fluxes and boundary layer structure were compared to observed and modeled fluxes in the current method used in COAMPSTM.

Chapter II summarizes the relevant background and research papers related to this study; Chapter III discusses methodology, observational datasets, and general control run

model results; Chapter IV discusses methods of identifying the boundary layer height in COAMPSTM and its role in parameterizing entrainment; Chapter V discusses the development of an explicit entrainment parameterization and single column model (SCM) results; Chapter VI discusses three dimensional results, and Chapter VII summarizes our findings and provides recommendations for future research.

THIS PAGE INTENTIONALLY LEFT BLANK

II. BACKGROUND

A. CLOUD TOPPED BOUNDARY LAYERS

Modeling of the CTBL in COAMPSTM is the main focus of this research, thus it is important to understand the physical processes that generate and maintain turbulence and result in the observed structure and evolution. The marine atmospheric boundary layer (MABL) is the lowest (~10%) part of the troposphere that is directly affected by ocean surface forcing on a time scale of order 1 hour or less (Stull 1988). The MABL is comprised of the interfacial layer, where molecular diffusion dominates (order ~1 cm), the surface layer, (order ~10% of MABL height) where turbulent fluxes are nearly constant with height, and the outer layer where turbulent fluxes are linear with height if well mixed. A balance between turbulent mixing and large-scale subsidence determines the depth of the MABL. In the case of the eastern subtropical ocean regions, the subtropical high produces a permanent subsidence inversion and generally northerly flow over increasing SST. This creates a nearly permanent MABL structure of increasing boundary layer heights southward and westward from the coast. In summertime, the inversion base is frequently above the lifting condensation level resulting in persistent large-scale sheets of stratus and stratocumulus which have important effects on the total global radiation budget as well as significant climate and economic impacts on coastal communities. Burk and Thompson (1996) and Dorman et al. (2000) provide good descriptions of the summertime MABL along the U.S. West coast.

Stratiform low cloud is a common feature through most of the world's oceans. Marine stratocumulus CTBL in particular are often observed along western continental shelves at the eastern edge of the summertime subtropical high. As discussed in Klein and Hartmann (1993), from a climate perspective, marine stratiform clouds can be classed into three basic types as follows. Subtropical CTBL form primarily in summer over cold western boundary currents on the east side of subtropical highs and are maintained by a balance between large-scale subsidence and convection driven by cloud top radiative cooling. Midlatitude CTBL form in winter as cold continental air flows over warm western boundary currents. Arctic stratus forms from radiative cooling of

moist air entering the Arctic from the subpolar regions. This study will primarily focus on subtropical stratus, although the same boundary layer model can be used to describe the other types if parameterizations are kept physically based and consistent. As depicted schematically in Figure 2.1 from Atkinson and Zhang (1996), the general mixed layer structure in the cloud-topped case is primarily a balance between downward adiabatic warming from large-scale subsidence, cloud-top radiative cooling, cloud dynamics and thermodynamics, and weak surface forcing.

As discussed in Paluch and Lenschow (1991) based on FIRE data, the stratocumulus CTBL has a more complex structure than the typical clear convective boundary layer. This is because of additional mechanisms affecting the turbulence structure due to thermodynamic effects (primarily water phase changes), longwave and shortwave radiative effects associated with the cloud layer, and heat and moisture transport by drizzle falling and re-evaporation. The inversion at the cloud top tends to be sharper in both the virtual potential temperature (θ_v) and total water mixing ratio (q_t) than in clear boundary layers due to enhanced turbulent mixing in the upper part of the boundary layer driven mainly by cloud-top radiative cooling. This longwave radiative cooling and shortwave daytime heating modify the in-cloud thermodynamic profile and produce turbulence, although the net effect is also modified by evaporative cooling or sensible heating as warm, dry inversion air is entrained and mixed with cloudy parcels. Some researchers have proposed that this entrainment mixing can lead to buoyancy reversal and cloud dissipation through Cloud Top Entrainment Instability (CTEI) (Randall 1980, Deardorff 1980) if the buoyancy jump condition is sufficiently large, although the exact criteria for CTEI to occur is still a subject of active research. In the absence of subsidence, entrainment will tend to deepen the boundary layer by mixing free atmosphere air into the layer and increasing the mass. In-cloud radiative warming or sub-cloud evaporative cooling due to drizzle can also lead to less well-mixed or “decoupled” boundary layers which can lead to cloud dissipation or pooling of heat and moisture in the surface layer and shallow cumulus convection.

Drizzle is frequently observed in CTBL. As discussed in Jiang et al. (2002), the role of drizzle in CTBL structure is quite variable and can lead to cloud base lowering,

cloud dissipation, or stratocumulus to cumulus transition. When drizzle reaches the surface, the entire sub-cloud layer is evaporatively cooled and moistened, resulting in reduced surface buoyancy flux. This can increase the surface temperature gradient and result in transition from stratus to shallow convection and cumulus transition. For cases where the precipitation remains aloft (virga), the effect is variable, with lightly drizzling ($\sim 0.1 \text{ mm day}^{-1}$) cases becoming stabilized and decoupled from the surface, possibly leading to daytime dissipation, and heavier rates ($\sim 0.5 \text{ mm day}^{-1}$) increasing sub-cloud instability thus increasing development of penetrating cumulus, turbulence generation, and entrainment (Wang and Wang 1994). These effects are also dependent on the large-scale subsidence and the aerosol loading (e.g. Twomey 1977, Albrecht 1989, Penner et al. 2001).

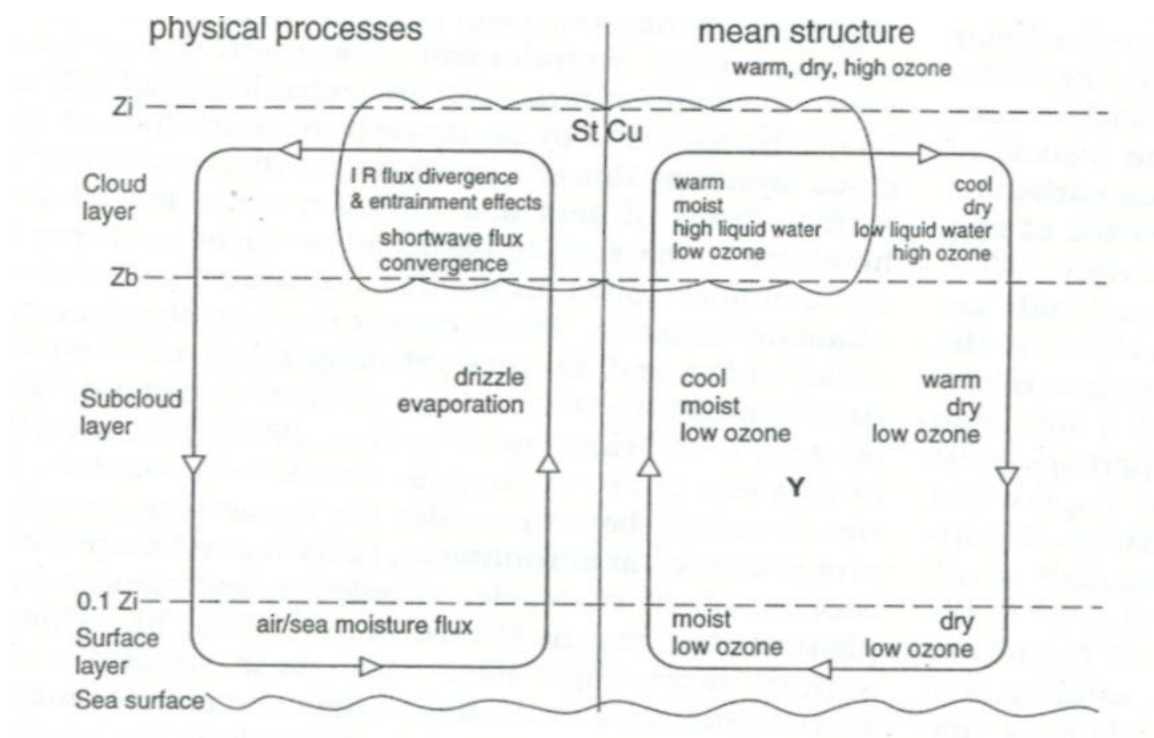


Figure 2.1. Primary physical processes in StCu topped boundary layers. From Atkinson and Zhang (1996).

B. THE SUMMERTIME CTBL STRUCTURE ALONG THE CALIFORNIA COAST

1. The Low Level Coastal Jet (LLCJ)

The California coastal region in particular has been studied extensively through both field observations and modeling studies as a particular case of cloud-topped boundary layers. As described in Beardsley et al. (1987) and Burk and Thompson (1996), a primary feature of the summertime California coastal region is a persistent, coast-parallel northerly low level jet (LLCJ) that forms due to the cross-coast pressure gradient between the East Pacific subtropical high, Sonoran Desert thermal low, capping inversion, and coastal mountain range. As depicted in Figures 2.2 and 2.3, the horizontal wind speed increases with decreasing height and coastward distance, as would be expected from thermal wind considerations, to a maximum at the top of the boundary layer inversion, and then decreases due to turbulent diffusion to the surface. This results in an inversion that slopes more sharply in the inner coastal zone than the gradual westward and southward slope expected from synoptic level considerations and a distinct diurnal character due to additional diurnal temperature fluctuations over land. This structure is well represented in COAMPSTM, as can be seen in Figure 2.4 of day and night East-West cross-sections of the boundary layer at 37.1 N, which is across the southern part of Monterey Bay. As discussed in Burk and Thompson (1996), Cui et al. (1998), Dorman et al. (2000) and elsewhere, the exact mechanisms causing the boundary layer and jet structure and spatial and temporal variability are still areas of active research, however a proper specification of the coastal mountains and the Sierra Nevada are critical to the structure of the MABL and LLCJ close to the coast (Cui et al. 1998). The dynamic impact of the marine stratocumulus on the wind field has received little attention, but is potentially an important factor as it's a common characteristic in this regime. In addition to the broader jet feature that often extends to 200-300 km from shore, the inner coastal region, defined here as less than 100 km off shore, has an additional mesoscale structure of relative maximums and minimums in wind speed and boundary layer height respectively downstream of prominent points. These are associated with regions of increased horizontal divergence and forced subsidence as depicted in Figure 2.5. The reverse structure is also seen upstream of these points. The four dimensional structure of

these features is difficult to observe directly but is well resolved in operational mesoscale models as discussed in Burk and Thompson (1996) and Koracin and Dorman (2001). The model simulations show reasonable agreement with surface observations in horizontal extent, magnitude, and diurnal variability with the observed surface wind maximum close to 0500 UTC, just after sunset. Based on mesoscale model simulations and observations, Koracin and Dorman (2001) found the mesoscale low level coastal jet (MLLCJ), embedded within the broader LLCJ feature, can largely be described by shallow water hydraulic flow theory, with the mesoscale variability driven by flow along a complex coastline constrained by the thermally induced cross-coast gradient. Bends in the coast result in low wind, high boundary layer compression bulges upstream from points, high wind, low boundary layer expansion fans downstream in the capes, and transcritical flow further downstream where the flow recovers to the gradient value. Although it's been noticed that the persistence or dissipation of coastal stratus is often correlated with this mesoscale divergence and vertical wind shear pattern, there is not much in the literature about the exact mechanisms involved.

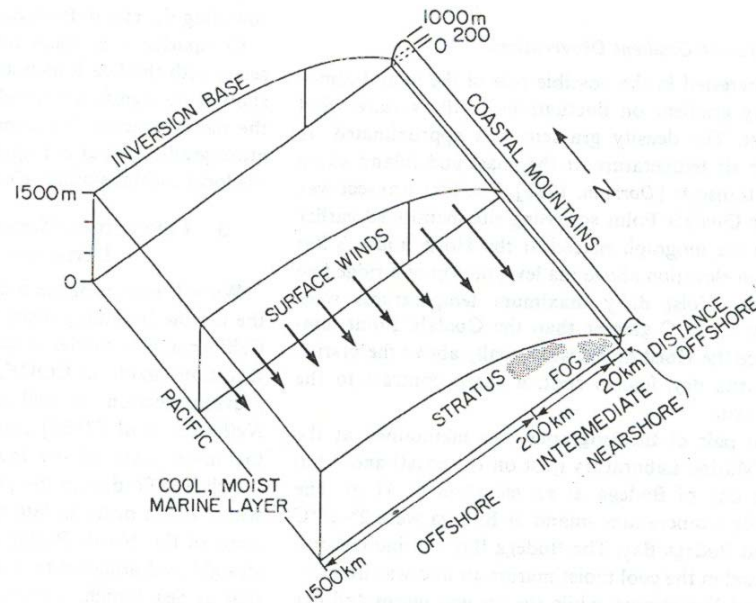


Figure 2.2. Basic structure of the CTBL along the California coast. From Beardsley et al. (1987).

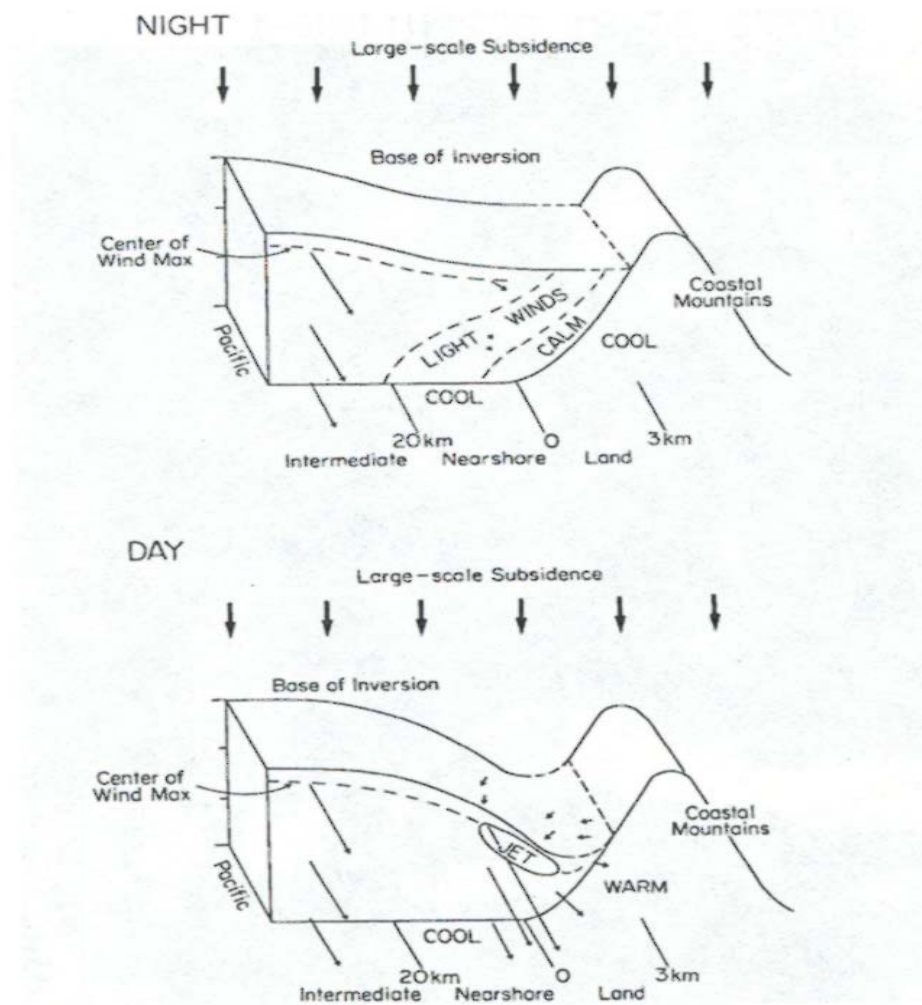


Figure 2.3. Diurnal variability in the inversion structure and vertical wind profile along the summertime California coast. From Beardsley et al. (1987).

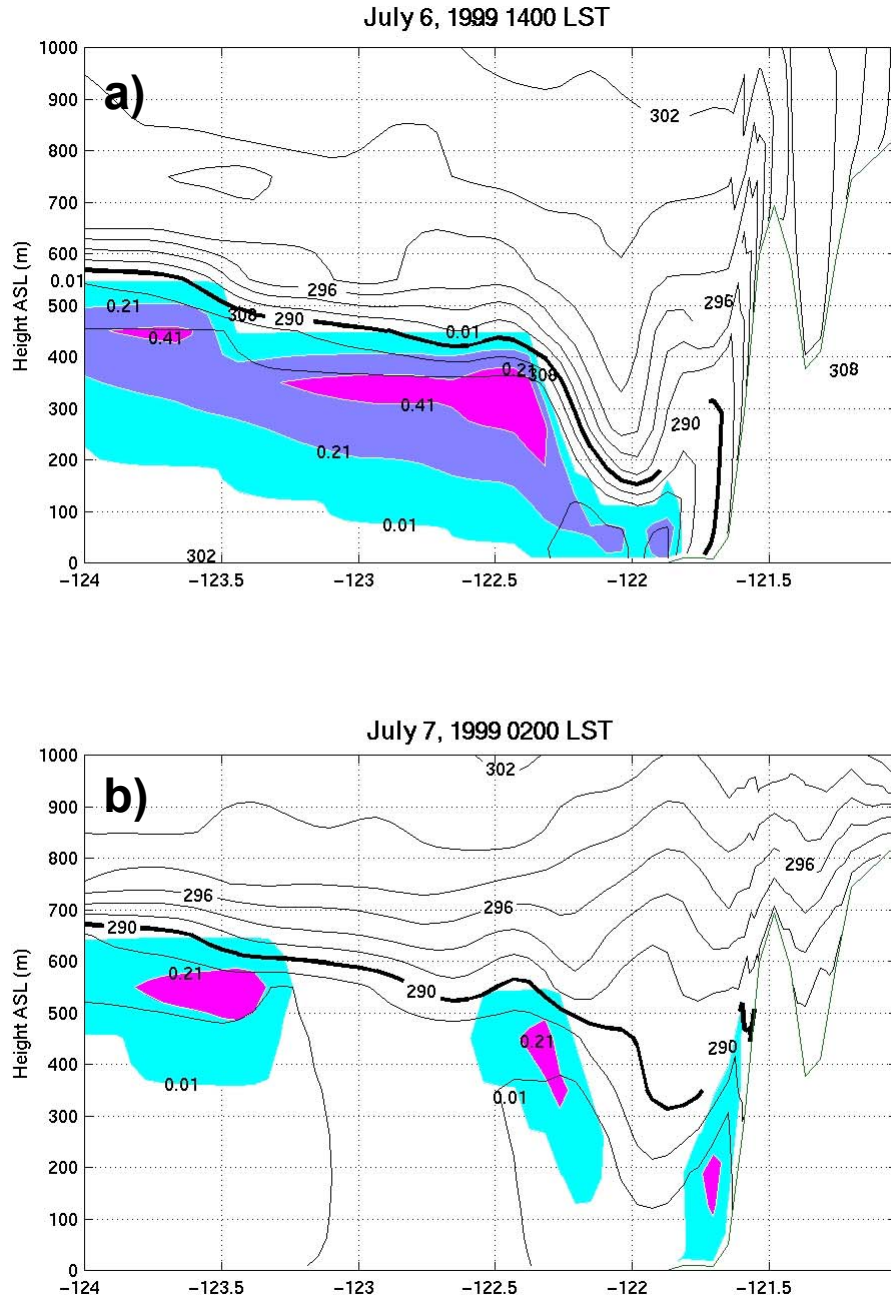


Figure 2.4. Simulated diurnal virtual potential temperature (K) and liquid water mixing ratio (g kg^{-1}) contours in an East-West cross-section from Monterey Bay, CA (36.71 N) (between Pigeon Point and Point Sur) for July 6-7, 1999, a day with a strong LLCJ. Note the a) daytime shallowing and b) nighttime deepening of the boundary layer at approximately 122 W consistent with the convergence/divergence pattern in Figure 2.4.

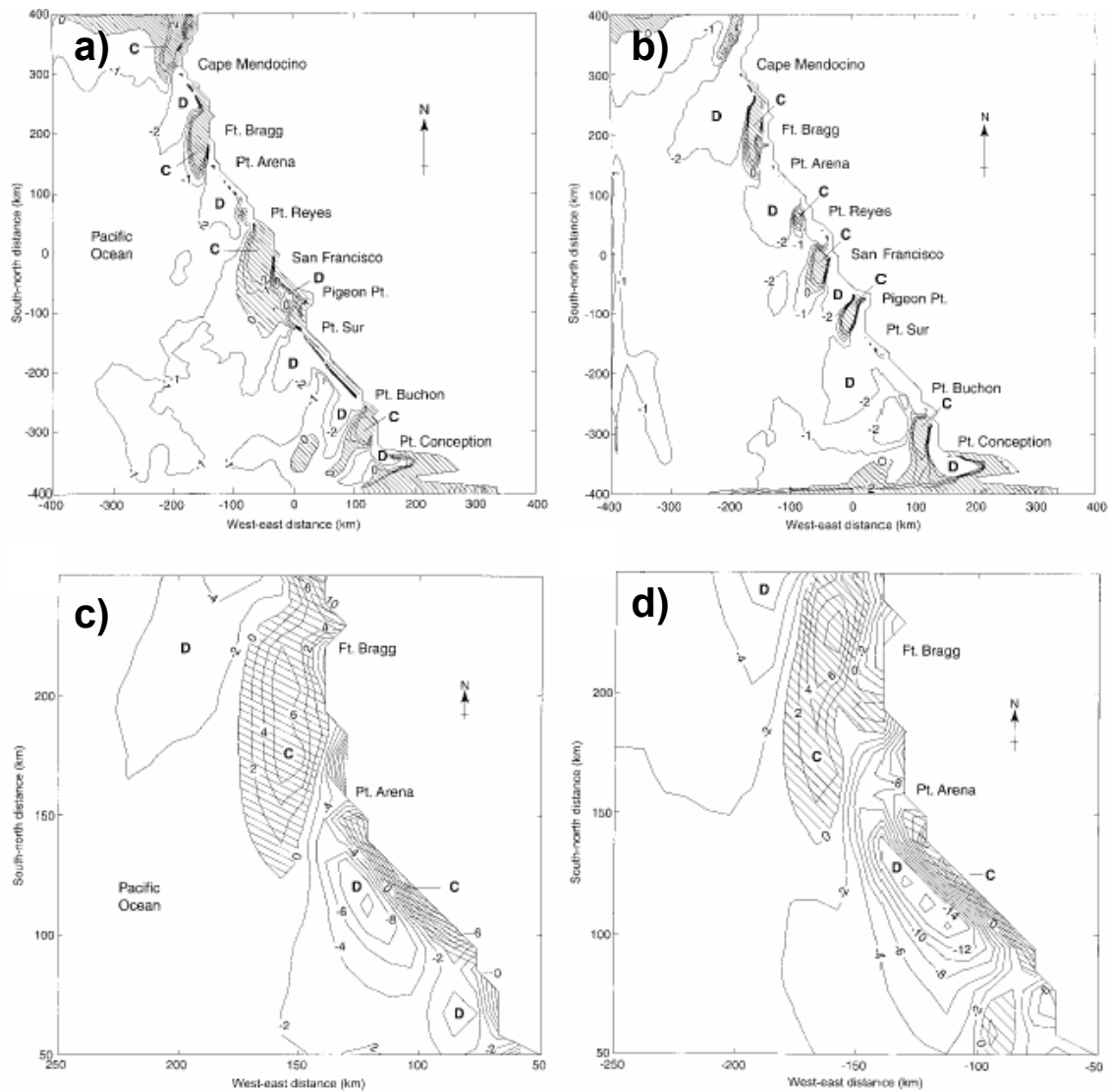


Figure 2.5. Simulated diurnal boundary layer height and divergence pattern along the California coast. Panels a) and c) are daytime (1400 LST) and b) and d) are nighttime (0200 LST). Adapted from Koracin and Dorman (2001).

2. The Sea Breeze/ Mountain Valley Circulation (SBMV)

In addition to a spatially and diurnally varying LLCJ, several points along the California coast develop a robust sea breeze mountain valley circulation (SBMV) within approximately 100 km of the coast with an increasing diurnal amplitude shoreward (Kindle et al. 2002). This circulation is particularly prominent in breaks in the coastal mountains such as at San Francisco, Monterey Bay (Banta et al. 1993) and the Los Angeles Basin (Lu and Turco 1994). The SBMV differs in timing and structure from a classic sea breeze front in that upslope flow and elevated solar driven heating in complex terrain can change the timing and orientation of the flow. Lidar studies by Banta et al. (1993) of the Monterey Bay showed that the SBMV grew during the late morning hours similar to other sea breeze regions, but grew much faster over land than over the cold coastal waters. The SBMV also varied from a classic sea breeze in that there was little change in vertical velocity at the sea breeze front due to strong synoptic subsidence extending to at least 1 km, and there was little evidence of a return flow aloft towards the ocean. Horizontal extent seaward seems to be on the order of 30-50 km, which is also supported by model and buoy data as discussed in Kindle et al. (2002) using buoy data and COAMPSTTM simulations to explore the surface wind short and long period variability over Monterey Bay. The subsiding return flow of this sea breeze circulation contributes to the observed lowering of the inversion height near the coast in late afternoon but does not independently cause the observed pattern as the convergence pattern remains robust over a longer diurnal period and is also observed downstream of points such as Point Sur which do not develop a clear SBMV.

3. Coastal Fog and Stratus

Several studies of fog and stratus have been done in Northern California due to the critical operational and economic impact low ceilings and visibility has on marine and aviation communities. The impact on flight scheduling at San Francisco International airport (SFO) is discussed in Hilliker and Fritsch (1999) which, as seen in Figure 2.6, found a relative maximum in occurrence of low stratus and fog at SFO at 1500 UTC (just after sunrise) and the greatest decrease in frequency of occurrence 1-4 hours afterwards,

indicating the most likely time of dissipation leading to a relative minimum at 2300 UTC (mid afternoon). Figure 2.7 depicts a typical diurnal variation in the large-scale distribution. From a prediction perspective, few studies have attempted to distinguish between the dominant physical mechanisms underlying the evolution of the inner coastal stratus, inner coastal surface fog, outer coastal stratus, and valley fog. Koracin et al. (2001) examined the transition between stratus and fog over water from a Lagrangian perspective. They determined that fog forms in response to a relatively long preconditioning of the marine boundary layer, with cloud top cooling as the primary mixing mechanism for the lifting of the inversion resulting in fog developing from stratus, and subsidence as the predominant cause of lowering of the inversion base resulting in stratus transitioning to fog. As will be discussed in Chapter III, it was found that in order to properly model the CTBL, the long preconditioning required for the CTBL to develop and reach semi-equilibrium requires an upstream model domain on the order of 200-300 km and a 36-48 hour data assimilation period (“warm start”) to accurately depict the CTBL.

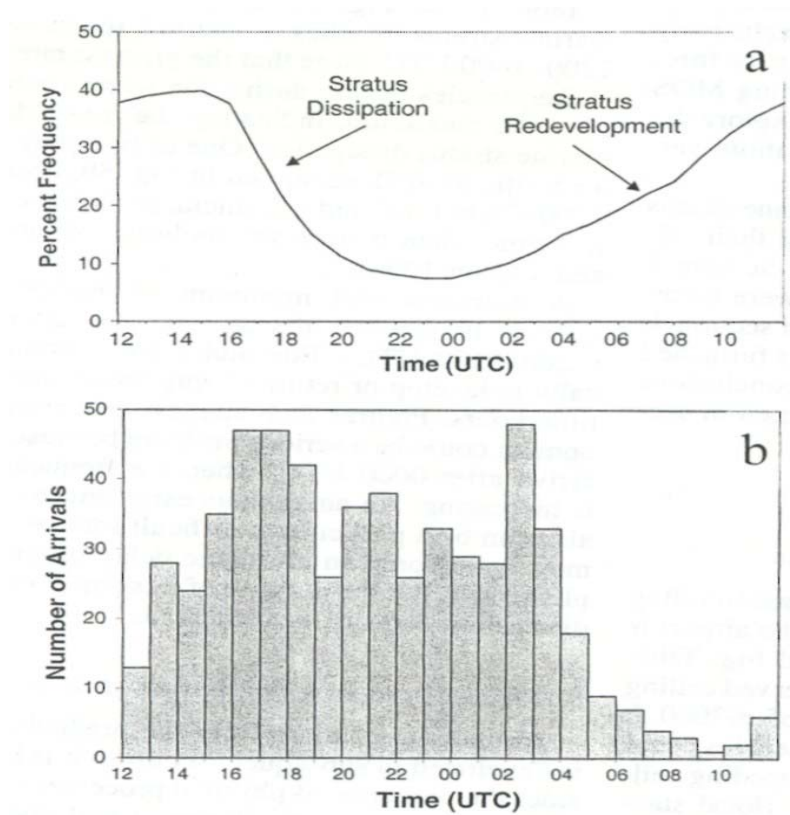


Figure 2.6. Diurnal occurrence of a) ceilings less than 914 m at SFO from May to October and b) corresponding hourly arrival demand of air traffic. From Hilliker and Fritsch (1999).

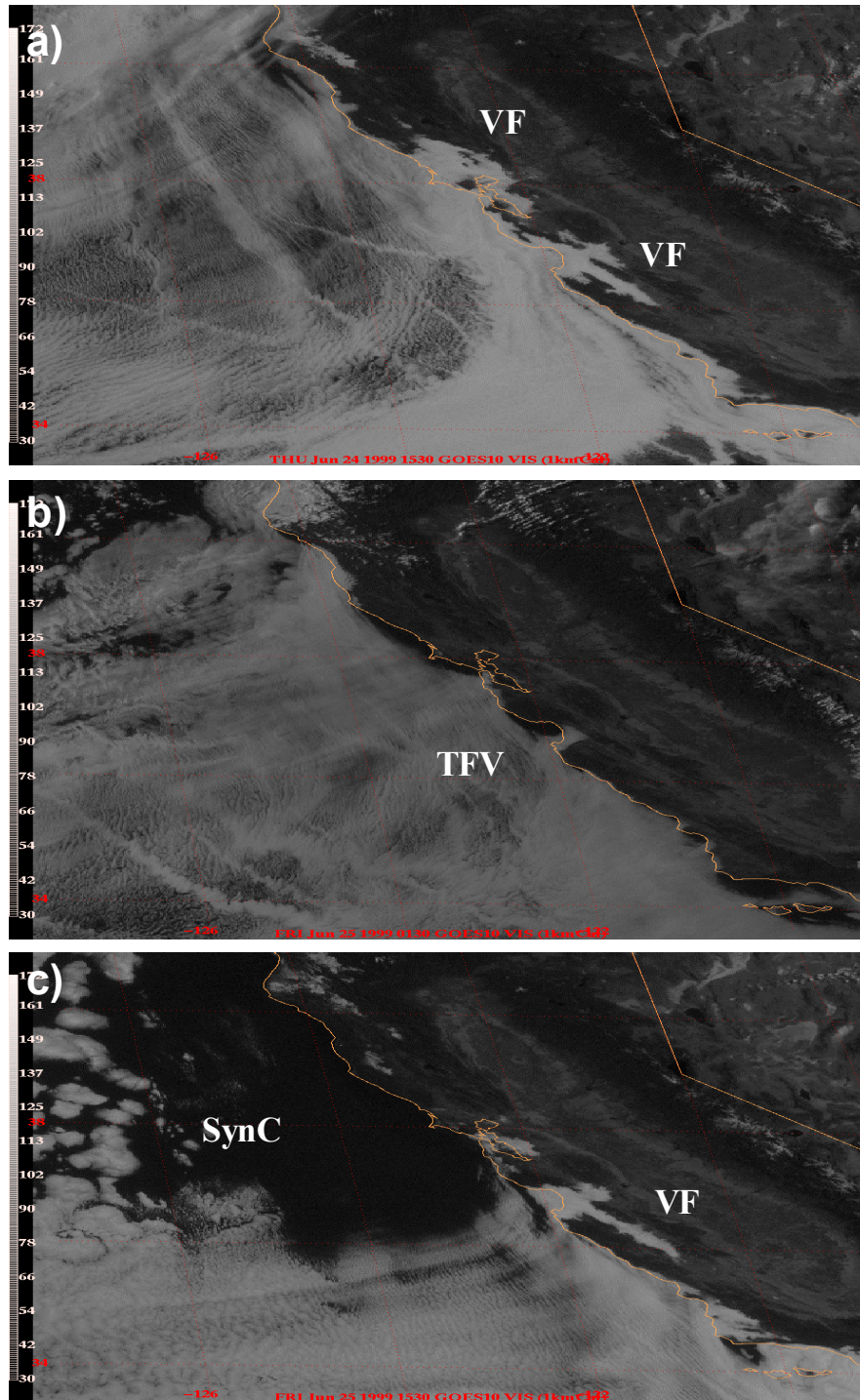


Figure 2.7. Typical diurnal pattern in summertime coastal cloud distribution. Note nocturnal development and daytime dissipation of valley fog (VF), terrain forced coastal clearing/ persistence around points (TFV) and broader, synoptically-driven clearing (SynC) over water that still has a coastal characteristic. Figures a) and c) are early morning at 1530 UTC and figure b) is at 0130 UTC late afternoon.

C. REPRESENTATION OF BOUNDARY LAYER TURBULENCE IN COAMPSTM

In numerical models, the choice of parameterization scheme for turbulent flux calculation is restricted by available computer power and time limitations in producing a needed forecast product. Mellor and Yamada (1974) developed a hierarchy of turbulence closure models, ranging from a level 1 model (the smallest equation set with the largest number of assumptions) to a level 4 model (the largest equation set with the smallest number of assumptions). They tested these equation sets and determined that the level 2 model performed adequately, with additional improvement going to level 3 that is worth the extra computational effort. However the level 4 model, with its 8 additional equations, showed little improvement over level 3 for the increased computational effort. Mellor and Yamada (1982) further modified their level 3 model, known as the level 2.5 model, which eliminates the prognostic equation for temperature. The result reduces the computational effort with negligible effect to the prediction ability as compared to a level 3 model. COAMPSTM uses Mellor-Yamada level 2.5 for PBL turbulent mixing and diffusion calculations. In this scheme, entrainment at the upper boundary is implicit. The vertical profiles of state variables are modified by the TKE profile through the turbulent fluxes of heat, moisture and momentum.

COAMPSTM uses a turbulence closure model based on the Mellor and Yamada (1982) 2.5-level scheme (Hodur, 1997). Following Mellor and Yamada (1982) and Chen et al. (2003), the one dimensional TKE budget equation is generally of the form:

$$\frac{d\bar{e}}{dt} + \frac{\partial}{\partial z}(\bar{w'e'}) = -\bar{w'u'} \frac{\partial U}{\partial z} - \bar{w'v'} \frac{\partial V}{\partial z} + \beta g \bar{w'\theta'} - \frac{1}{\rho} \frac{\partial}{\partial z}(\bar{w'p'}) - \varepsilon \quad (2.1)$$

which is parameterized in COAMPSTM as

$$\frac{\partial \bar{e}}{\partial t} - \frac{\partial}{\partial z} (K_e \frac{\partial \bar{e}}{\partial z}) = K_M \left(\frac{\partial U}{\partial z} \right)^2 + K_M \left(\frac{\partial V}{\partial z} \right)^2 - \beta g K_H \frac{\partial \theta}{\partial z} - \frac{(2\bar{e})^{3/2}}{\Lambda} + \left(U \frac{\partial \bar{e}}{\partial x} + V \frac{\partial \bar{e}}{\partial y} \right) \quad (2.2)$$

where e is the TKE, U , V are the horizontal wind speed, K_e , K_H and K_M are the eddy diffusivity constants for TKE, heat and momentum, β is the coefficient of thermal expansion, θ is the potential temperature, and Λ is an empirical dissipation length scale.

In this formulation the prognostic variable, TKE, is determined from the TKE budget equation where the production terms are a function of turbulent fluxes. These fluxes are diagnosed from the vertical gradient of the scalar quantity times the eddy diffusivity, given by

$$K_{H,M,e} = S_{H,M,e} l \sqrt{2e} \quad (2.3)$$

where $S_{H,M}$ are polynomial functions of the flux Richardson number, S_e is a constant and l is the master length scale. The TKE equation is solved explicitly using a tri-diagonal technique to invert the coefficient matrix. Various length scales (e.g. Blackadar 1962, Therry and LaCarrère 1983) are available; however the default master length scale follows Blackadar (1962) such that for the neutral or convective boundary layer it increases with height from a minimum of 5 meters near the surface to a maximum at the boundary layer top, and then returns to the minimum value.

$$l = \frac{kz}{1 + \frac{kz}{\alpha \frac{\int zedz}{\int edz}}} \quad (2.4)$$

where k is the von Karaman constant, z is the elevation, and α is a stability function based on z/L . Some turbulence can be generated at the upper interface in this scheme by wind shear and cloud-generated buoyancy flux between grid levels, and this indirectly represents the entrainment effects. This approach implicitly represents the entrainment mixing across the upper interface at grid resolution with the calculation of turbulent fluxes based on the eddy diffusivity and the vertical gradient of the scalar quantity. This approach can partially represent the mixing across the interface; however this implicit entrainment at vertical resolutions on the order of 100 meters does not accurately represent the sharper gradient in the entrainment zone, which is generally sub-grid scale of order 10 meters. It is not yet feasible to run operational prediction models at very high vertical resolutions, and LES studies indicate that, even at LES resolutions, sub-grid scale (SGS) processes may still cause problems with accurately determining the entrainment velocity (Moeng 2000; Stevens 2002). Using an adaptive grid scheme to concentrate

levels in a diagnosed entrainment zone (Fiedler 2002) showed some advantage in increasing vertical resolution without large computational expense, but resulted in no improvement in predicting entrainment velocity at resolutions typical for operational weather prediction.

At least for the near future, improvement in mesoscale prediction models of the CTBL will require more efficient representation of the sub-grid scale turbulent transport near the cloud top. It is hypothesized that this more representative turbulent mixing will then feedback on thermodynamic prognostic equations and the cloud microphysics scheme to better reflect the observed CTBL in terms of cloud height, thickness, and LWP.

D. PARAMETERIZATION OF ENTRAINMENT VELOCITY

As discussed in Lilly (2002b) and Stevens et. al (2003b) the PBL parameterizations in General Circulation Models (GCM) are usually at relatively coarse vertical resolutions and often explicitly solve for boundary layer height and therefore must explicitly represent entrainment. The motivation for much of the recent work in parameterizing entrainment has been to improve the ability of GCM's to accurately diagnose entrainment velocity with an explicit approach at coarse vertical grid spacing. This is required to represent a realistic CTBL and in particular stratocumulus to cumulus transition, which is important to the global radiative budget and therefore the applicability of GCM's to climate studies. As discussed in Lilly (2002a, 2002b), the key to appropriately parameterizing the entrainment rate is to represent the relative contributions to the entrainment velocity (W_e) of turbulent transport due to surface fluxes and the buoyancy flux generated by cloud. Comparison to observations and representation of the net effective entrainment is complicated in numerical models by the horizontal grid resolution in which the real atmosphere may be only partially cloudy, cloud top may undulate within a grid box, and the interface may only be tens of meters thick or less while the model vertical resolution is typically an order of magnitude larger. Stevens (2002) compares several recent entrainment rules proposed by Lock (2000), Turton and Nicholls (1987), Konor and Arakawa (2001), Moeng (2000), and Lilly

(2002a) and found that entrainment rules differ by as much as a factor of 2 or 3, even when based on identical LES data, and that the coarse vertical resolutions found in GCM and operational forecast models cannot currently satisfactorily represent the CTBL regime. Following Stevens (2002), Equation 2.5 describes the general form of all of these rules and they differ primarily in how they account for buoyancy reversal, shear and moist thermodynamic effects. Most of the recent rules can be expressed in the form

$$We = A\left(\frac{W}{\Delta b}\right) + D \quad (2.5)$$

where A is an efficiency parameter to describe the energy available to drive turbulence, part of which works against the stratification, W is the rate of work based on the forcing from the cloud-top buoyancy flux, radiative flux and total water flux, Δb is the stability condition, or “jump condition” at the inversion, and D describes forcing from diabatic processes such as radiative cooling above the inversion, drizzle, and other processes. The various rules treat each of these terms slightly differently and also specify different empirical constants depending on the observations and LES studies used in their development and the environmental conditions where their assumptions and constraints remain valid.

As discussed in Grenier and Bretherton (2001), the entrainment velocity can be diagnosed fairly simply by applying a local closure such as the Turner-Deardorff scheme (Deardorff 1972, 1976) given by

$$We = A\left(\frac{U}{Ri}\right) = A\frac{U^3}{L\Delta_i b} \quad (2.6)$$

where Ri is the bulk Richardson number, $Ri=U^2/L\Delta_i b$, L is the velocity scale, U is the horizontal wind shear, and $\Delta_i b$ is the jump condition across the inversion. In the common notation of Equation 2.5, the Turner-Deardorff closure in Equation 2.6 becomes a simple ratio between the turbulent mixing and the inversion strength with D=0 as shown in Equation 2.7.

$$We = A_L \frac{e^{3/2}}{l^i \Delta_i b} \quad (2.7)$$

A_L is the entrainment efficiency, e is the TKE, and l^i is the mixing length. The turbulent mixing can be defined as the TKE at the grid level at inversion base or as a vertical integral of the mixed layer TKE. This parameterization does not account for variations in the in-cloud conditions such as droplet size that would affect the rate of evaporative cooling due to mixing between inversion air and cloud parcels, the role of wind shear above the cloud-top, or the additional radiative or moist-thermodynamic forcing due to the presence of cloud. Another approach by Lilly (2002b), given by Equation 2.8 attempts to better represent the differences between cloudy and clear convective boundary layers by including a consideration of the cloud “wetness” as a function of LWC and total water and potential temperature jump conditions. This attempts to account for buoyancy reversal in a weighted sense and might be expected to accelerate the dissipation of the cloud layer, but still sets the diabatic term (D) equal to zero. In this formulation

$$A = \frac{A_n \frac{\delta b}{\Delta b}}{1 + A_n \frac{\delta b}{\Delta b} \mu};$$

$$W = \eta_{q,0} \beta_{q,0} + \eta_{s,0} \beta_{s,0} + \eta_{s,h} \beta_{\Delta F,h}; \quad (2.8)$$

$$D = 0$$

where A_n is the entrainment efficiency, a semi-empirical constant, δb is a measure of the stability strength in the undulation layer as a function of cloud wetness and resulting change in buoyancy due to mixing of saturated and unsaturated parcels, μ relates entrainment as a proportion of the net forcing and the W term is equated to local weighting (η) of the top-down and bottom-up radiative (F), moisture (q), and moist static energy (s) fluxes. Another approach by Lock and MacVean (1999) attempts to include diabatic (radiative) effects and buoyancy reversal with

$$A = 0.23;$$

$$W = \eta_{q,0} \beta_{q,0} + \eta_{s,0} \beta_{s,0} + \eta_{s,h} \beta_{\Delta F,h} + 0.24 X_* \frac{-b_*}{h \Delta b} (z_c \Delta b)^{3/2}; \quad (2.9)$$

$$D = \beta_{s,m} \frac{\beta_{\Delta F,h}}{\Delta b}$$

where the formulation for W assumes that layer energetics are consistent with what one would expect in a uniformly unsaturated layer with an additional forcing term due to buoyancy reversal where X^* is the amount of free-tropospheric air as related to $(1-X)$ parts boundary layer air. The D term addresses the efficiency with which radiative forcing and water phase changes drive buoyancy fluctuations. These changes in the W and D terms enhance the efficiency with which radiation and entrainment mixing are allowed to generate turbulence.

Based on results from DYCOMS II Flight 1 as reported in Stevens et al. (2003a, 2003b) and considerations discussed in Stevens (2002) and Grenier and Bretherton (2001), our initial parameterization implements the Turner-Deardorff closure as it can be easily expressed within the COAMPSTM framework. We have also modified the length scales and determination of the jump condition as discussed in Appendix B of Grenier and Bretherton (2001) to partially account for the evaporative cooling effects caused by the mixing fraction between cloudy and clear air.

The three primary physical processes responsible for the CTBL structure are radiation, turbulence, and cloud microphysics. The CTBL has an additional source of turbulence not present in a clear convective boundary layer in that radiative flux divergence caused by the presence of the cloud results in additional buoyancy flux that drives turbulence at the cloud top. If evaporative cooling from mixing entrainment air into cloudy parcels is greater than entrainment warming, turbulence forced entrainment and can lead to cloud dissipation through buoyancy reversal. This is generally referred to as Cloud Top Entrainment Instability (CTEI) (Deardorff 1980, Randall 1980). As discussed in Stevens (2002), the relative role various mechanisms such as SST, CTEI, and drizzle play in CTBL formation, dissipation, and stratocumulus to cumulus transition is still unresolved. One area of active research with a strong effect on the CTBL structure is in the proper specification of surface fluxes and turbulent transport in the TKE closure (e.g. Miller et al. 2001, Rados et al. 2002). The specification of entrainment fluxes at the cloud-top sub-grid scale interface might be expected to have less effect, however this mechanism still results in the model being unable to capture boundary layer evolution completely as discussed in Grenier and Bretherton (2001) and Lock (2001) .

THIS PAGE INTENTIONALLY LEFT BLANK

III. EVALUATION OF COAMPSTM FOR STRATOCUMULUS TOPPED BOUNDARY LAYERS USING OBSERVATIONS

A. THE DECS FIELD EXPERIMENT AND DECS DATA ANALYSIS

In order to better understand the role of entrainment in the evolution and structure of coastal stratocumulus and the interactions with the complex coastal flow field, our approach will consist of three parts: analysis of the model diagnosed boundary layer height in comparison with the observed inversion base height, cloud thickness, and inversion strength as compared to observations, implementation of a parameterization to explicitly represent entrainment and resulting forcing in COAMPSTM, and comparison of simulations using this explicit method with simulations using the current formulation and with the observed boundary layer structure. This chapter will focus on the evolution of the predicted boundary layer field as compared to observations.

1. Observations – The Dynamics and Evolution of Coastal Stratus (DECS) Field Study

Aircraft, cloud radar, radiometer and rawinsonde observations were collected in Central California near Monterey Bay during the Dynamics and Evolution of Coastal Stratus (DECS) field study from June 13 to July 22, 1999. Twenty-one daytime research flights were flown which made 10 and 100 Hz measurements of marine boundary layer turbulence, thermodynamic, cloud microphysical, and aerosol properties using a two-engine UV-18A Twin Otter operated by the Center for Interdisciplinary Remote Piloted Aircraft Study (CIRPAS) of the Naval Postgraduate School (NPS). The instrumentation package, calibration and processing of the turbulence data are described in Kalogiros and Wang (2002). Figure 3.1 depicts the research area, surface data sites and two representative flight tracks, Figure 3.2 depicts a typical 3-dimensional flight track, and Table 3.1 describes the flights analyzed in this study. The first flight had instrument problems so the flight numbers in Table 3.1 refer to flights 2 through 21. Researchers from the University of Miami, Rosenstiel School of Marine and Atmospheric Sciences (RSMAS) operated a fixed, upward looking 94 GHz Doppler cloud radar during part of this period that allowed the determination of cloud top height, cloud reflectivity, cloud

vertical velocity and drizzle fall velocity. Kollias and Albrecht (2000) provide a description of this radar and its processing methods and Fritz et al. (2001) describes the use of the radar data to explore drizzle characteristics using a case study from DECS. A microwave radiometer operated by Pennsylvania State University was collocated with the cloud radar and was used to obtain the integrated water vapor and liquid water path. Several rawinsondes per day were launched by NPGS from the radar site on flight days. The rawinsondes were modified to measure the lower atmosphere to approximately 4000 m over about 30 minutes before descending back to the surface and providing an additional boundary layer profile during descent. The location of these instruments was at approximately 36.699N 121.808W at the City of Marina water treatment site, marked “DECS” on Figure 3.1.

Additional boundary layer observations were archived from the NPS site at Fort Ord, approximately 5 km to the northeast. This site is operated by the Naval Postgraduate School and includes 915 MHz and 404 MHz wind profilers, a Radio Acoustical Sounding System (RASS) to obtain a virtual temperature sounding, a Vaisala laser ceilometer, which provides cloud base information since the cloud radar cannot make observations below 200 m, and a surface meteorology suite that measures surface pressure, wind speed and direction, temperature and dewpoint, and shortwave and longwave irradiance. Basic data processing for the 915 MHz profiler is discussed in Ralph et al. (1998).

Surface mesonet data from the Real-time Environmental Information Network and Analysis System (REINAS; Nuss et al. 1996) as well as surface METAR, National Data Buoy Center (NDBC) and research moored buoy data, and 4km visible and infrared imagery and 1km visible geostationary satellite imagery from GOES-10 were also archived for the period.

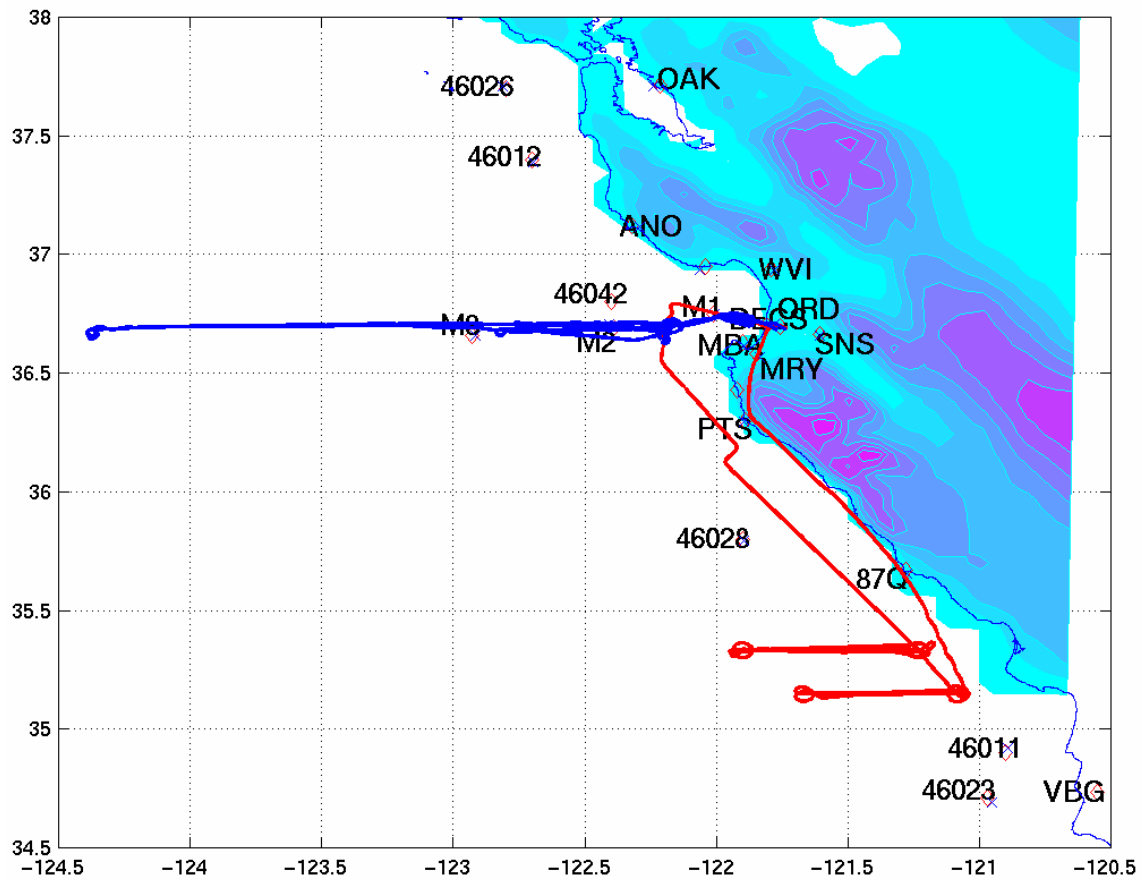


Figure 3.1. COAMPS 5km inner grid, terrain, surface data, and representative flight tracks for the DECS field campaign. Diamonds indicate surface observation sites, buoy data is identified by numbers and the designators M1-M3. Standard synoptic and mesonet surface sites are indicated by three letter call signs. Thick solid lines mark two representative flight tracks to the west and south. Flights typically consisted of stacked level legs, slant and spiral soundings and sawtooth profiles through the lower troposphere.

DECS Flight 14 07/14/1999 1510–2030 UTC

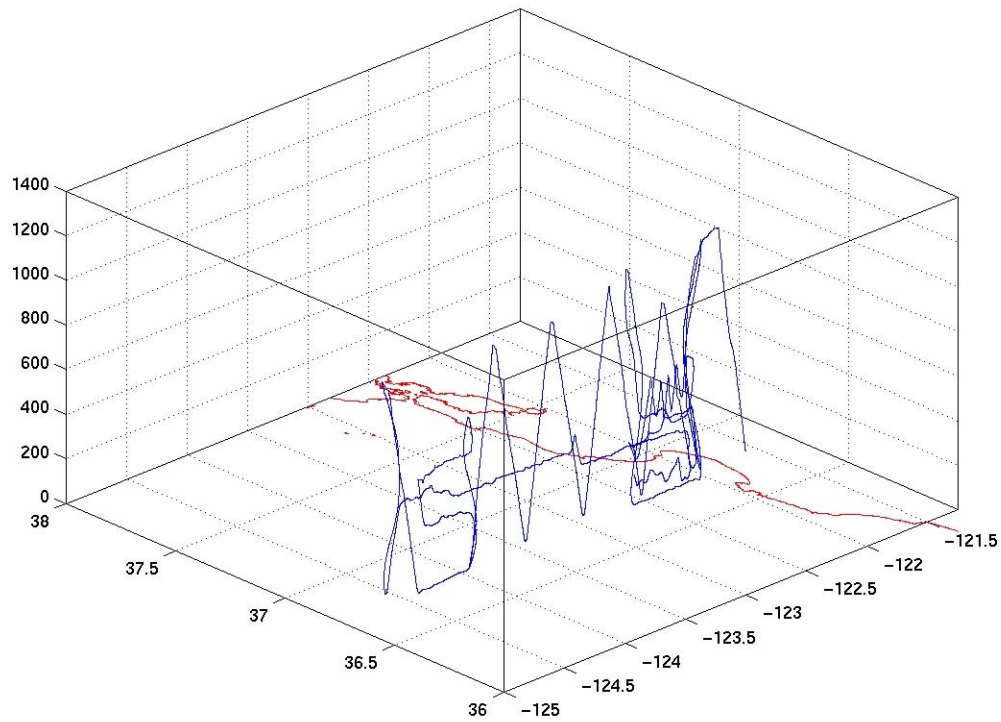


Figure 3.2. A typical three dimensional flight track during DECS. Flights included multiple sounding legs through the full extent of the boundary layer, “porpoise” or sawtooth soundings providing multiple measurements across the inversion, and level leg “stacks” of constant heading and altitude for multiple levels below, within, and above the cloud layer.

| Flight | Date | Min Lat. | Min Lon. | Max Lat. | Max Lon. | Start (UTC) | End (UTC) | Min. Alt. (m) | Max. Alt. (m) |
|--------|------|----------|----------|----------|----------|-------------|-----------|---------------|---------------|
| 1 | 618 | 36.61 | -122.94 | 36.71 | -121.66 | 1500 | 1620 | 27 | 1500 |
| 2 | 619 | 36.48 | -122.58 | 36.99 | -121.75 | 1530 | 1915 | 32 | 954 |
| 3 | 621 | 36.60 | -122.57 | 36.79 | -121.76 | 1430 | 1525 | 26 | 990 |
| 4 | 624 | 36.66 | -122.92 | 36.87 | -121.76 | 1500 | 1930 | 21 | 967 |
| 5 | 625 | 36.18 | -122.93 | 36.74 | -121.60 | 1500 | 1745 | 28 | 2403 |
| 6 | 628 | 35.11 | -122.21 | 36.80 | -121.04 | 1430 | 1845 | 32 | 2140 |
| 7 | 629 | 35.47 | -122.76 | 36.78 | -121.15 | 1430 | 1900 | 15 | 3266 |
| 8 | 702 | 34.72 | -122.54 | 36.71 | -121.00 | 1700 | 1945 | 49 | 1414 |
| 9 | 703 | 34.41 | -121.93 | 36.70 | -121.82 | 1345 | 1815 | 25 | 1450 |
| 10 | 706 | 36.63 | -124.39 | 36.75 | -121.73 | 1500 | 1930 | 21 | 1471 |
| 11 | 707 | 36.66 | -122.76 | 36.81 | -121.76 | 1540 | 1815 | 26 | 970 |
| 12 | 709 | 36.66 | -124.38 | 36.73 | -121.76 | 1500 | 1915 | 21 | 1063 |
| 13 | 710 | 36.65 | -124.37 | 36.73 | -121.76 | 1500 | 1930 | 25 | 1410 |
| 14 | 714 | 36.66 | -124.71 | 36.74 | -121.76 | 1510 | 2000 | 15 | 1160 |
| 15 | 715 | 36.65 | -124.70 | 36.75 | -121.76 | 1500 | 1700 | 25 | 1289 |
| 16 | 716 | 35.70 | -124.71 | 36.74 | -121.76 | 1800 | 2230 | 26 | 1357 |
| 17 | 717 | 36.33 | -123.04 | 36.87 | -121.62 | 1530 | 2015 | 28 | 1846 |
| 18 | 719 | 36.67 | -124.71 | 36.81 | -121.76 | 1450 | 2020 | 22 | 1829 |
| 19 | 720 | 36.66 | -123.06 | 36.74 | -121.76 | 1500 | 2015 | 17 | 1827 |
| 20 | 722 | 36.58 | -125.05 | 36.92 | -121.76 | 1800 | 2200 | 29 | 1442 |

Table 3.1. General information on the DECS flights analyzed in this study. Flights included multiple sounding legs through the full extent of the boundary layer, “porpoise” soundings providing multiple measurements across the inversion, and level leg “stacks” of constant heading and altitude for multiple levels below, within, and above the cloud layer.

B. COAMPSTM SIMULATIONS FOR DECS CASES

1. Model Configuration

In this study, our primary data analysis and visualization software tool was MATLAB version 5.3, a program commonly used in the scientific community data analysis. Meteorological analysis and forecast simulations were conducted with COAMPSTM version 3.1 as described in Chen et al. (2003). COAMPSTM was run in a mode similar to the current operational forecast model (30 levels), triply nested at horizontal resolutions of 45, 15 and 5 km as depicted in Figure 3.3. The vertical grid was modified slightly to add resolution in the boundary layer (Table 3.2) and to ensure consistent vertical grid spacing across the inversion for ease in data interpretation. Several other modifications were also completed and tested in the memory arrays and output routines to aid in model result interpretation. These changes create additional output variables such as the TKE budget components and radiative and turbulent fluxes. Identical comparison runs were done to ensure the code changes designed to produce additional output variables did not inadvertently change the memory arrays or model results.

The model was run using the COAMPSTM Ocean Data Assimilation (CODA) in order to analyze the ocean sea surface temperature (SST) and ice fields from observations at higher resolution suitable for mesoscale forecasts rather than using the analysis fields from the global model (NOGAPS). This allows the mesoscale variability in the coastal zone from satellite retrievals (approximately 10 km resolution) and ship and buoy data to be better represented. Figure 3.4 compares observed SSTs from AVHRR satellite data to the model analysis fields. The general features are well depicted including a pronounced cooling extending westward and southward of Point Reyes and Point Sur and general warming to the south and west overall with coolest temperatures near the coast. The model was run in simulation mode for the entire period of the DECS field study, from June 13, 1999 to July 22, 1999. This means that the forecast was run to twelve hours and then a new data assimilation cycle was run to combine the forecast with observed conditions. This is different from the typical operational 48-72 h forecast length in order

to better represent the real atmosphere, thus the model tendencies are periodically bounded by synoptic observations when comparing the model forecast to observations. Observation flights were typically done between 1500 and 2000 UTC corresponding to a 3 to 8 h model forecast. This period is shorter than the 8-12 hour pre-integration time suggested by Cui et al. (1998) for dynamic initialization to ensure all gravity wave oscillations caused by the initialization have propagated out of the model domain. In our case, however, we decided that capturing the synoptic conditions from the conventional observations was more important than ensuring dynamic balance since we are comparing model forecasts to specific observations and events. None of the special data from the field study was assimilated in the initial analysis for the simulations. Therefore the comparisons between the model and the DECS observations are truly independent and the mesoscale and marine boundary layer structure in the simulation relies mostly on the model physics and large scale forcing since these structures are under-resolved in the observations. The COAMPSTM simulations did however include all standard data sets used in the operational model such as surface observations, coastal buoys, rawinsondes, and satellite data.

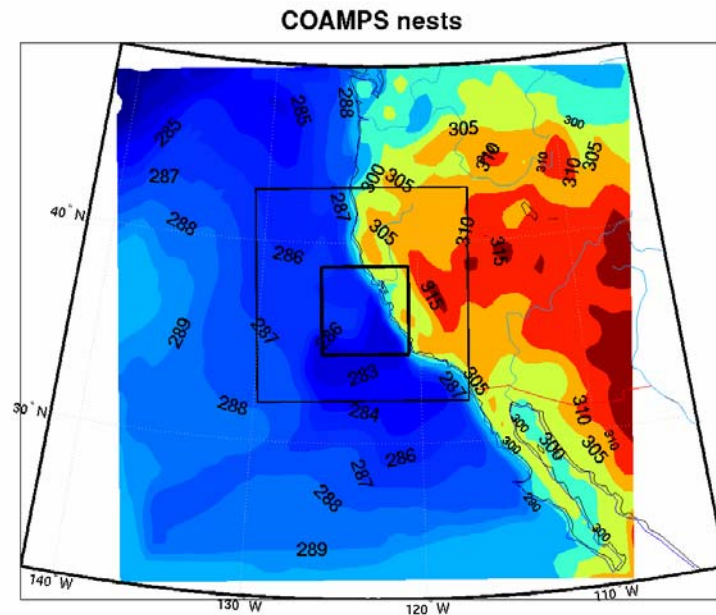


Figure 3.3. 1800 UTC 10m Potential temperature (K) and model nest boundaries for the DECS simulations.

| Operational COAMPS | | Modified COAMPS | | Approximate Pressure (mb) |
|--------------------|-----------------|-----------------|-----------------|---------------------------|
| Sigma (m) | Delta Sigma (m) | Sigma (m) | Delta Sigma (m) | |
| 31050 | 7500 | 27350 | 7500 | 15 |
| 24400 | 5800 | 20700 | 5800 | 50 |
| 19400 | 4200 | 15700 | 4200 | 110 |
| 16050 | 2500 | 12350 | 2500 | 185 |
| 14300 | 1000 | 10600 | 1000 | 240 |
| 13300 | 1000 | 9600 | 1000 | 280 |
| 12425 | 750 | 8725 | 750 | 320 |
| 11675 | 750 | 7975 | 750 | 355 |
| 10925 | 750 | 7225 | 750 | 400 |
| 10175 | 750 | 6475 | 750 | 440 |
| 9425 | 750 | 5725 | 750 | 490 |
| 8675 | 750 | 4975 | 750 | 540 |
| 7800 | 1000 | 4200 | 800 | 600 |
| 6800 | 1000 | 3400 | 800 | 660 |
| 5800 | 1000 | 2600 | 800 | 740 |
| 4800 | 1000 | 1900 | 600 | 805 |
| 3900 | 800 | 1400 | 400 | 855 |
| 3100 | 800 | 1050 | 300 | 895 |
| 2300 | 800 | 850 | 100 | 915 |
| 1600 | 600 | 750 | 100 | 925 |
| 1100 | 400 | 650 | 100 | 940 |
| 750 | 300 | 550 | 100 | 950 |
| 500 | 200 | 450 | 100 | 960 |
| 330 | 140 | 350 | 100 | 970 |
| 215 | 90 | 260 | 80 | 980 |
| 140 | 60 | 180 | 80 | 990 |
| 90 | 40 | 115 | 50 | 1000 |
| 55 | 30 | 65 | 50 | 1005 |
| 30 | 20 | 30 | 20 | 1010 |
| 10 | 20 | 10 | 20 | 1015 |

Table 3.2. Operational and modified model vertical levels.

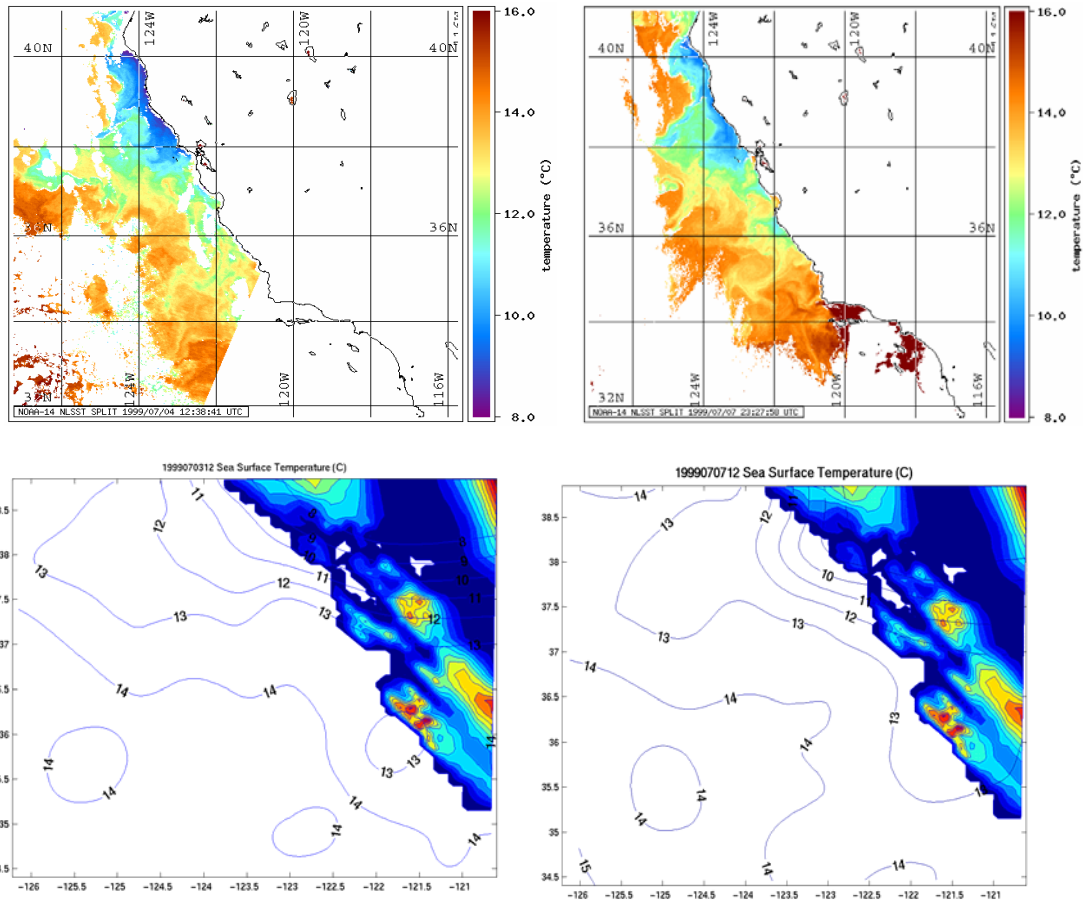


Figure 3.4. Comparison of CODA Sea Surface Temperature Analysis with AVHRR satellite observations for 2 days during the DECS field study. Note the general agreement between the model analysis and observations for features such as the cooler temperatures offshore of Point Reyes and Point Sur and a warming trend to the southwest.

2. Modifications to the Calculation of In-cloud Buoyancy Flux

In initial COAMPSTM simulations it was noted that forecast LWC and LWP values were an order of magnitude too small for an otherwise reasonable thermodynamic profile as compared to observations. Investigation into this issue indicated that under-prediction of low cloud may be attributed to the method used to diagnose of the presence of cloud and the applicable thermodynamic variable in calculation of the in-cloud buoyancy flux in the boundary layer turbulence scheme. COAMPSTM uses the condensation rate to diagnose if a cloud layer is present in calculating the buoyancy contribution to turbulence, but this method has the effect of diagnosing a cloud-free condition if cloud is dissipating but still present (Shouping Wang 2003, personal communication). An incorrect TKE profile therefore results as the fluxes are calculated for clear air and the cloud layer thus dissipates too rapidly. Modifications to the boundary layer scheme to use a saturation condition vice condensation rate to define the cloud layer are planned for incorporation in a future COAMPSTM release. The turbulence scheme was modified to identify the cloud layer from the saturation condition and then use the liquid potential temperature gradient in-cloud to calculate the stability function for the mixing coefficient vice using the virtual potential temperature gradient. This produced much better results for the summertime stratus cases in this study as can be seen in Figure 3.5. All simulations and COAMPSTM versions discussed in this study except for the comparison test in Figure 3.5 use the boundary layer subroutine modified as discussed to produce more realistic cloud fields.

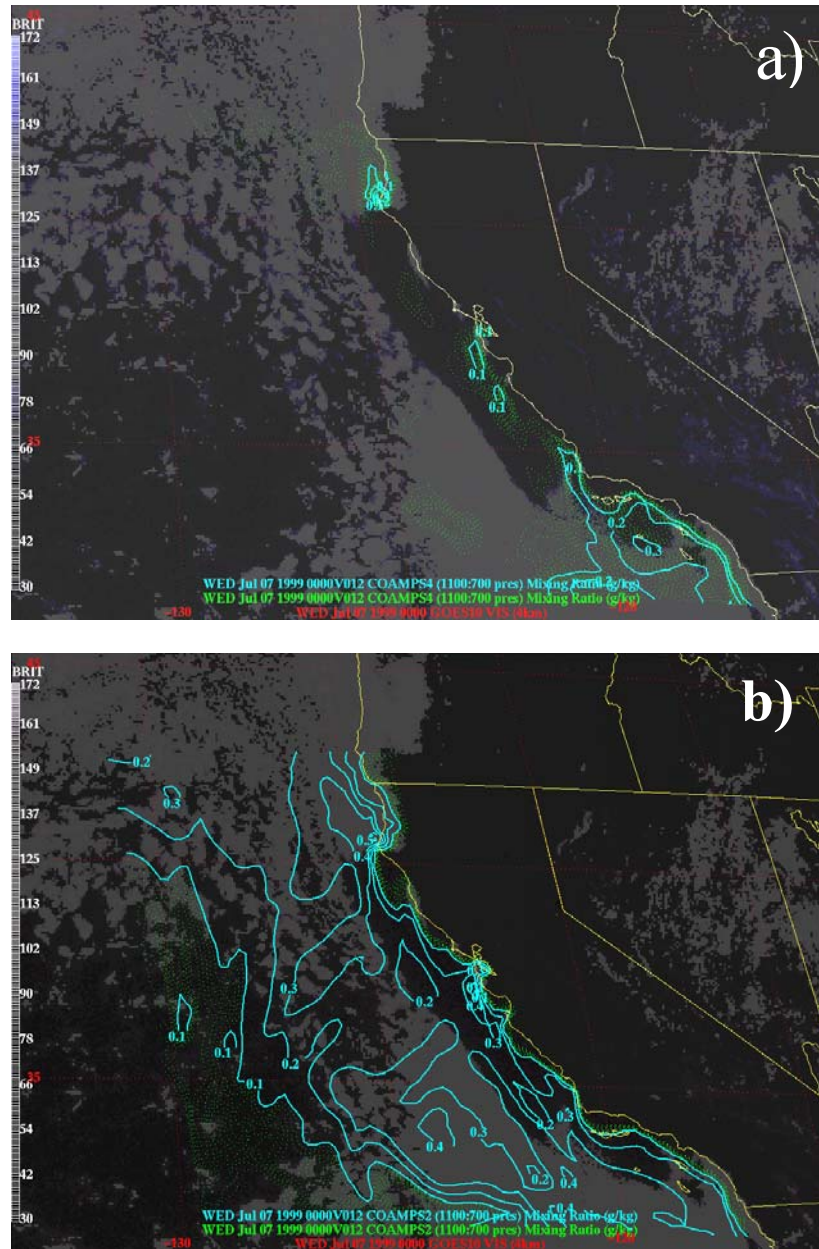


Figure 3.5. 12 hour forecast of integrated cloud liquid water (kg m^{-2}) for a) original COAMPS™ 3.1 and b) the modified turbulence parameterization. The parameterization was modified to 1) identify the cloud layer from the saturation condition vice the condensation rate and 2) calculate the stability in-cloud for the turbulent mixing coefficient from the liquid potential temperature gradient.

C. COAMPSTM – DECS COMPARISON

To better understand the ability of the simulations to accurately forecast the boundary layer and cloud structure, the simulation results were compared to aircraft observations. Vertical profiles of model output on a one hour interval were extracted from the 5 km inner nest for the closest point corresponding to the mean time and position for each of 445 aircraft slant sounding legs. The aircraft flights were generally between 1500 and 2000 UTC, which corresponds to a 3-8 hour model forecast. The total water and buoyancy fluxes from the model were also extracted for each level flight leg. Turbulent variances and fluxes can also be calculated using the eddy correlation method for the slant path soundings, however the results may be less reliable for sounding legs, especially if the aircraft is not maintaining a steady heading and rate of ascent. Mean turbulence values from level legs at various altitudes were therefore also calculated and compared to slant path and model profiles. Hourly east-west cross-sections for both the daytime (1200 UTC) and nighttime (0000 UTC) simulations along the mean flight track latitude were also analyzed from the model to assess diurnal development and variability. The purpose here is to describe the general CTBL structure and variability in both the simulations and observations. This analysis will allow us to determine the performance of the current operational forecast model for the period of interest and will be the basis for adjustments made to the turbulence parameterization within COAMPSTM via the explicit entrainment velocity calculation and fluxes to examine the effect of implicit entrainment in the current model formulation.

The thermodynamic structure of the model atmosphere was found to compare well to both the aircraft sounding legs and coastal rawinsondes (not shown). Surface temperatures were generally within 1 degree (K) and values in the free atmosphere matched well. As shown in Figure 3.6, the east-west cross-sections depict a characteristic lowering of the inversion height towards the coast with a much steeper slope within 100 km of the coast and increasing heights across the coast and the coastal plain until the boundary layer intersects the terrain. The observed structure in Figure 3.6.a) does not slope as sharply in the inner coastal, which is partly an artifact of the smoothing and plotting of limited point data, but still shows the characteristic slope offshore. The wave

pattern in the model data and the lowering boundary layer height farther offshore near 125 W that are not seen in the observations are likely due to a combination of smoothing of the observational data and gravity wave propagation from the Sierra Nevada as discussed in Cui et al. (1998). The rapidly changing inversion height in the inner coastal has a strong diurnal and synoptic characteristic and is associated with terrain-induced increased mesoscale subsidence and the MCLLJ. When compared to observations, the structure as depicted in Figure 3.6 seems to be well supported, although the slope is too steep and the inversion height is too low. Figure 3.7 compares the model inversion height based on the vertical θ_1 gradient to the observations, which shows that this low bias is consistent throughout the field study and that there is a mean bias of 200 meters. The consistent bias at different forecast times and under different synoptic conditions supports our theory that differences between the COAMPSTM simulation and the observed structure are not an artifact of a poor initialization or lack of dynamic balance in the simulation but rather are caused by inappropriate representation of key physical processes. Figure 3.8 is the difference between modeled and observed boundary layer height as a function of cross-coast longitude. Although there is more scatter in the inner coastal zone, a dependence on cross-coast distance is not readily apparent.

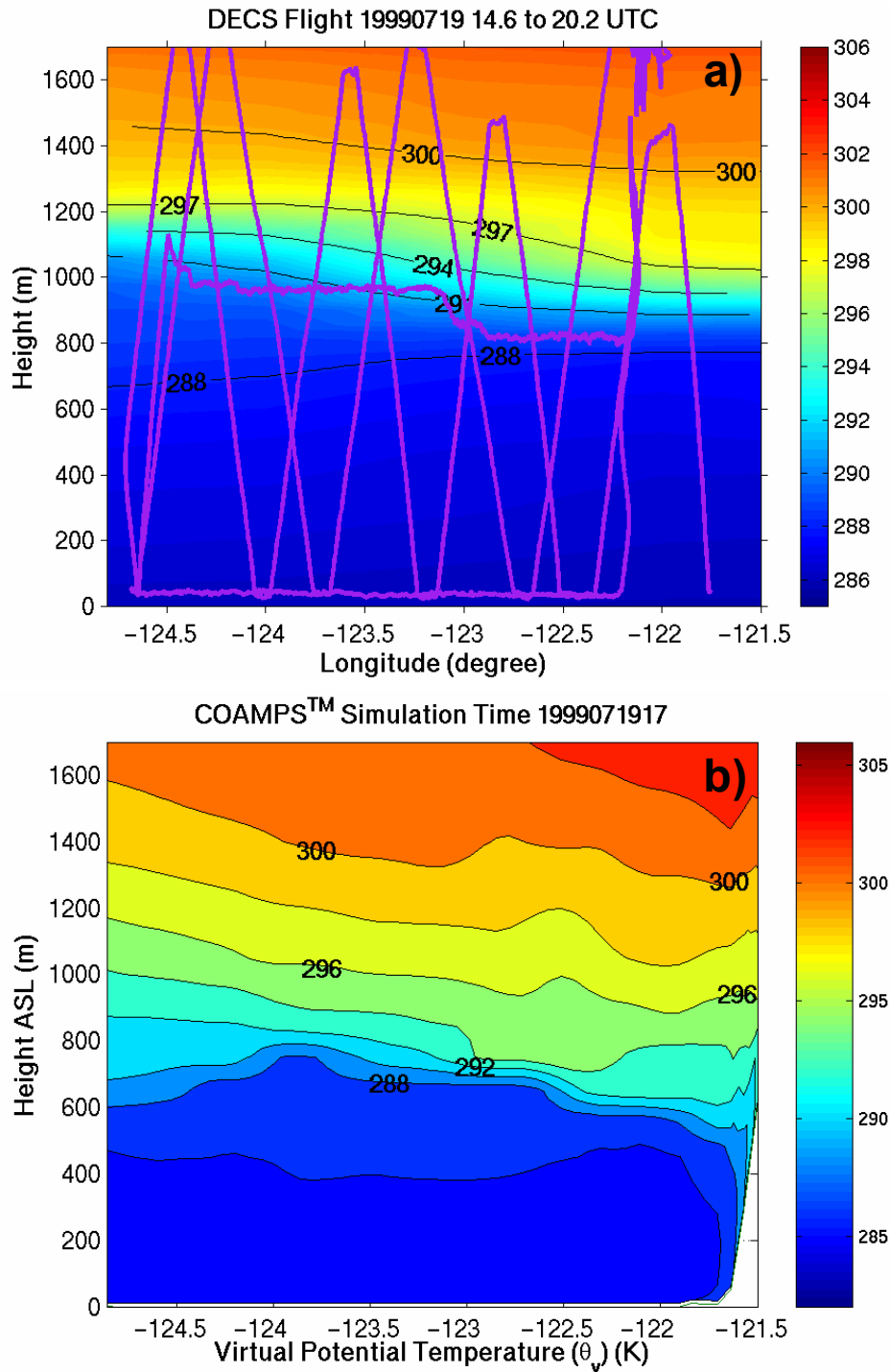


Figure 3.6. Comparison of virtual potential temperature (K) between a) the observations and b) the corresponding model forecast. A solid line superimposed on the contour plot depicts the flight track for the observations. The COAMPS™ simulation is a five hour forecast valid at 1700 UTC, close to the midpoint of the aircraft flight.

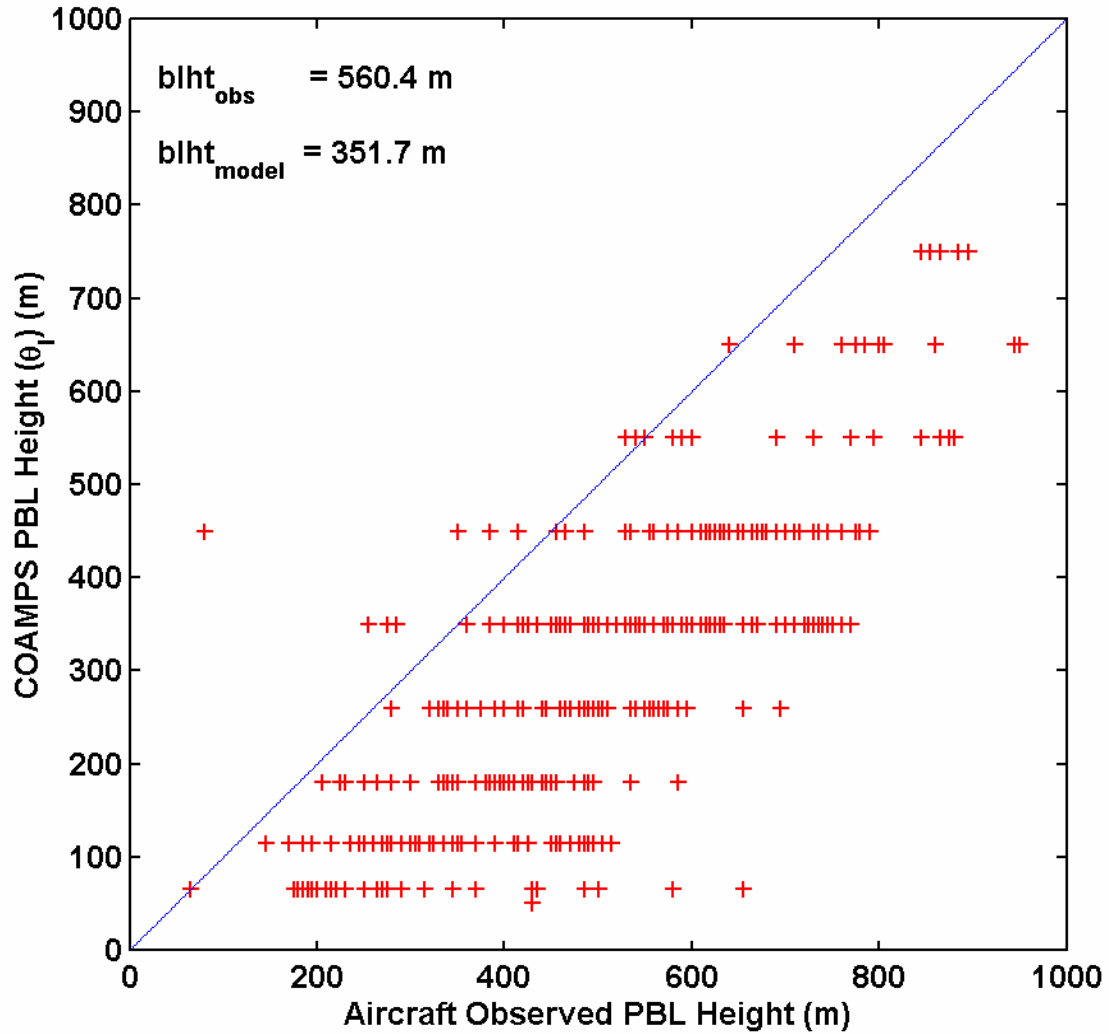


Figure 3.7. Comparison of observed and modeled PBL heights as defined from the height of the greatest potential temperature gradient (K m^{-1}) or “jump”. Values in the upper left corner are the mean values for the aircraft measurements and corresponding COAMPSTM profiles.

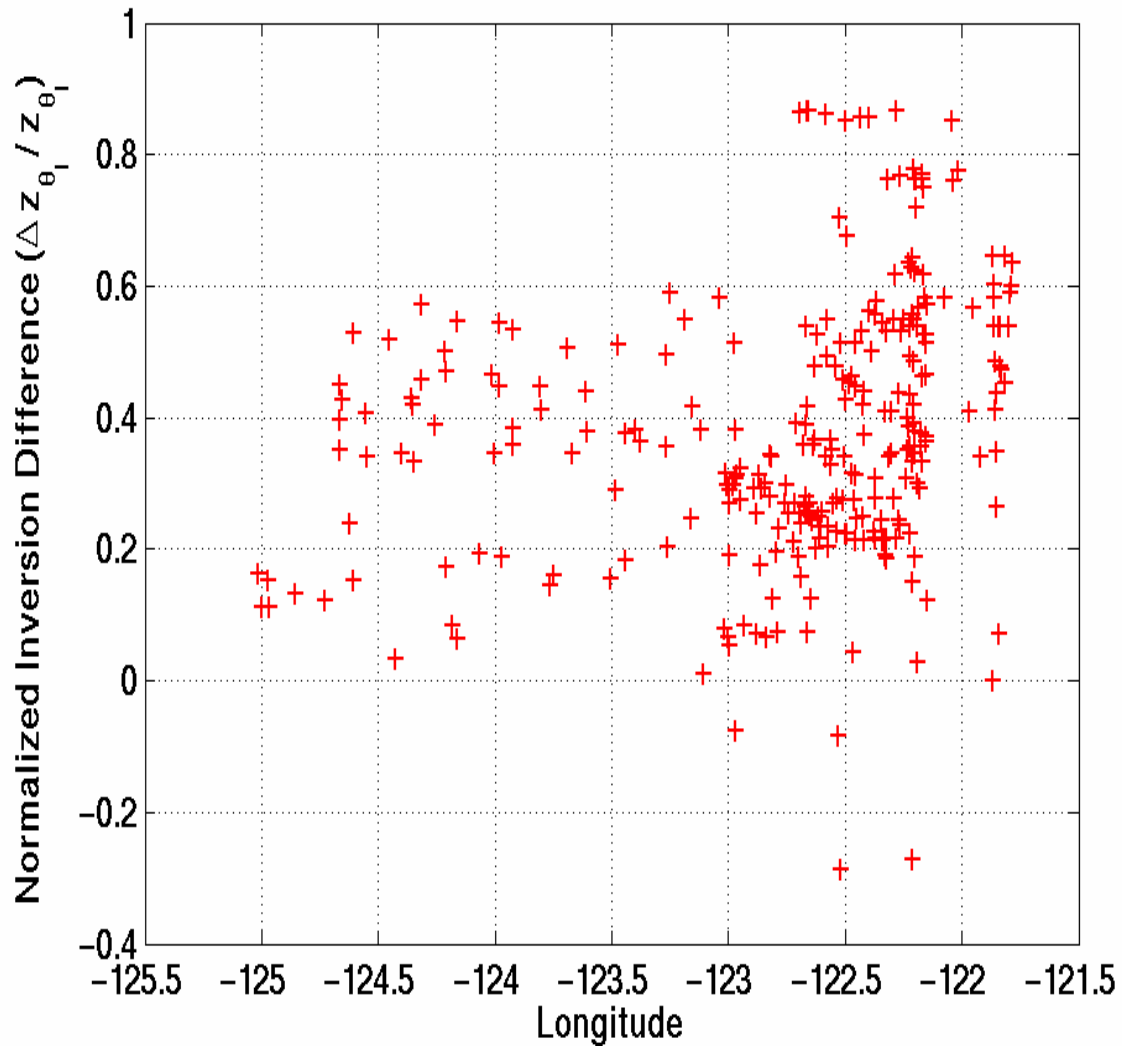


Figure 3.8. Differences between the observed and COAMPSTM boundary layer height normalized by the observed boundary layer height as a function of longitude. Boundary layer height is determined from the height of the greatest liquid potential temperature gradient (K m^{-1}) or “jump”. (Groupings at 0.2 and 0.5 correlate to particular flight days and represent the fit between the forecast and the synoptic conditions rather than a particular boundary layer regime.) Note the larger variability in the inner coastal zone between 121.5 W and 123.0 W.

Figure 3.9 shows a comparison of modeled LWP to the corresponding observed cloud field. Qualitatively COAMPSTM represents variations in the coastal stratus field well compared to the satellite observations. Climatologically, the marine stratus is relatively persistent offshore with thinning/ dissipation and a more cellular structure developing frequently during the day. A thin finger of fog and stratus is often observed, which persists in a narrow zone within 30 km of the coast, especially downwind from prominent points such as Pt. Arena and Pt. Sur. A characteristic oval shaped cloud thinning associated with the onset of the LLCJ is often observed downstream from Cape Mendocino and occasionally downstream of less prominent points such as Point Reyes, Pescadero Point, and Point Sur. This lowering of the boundary layer and cloud thinning often persists for 2-3 days and the diurnal signal is superimposed on this temporally synoptic and spatially mesoscale variability. At the coast over land, the cloud patches that persist during the day often deepen and develop in late afternoon and become indistinguishable from developing nocturnal valley fog, which generally dissipates by mid-morning. The model depicts these major observed cloud features quite well including the persistent marine stratus, diurnal variation in cloud fraction and thickness west of about 123 N, inner coastal clearing associated with the coastal jet and sea-breeze forcing and more persistent cloud upwind of headlands, and nocturnal valley fog clearing by midday. Figure 3.10, COAMPSTM is an East-West cross-section of cloud liquid water mixing ratio at 37.1 N along the aircraft flight path. A lowering of the cloud top and base in the narrow inner coastal zone is seen in both the observations and model output which matches our expectation from considerations of lower SSTs and increased mesoscale subsidence due to flow interaction with the terrain. The model frequently produces fog in this zone (not shown), however observations indicate that, although the cloud top and base in this region is generally lower than elsewhere, it is usually not saturated all the way to the surface, especially during daytime.

Figure 3.11 compares the observed and modeled cloud top height. The 200 m low height bias seen in the liquid potential temperature gradient is also seen here which further supports our conclusion that the boundary layer height is too low in COAMPSTM

in the CTBL regime. Figure 3.12 is a comparison between the observed maximum cloud liquid water mixing ratio, which occurs at cloud top, and the modeled values. COAMPSTM may be expected to have slightly lower peak values than the observations as a result of representation of a sharp gradient on a coarse discrete grid. Instead, this comparison shows that the maximum liquid water mixing ratio in COAMPSTM is consistently about 25% too high. The low cloud top bias and high cloud LWC bias have important implications to the radiation budget, optical depth, and surface heating by solar warming in the model and are a major focus of this study. Figure 3.13 is a comparison of the cloud base to ceilometer data for a representative two day period. The ceilometer is sufficiently sensitive to scattering by liquid water and aerosols to detect liquid water mixing ratios to about 0.02 g kg^{-1} . Based on the ceilometer and aircraft data, both the cloud top and base in COAMPSTM are about 200 meters too low. The cloud also lifts and dissipates 1-3 hours later than indicated from observations and reforms 1-3 hours sooner, which is consistent with over-prediction of LWC.

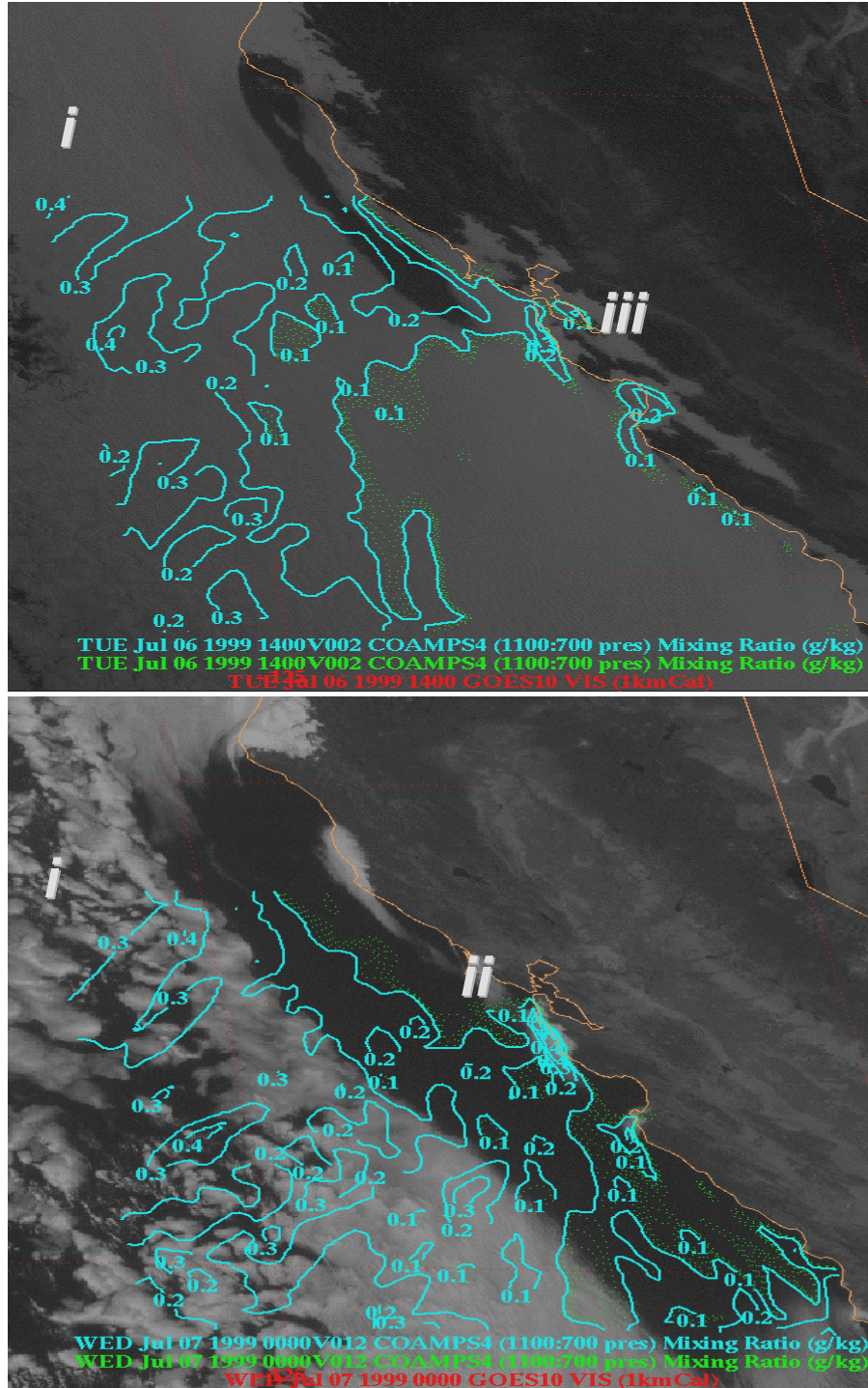


Figure 3.9. Vertically integrated liquid water mixing ratio (g kg^{-1}) (LWP) from COAMPSTM and corresponding visible 1 KM satellite imagery. The model qualitatively matches the observations for major coastal cloud features including: i) persistent marine stratus with a diurnal change in cloud fraction, ii) coastal clearing with persistent patches upwind from points, and iii) coastal stratus and inland valley fog with a strong diurnal character.

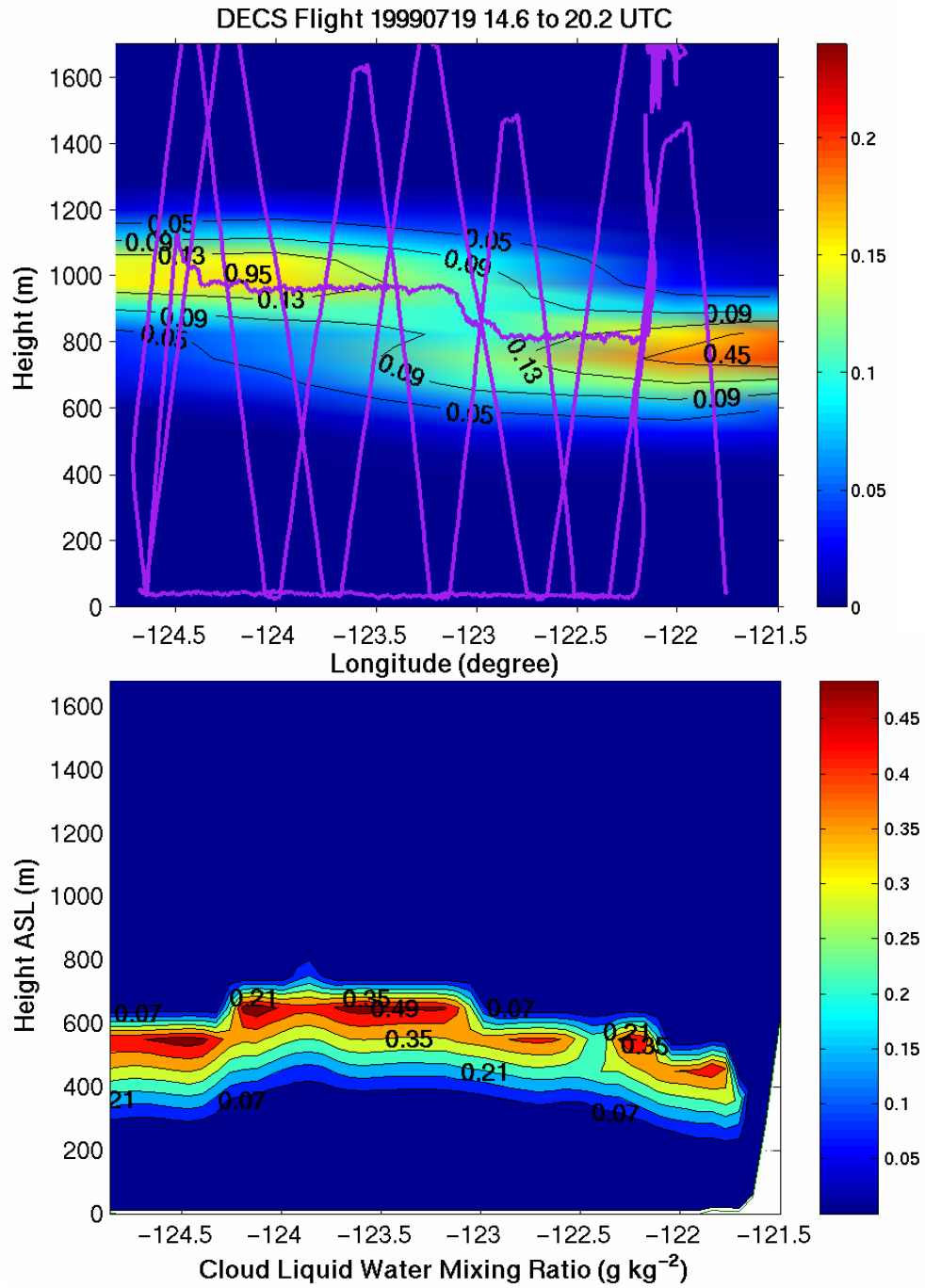


Figure 3.10. Comparison of cloud liquid water mixing ratio (g kg^{-1}) between the model and the observations along and East-West cross-section at 37.1°N , which corresponds with the aircraft flight track. A solid line superimposed on the contour plot depicts the flight track for the observations. The COAMPSTM simulation is a five-hour forecast valid at 1700 UTC, close to the midpoint of the aircraft flight.

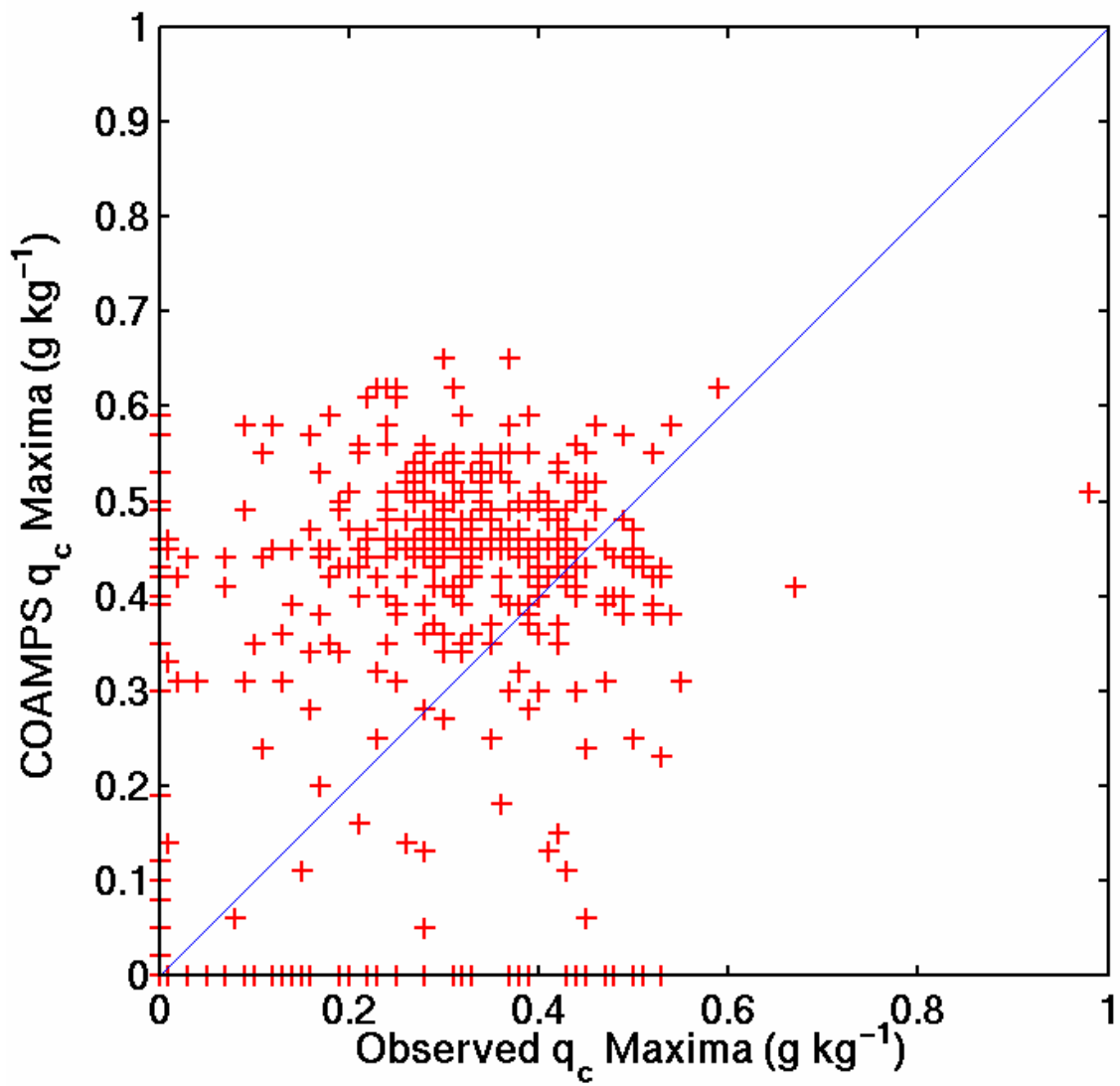


Figure 3.11. Scatter plot of observed and modeled maximum liquid water mixing ratio.

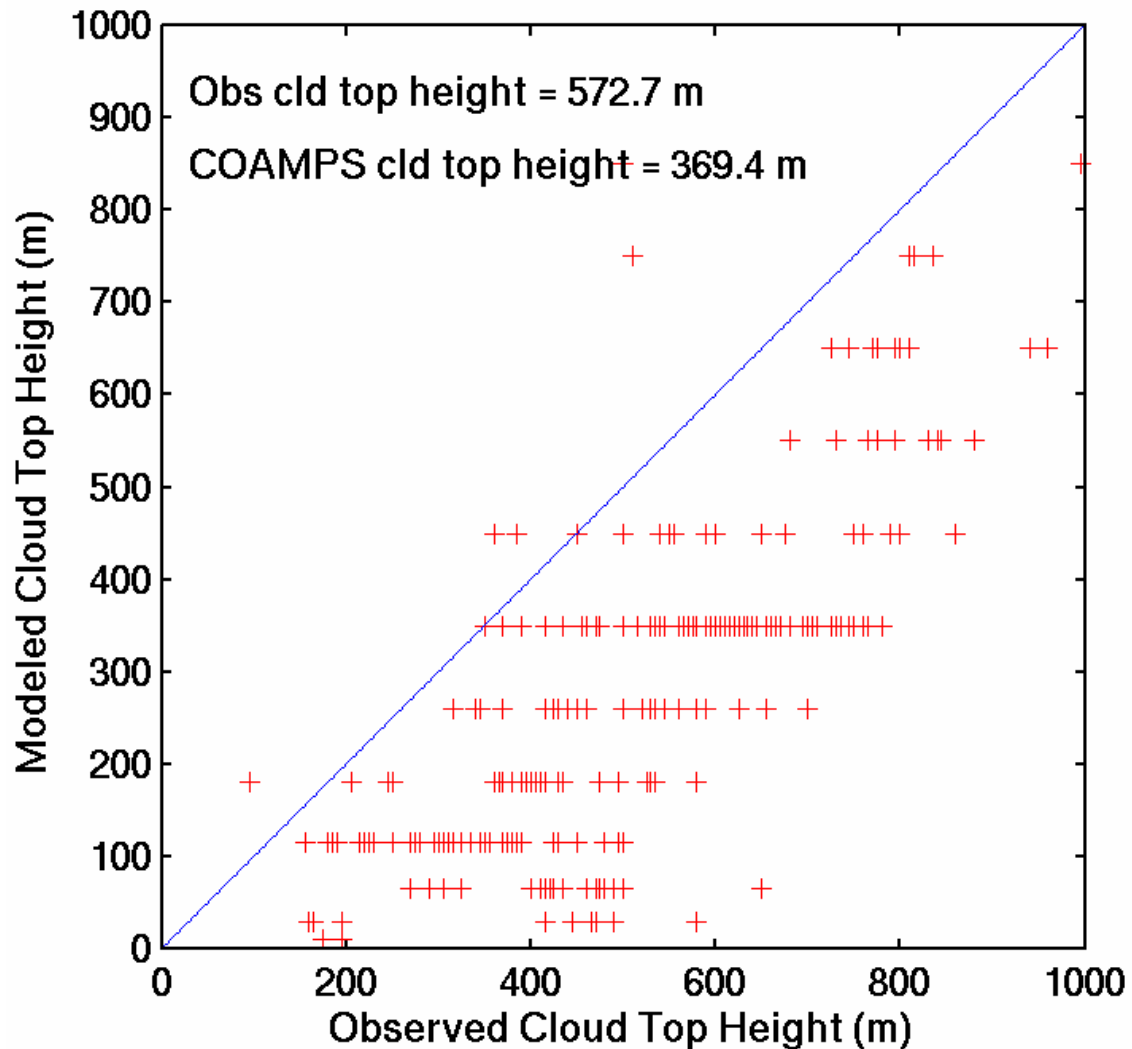


Figure 3.12. Comparison of cloud top height (m) between the model and the observations. In the case of the discrete model grid, cloud top height is taken as the level of maximum cloud liquid water mixing ratio. In the observations, the vertical distance between this value and a zero value is tens of meters while the model may represent the cloud top across 2-3 grid levels at 100 m vertical resolution.

COAMPS™ Simulation and NPS Ceilometer Observations 06/23/1999–06/25/1999

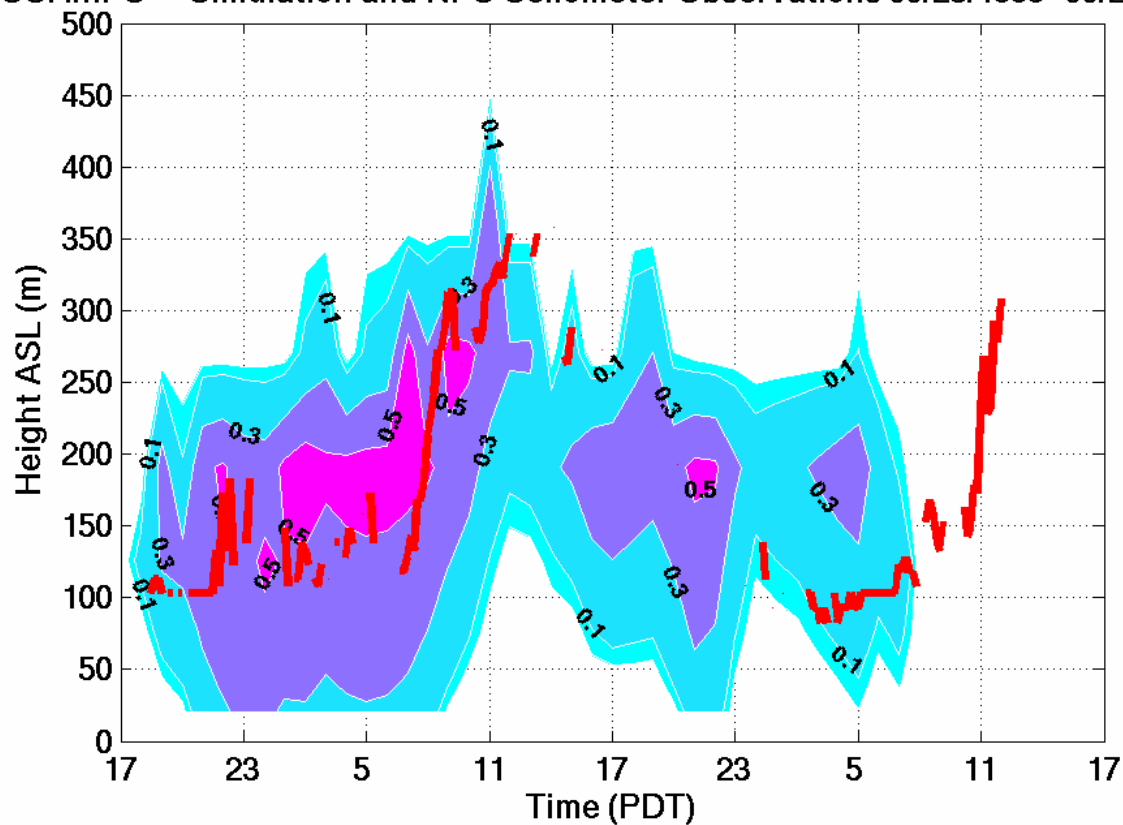


Figure 3.13. Time series plot of observed ceilings (line data) at the NPS Ft. Ord ceilometer site and modeled liquid water mixing ratio (g kg^{-1}) (filled contours).

We also examined the predicted wind field relative to the MLLCJ and compared it with available observations. The horizontal structure in the simulated MLLCJ depicted in Figure 3.14 matches the conceptual model of terrain induced variability well, although the horizontal velocity patterns cannot be verified from observations. The presence of the jet is often difficult to detect in surface observations in that it reaches its maximum magnitude at the boundary layer top, therefore the reflection of the LLCJ in buoy observations depends on momentum mixing in the boundary layer. Detection in aircraft observations requires that the available data are sufficiently dense and correctly located in time and space to capture the complete structure. The horizontal variability in the LWP depicted in Figure 3.14 correlates well with the conceptual model of the cloud patterns and jet structures arising from the boundary layer response to the coastal flow and typically observed cloud patterns seen in satellite data under this regime (not shown). The vertical structure of increasing winds at the boundary layer top along an east west sloping inversion matches the conceptual model and the aircraft observations well as can be seen in Figure 3.15. The aircraft slant path soundings provide a unique opportunity to directly study the vertical structure of the jet at varying distances offshore.

In comparing the observed and modeled vertical wind structure in jet regions it was noted that the classic LLCJ velocity profile of a distinct velocity maximum at the inversion and decreasing wind speeds towards the surface was rarely observed in cloudy cases in the observations. Instead the aircraft soundings often depicted uniform stronger winds within and below the cloud and decreasing winds above the cloud top. Occasionally wind speed would increase again to a secondary maximum well above the boundary layer top. In the no-cloud cases the observations generally matched the expected vertical wind speed structure from LLCJ theory of increasing winds in the free atmosphere towards the surface to a maximum at the boundary layer top and decreasing winds in the boundary layer. On the other hand, the model generally produced a relative velocity maximum at the boundary layer top in both cloudy and clear cases as depicted in Figure 3.16.

Figure 3.17 is an example from one flight of the observed and modeled fluxes for a series of “stacked” level legs. Because the turbulent fluxes derived from 10 Hz slant

profiles of aircraft data using the eddy correlation method have the potential for large uncertainty, especially if the aircraft maneuvers or does not maintain a sufficiently slow and constant ascent rate, discussion of the observed fluxes is based a subset of vertical profiles with a long ascent path and constant heading and averaged flux values calculated from stacks of long, horizontal legs. The observations generally showed small surface buoyancy fluxes on the order of $10\text{-}15\text{ W m}^2$ at the surface and decreasing to a minimum, or even slightly negative buoyancy at the top of the sub-cloud mixed layer. Buoyancy flux then increased in the cloud layer to a maximum near cloud top approximately equal or larger than the surface buoyancy flux. There was a great deal of scatter in the cloud top flux measurements with large positive and negative fluxes occurring. This general structure is well correlated between the individual soundings and level leg averages. Figure 3.18 and 3.19 depict a typical sounding leg and corresponding model sounding for a cloudy case and a no-cloud case respectively. Note the much closer agreement between COAMPSTM and observations for the no-cloud in Figure 3.19. Frequently the simulation and the observations were in reasonably good agreement in the sub-cloud layer, however the model cloud layer was too low, making it difficult to distinguish between surface and cloud forcing. In the entrainment zone at and just above the inversion, a narrow region of strong negative buoyancy flux was often observed, especially when vertical wind shear was large. This was also represented in the simulations, although less frequently and with a smaller magnitude. Mixing between the dry inversion air and the cloud can lead to evaporative cooling and positive buoyancy flux through buoyancy reversal. Since, the turbulence parameterization implicitly represents the entrainment, the tendency of the model to under-predict the magnitude of the large positive fluxes in-cloud and negative fluxes in the entrainment zone supports our hypothesis that the implicit approach cannot adequately represent the entrainment velocity across a narrow sub-grid scale entrainment zone.

In summary, the model captured the structure and evolution of the boundary layer reasonably well, with the exception of a consistent high bias in cloud liquid water and low bias in inversion strength and height. These biases in the inversion strength and height were seen more strongly in cloud-topped cases than in clear boundary layers and

were seen more strongly in the potential temperature profile than in the water vapor profile. On average, the height bias was 200 meters, approximately 25% of the total boundary layer height, but varied from less than 100 meters to more than 600 meters. These trends were confirmed with over 400 individual sounding legs, 80 level legs and 20 flights in varying synoptic conditions. This strengthens our hypothesis that sub-grid cloud top processes are a likely the source of this bias, which is investigated in Chapter V.

This study was designed to examine the performance of COAMPSTM at the relatively coarse operational vertical spacing of 100m. However, because our reasoning for investigating an explicit entrainment approach partly relies on the under-resolution of the entrainment zone in the implicit approach, sensitivity tests were conducted to examine the model dependency on vertical grid resolution. COAMPSTM simulations were run with 40 vertical levels (vice 30) with 50 m resolution to a height of 1000 m in SCM and full three dimensional versions. The boundary layer height grew more rapidly in the 40 level SCM and the cloud liquid water mixing ratio was 10% smaller (not shown). The three dimensional tests showed similar results with a sharper cloud liquid water gradient as seen in Figure 3.20 that qualitatively matched observed typical CTBL structure better, and higher boundary layer heights by 50-100m as seen in Figure 3.21. As will be discussed in Chapter VI, the magnitude and direction of these changes are similar to the effects of explicitly parameterizing entrainment. The computational expense is much larger however, with the EEP having negligible effect on run time while the increased vertical resolution increases the wall clock time of a simulation by 50-75%, which in our configuration results in a 12 hour forecast taking 16 hours to complete vice 9 hours for the control or EEP simulations. Developing a framework in COAMPSTM for EEP is also useful for studying the underlying physical mechanisms involved in cloud-top entrainment aside from the motivation of improving the operational forecast model.

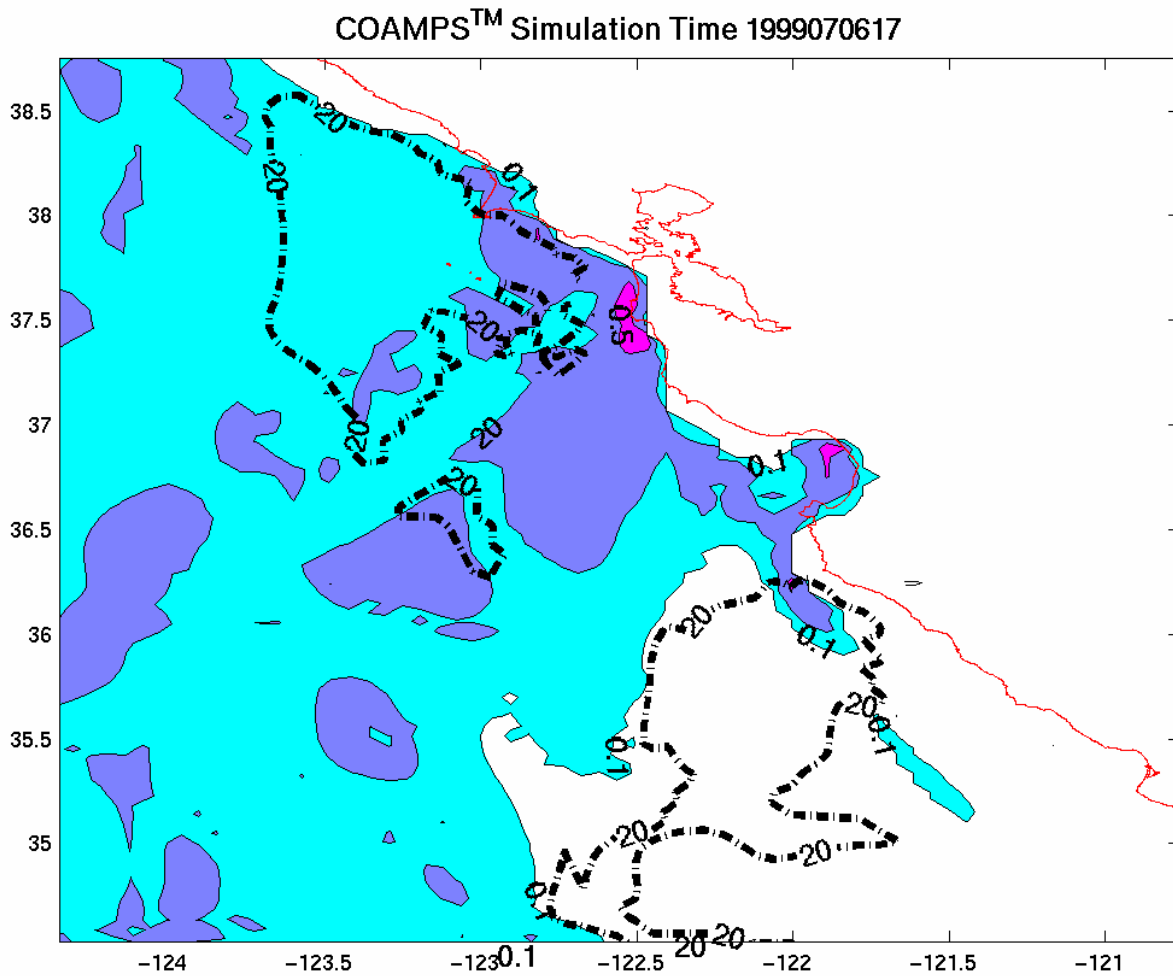


Figure 3.14. Predicted Liquid Water Path (LWP) (shaded) (kg m^{-2}) and wind speed at the inversion (dashed bold lines) (m s^{-1}). The COAMPS™ simulation is a five-hour forecast valid at 1700 UTC, close to the midpoint of the aircraft flight. Note that in the COAMPS™ simulation the relative minima in LWP correspond with maxima in the wind speed. This horizontal structure is difficult to depict in observations due to our inability to sufficiently resolve the large scale three dimensional structure in observational data, however the model depiction matches well with satellite observations of cloud patterns and point observations of wind velocity.

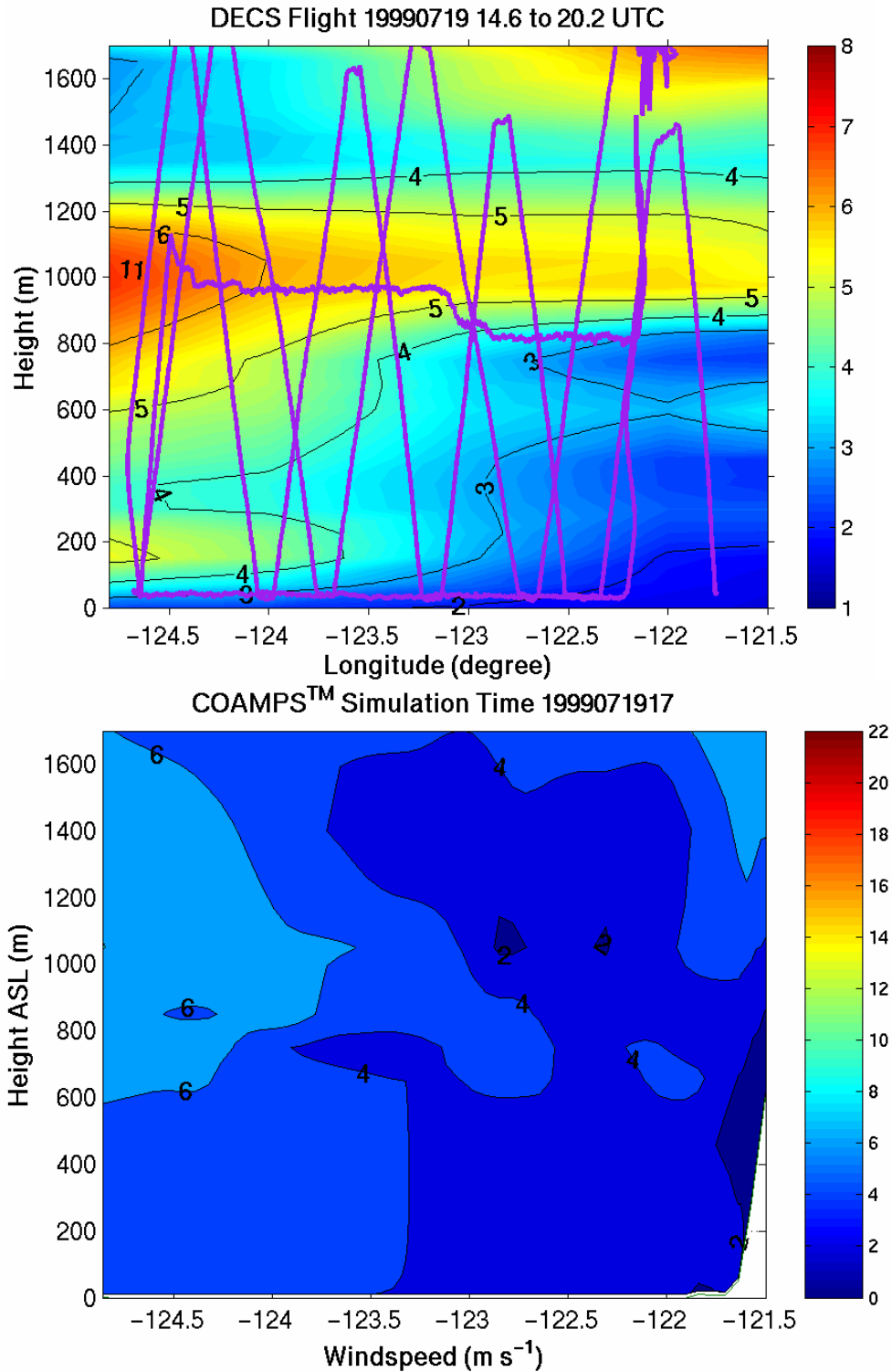


Figure 3.15: Comparison of wind speed (m s^{-1}) between the model and the observations. A solid line superimposed on the contour plot depicts the flight track for the observations. The COAMPS™ simulation is a five-hour forecast valid at 1700 UTC, close to the midpoint of the aircraft flight.

Forecast Time: 1999071017 UTC Observation Time: 17.02 Sounding 23

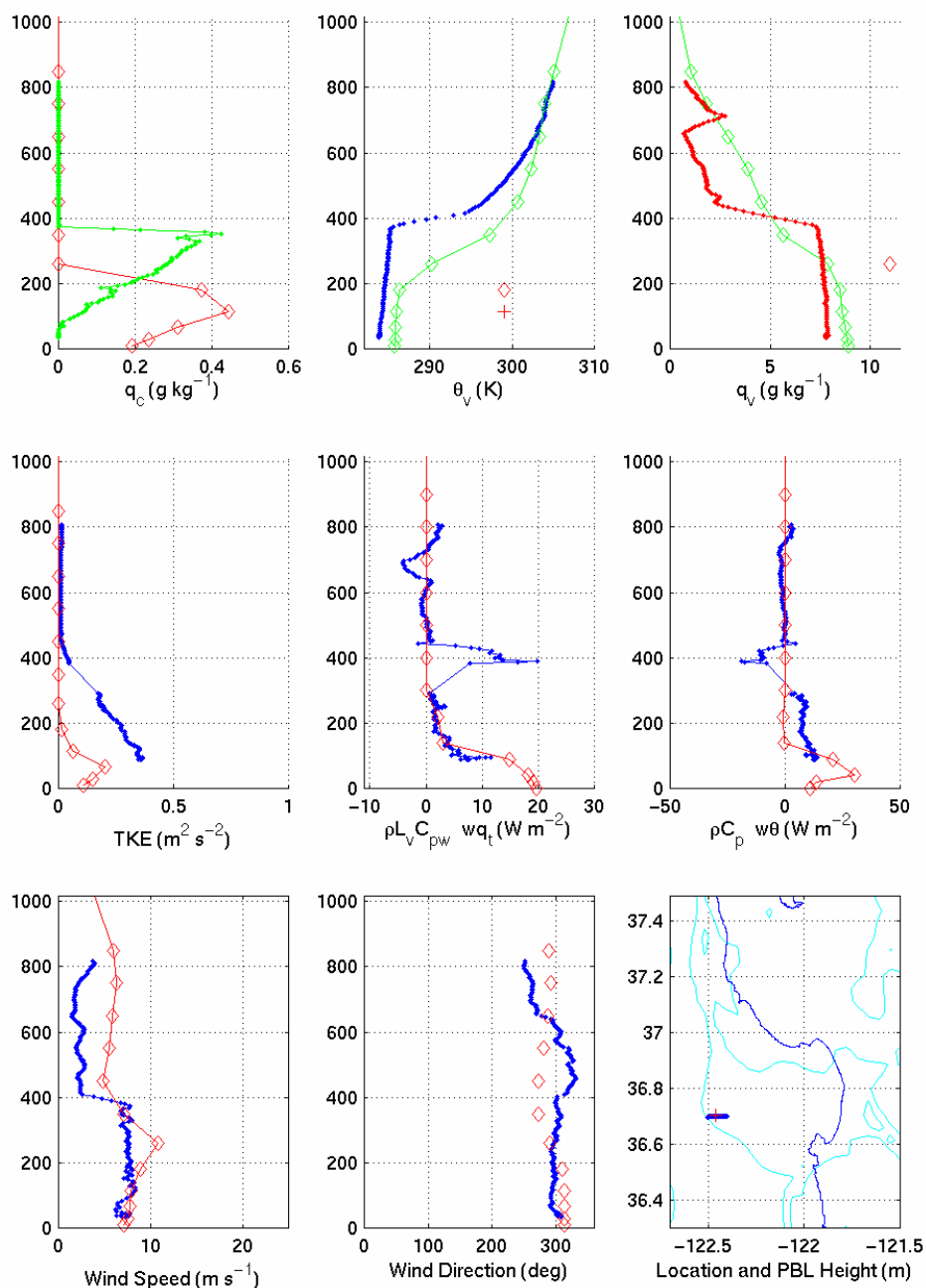


Figure 3.16. In cloudy cases the vertical profile of horizontal velocity (lower left panel) was often uniform with height in the boundary layer and dropped off rapidly above cloud top. COAMPSTM simulations frequently depicted a velocity maximum just above the boundary layer top, which matches the clear profile more closely.

Observed vs. Model Level Legs 19990717 16–17.7UTC 36.7 – 122.59

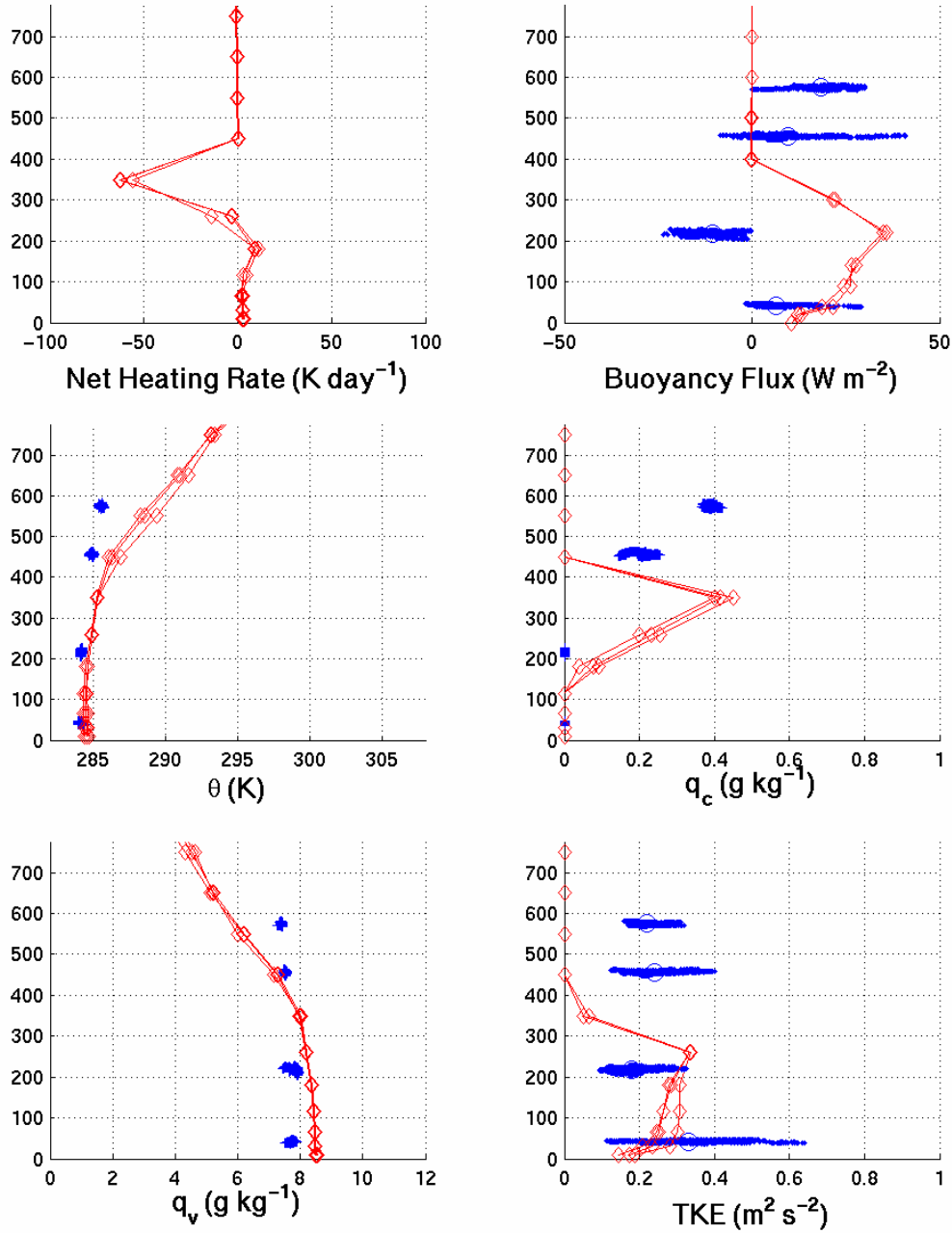


Figure 3.17. Typical profiles of observed values for aircraft level legs. Small scattered dots are individual data points and circles are mean values. Corresponding model profiles are solid lines marked with a diamond at each grid level. Note the in-cloud buoyancy flux maximum and sub-cloud minimum are under-resolved by COAMPSTM. Net radiative heating rate (upper left panel) is not available from the observations.

Forecast Time: 1999071618 UTC Observation Time: 18.13 Sounding 2

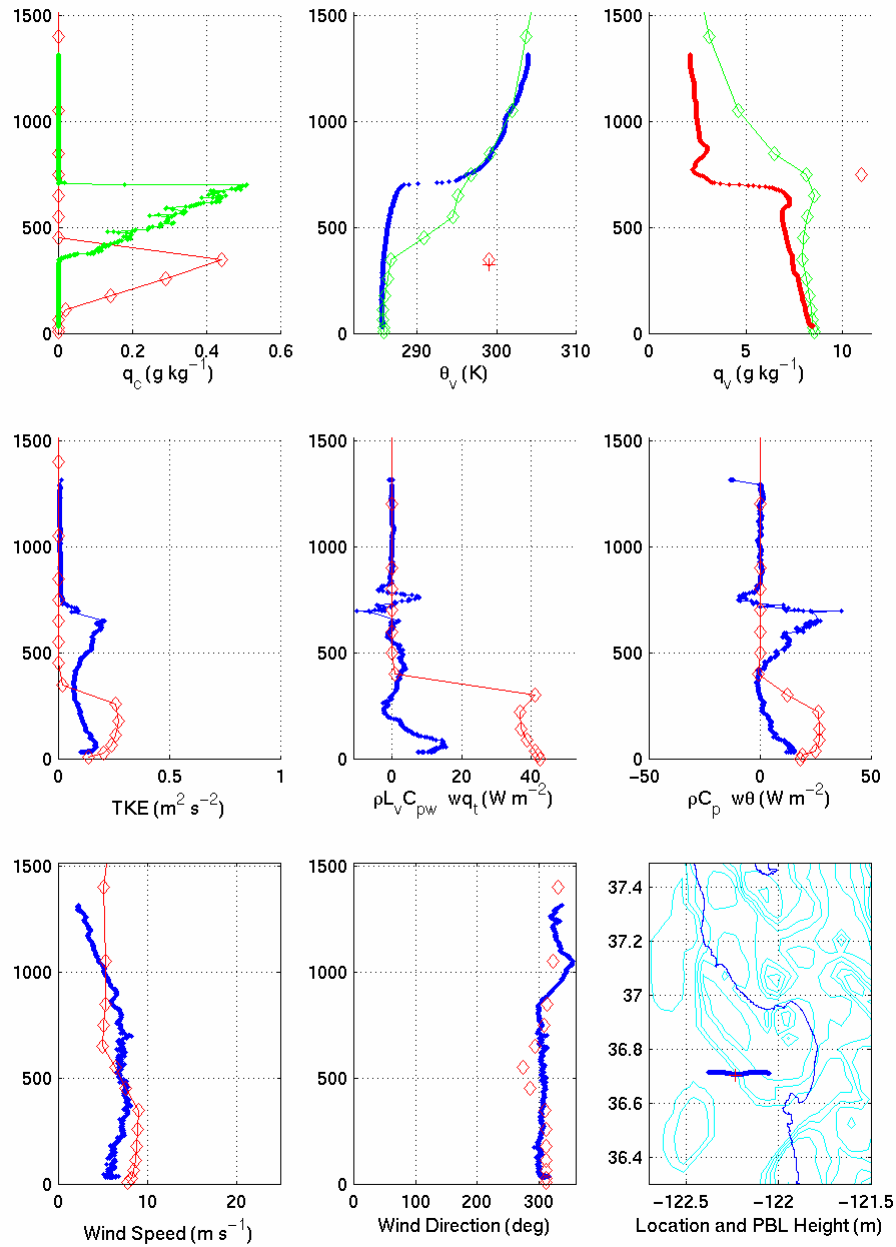


Figure 3.18. Typical model vertical profile (diamonds) and sounding profile (dark thick line) for a cloudy case with a minimal coastal jet.

Forecast Time: 1999070717 UTC Observation Time: 17.28 Sounding 13

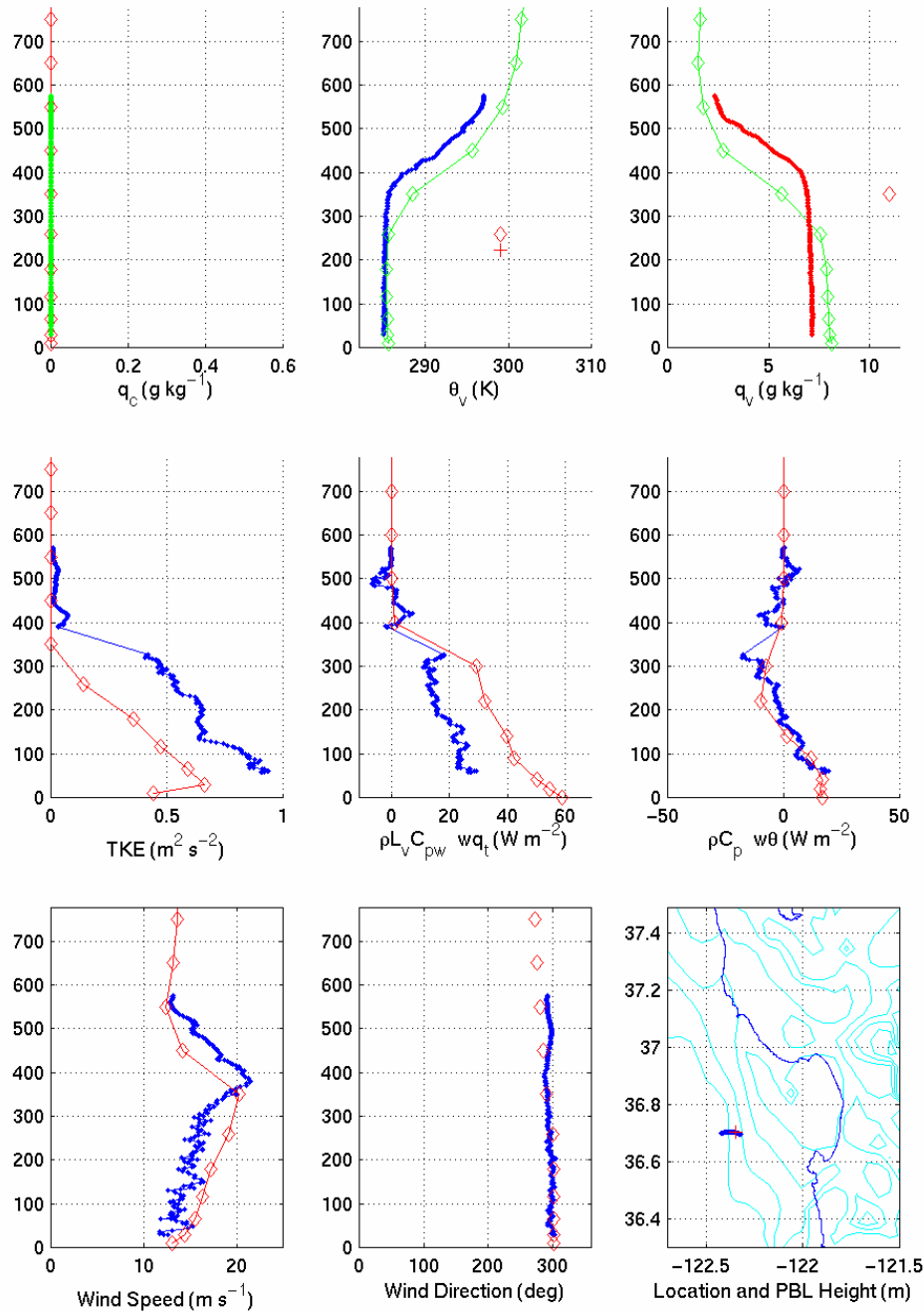


Figure 3.19. Typical model vertical profile (diamonds) and sounding profile (dark thick line) for a no-cloud case with a strong coastal jet.

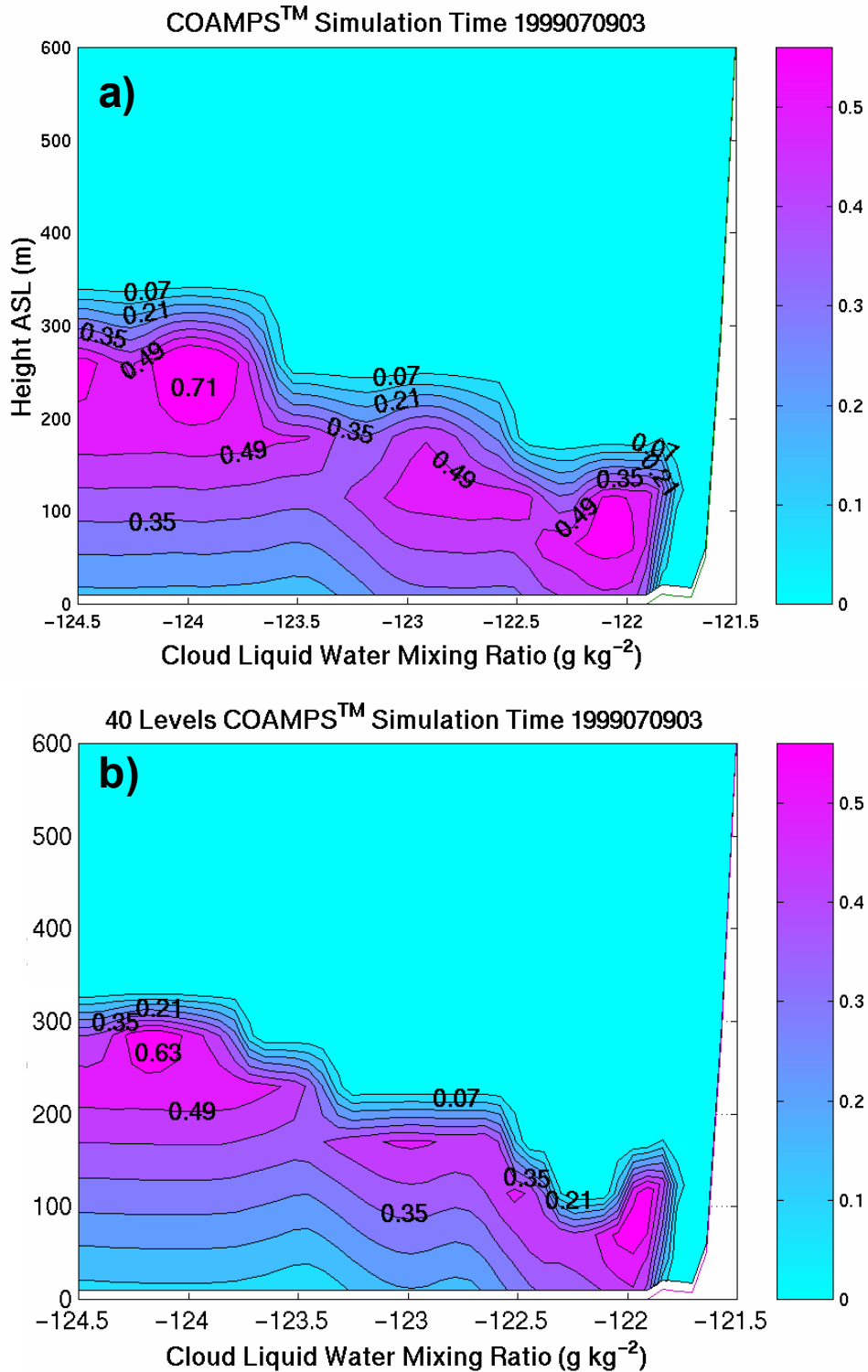


Figure 3.20. East-West cross-section at 37.1 N for: a) 30-level COAMPS™ at approximately 100 m vertical spacing in the boundary layer and b) 40-level COAMPS™ at approximately 50 m vertical spacing in the boundary layer.

1999070917 17.05 Sounding 8

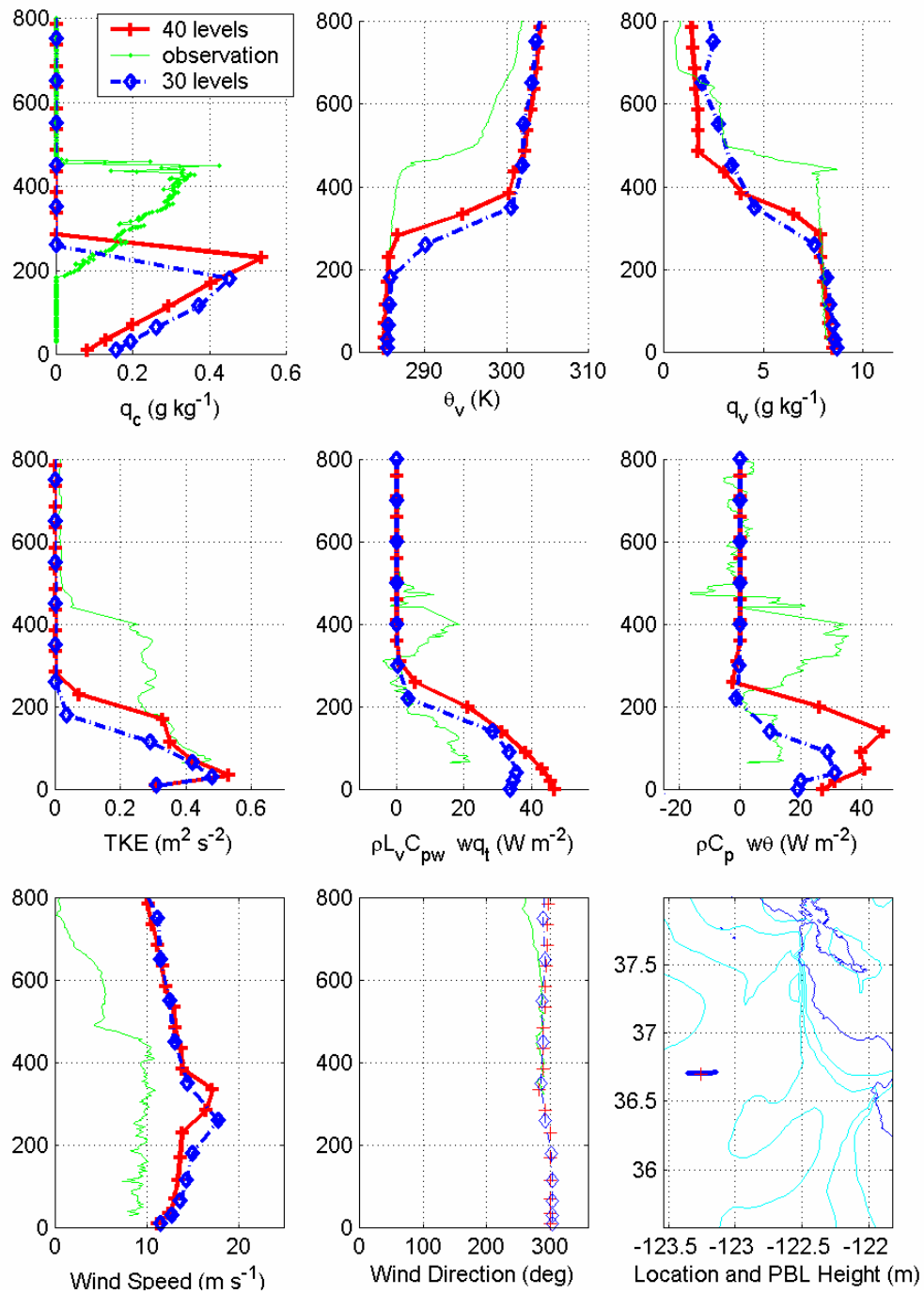


Figure 3.21. Comparison of CTBL structure for 40-level and 30-level simulations as discussed in the text.

IV. DEFINING THE BOUNDARY LAYER HEIGHT

A. OBJECTIVE

One of the most important aspects in being able to implement an explicit entrainment parameterization in COAMPSTM is to accurately identify the boundary layer top at which entrainment fluxes will be applied. This is challenging for a mesoscale model since the theoretical criteria for dynamic stability that use either turbulence fluxes (flux Richardson number) or vertical gradients (gradient Richardson number) at the interface generally are not applicable for the coarse vertical resolution used in mesoscale models. We will first examine the diagnostic boundary layer height using the existing method in COAMPSTM against those observed in DECS. Efforts are then made to search for alternative approaches to improve the diagnostic boundary layer height. This chapter focuses on better identification of the boundary layer top as a diagnostic quantity; however improvement of the prediction of the boundary layer properties and thus the boundary layer height can only come from modifications to the model numerics or physics. Modifying the model numerics with regard to entrainment parameterization is discussed in the chapters to follow.

As described in Chen et al. (2003) the diagnostic boundary layer depth is based on the lowest level at which the bulk Richardson number exceeds a critical value, which is set at 0.5 in the model. The theoretical basis for this is that when the flux Richardson Number is greater than a critical value, generally taken to be 0.25, the flow becomes non-turbulent. When the equations are cast in a finite difference form, the appropriate critical value at discrete grid levels becomes less certain. Previous research on MABL structure and evolution during the Coupled Boundary Layer Air-Sea Transfer (CBLAST) field study in Cape Cod, MA (Qing Wang, 2003, personal communication) indicated large discrepancies between model diagnosed boundary layer height based on the Richardson number (turbulence profile) and the inversion base height indicated by manual estimation from model sounding profiles. By examining a variety of boundary layer and inversion conditions and comparing modeled structure to aircraft sounding data, we refine the diagnostic method to ensure accurate representation in the model.

B. COAMPSTM DIAGNOSTIC BOUNDARY LAYER HEIGHT

The boundary layer top is the interface between the turbulent boundary layer below and non-turbulent tropospheric air above. As a result, the boundary layer top is characterized by a significant increase in Richardson number. Theoretically, this interface is best identified using the flux Richardson number:

$$R_f = \frac{\frac{g}{\theta} \overline{w' \theta'_v}}{\overline{w' u'} \frac{\partial U}{\partial z} + \overline{w' v'} \frac{\partial V}{\partial z}} \quad (4.1)$$

where the numerator and the denominator are the buoyancy and shear production terms of the turbulent kinetic energy (TKE) budget equation, g is gravity, θ_v is the virtual potential temperature, U and V are the mean horizontal wind components, and u' , v' , w' are the velocity perturbations. The flux Richardson number defines the dynamic stability of the flow. Under stable stratification, turbulence will cease if the buoyancy term is larger than the shear production term, specifically when $R_f \geq 1$. Thus a critical flux Richardson number of 1 can be used to define the dynamic stability of the flow. Alternatively, we can define a gradient Richardson number:

$$R_i = \frac{\frac{g}{\theta} \frac{\partial \bar{\theta}}{\partial z}}{\left(\frac{\partial U}{\partial z} \right)^2 + \left(\frac{\partial V}{\partial z} \right)^2} \quad (4.2)$$

where the gradient is used instead of the fluxes. The critical gradient Richardson number, R_{ic} , was deduced to be $1/4$ for inviscid stability by Miles (1961). Measurements suggests that the range of R_{ic} is $R_{ic} \approx 0.2 \sim 0.25$ (Garratt, 1992). In a numerical model with finite vertical resolution, the gradient Richardson number is replaced by the bulk Richardson number defined as:

$$R_b = \frac{\frac{g}{\bar{\theta}} \Delta \bar{\theta} \times \Delta z}{(\Delta U)^2 + (\Delta V)^2} \quad (4.3)$$

Because of the bulk approximation, the critical bulk Richardson number, R_{bc} , is often not the same as R_{ic} . In fact, when the grid resolution is coarse (i.e., large Δz) sub-critical Richardson number values are almost certainly present in thinner layers within the vertical grid interval, implying that there are sub-grid scale fluxes supported by the smaller-scale turbulence. This effect is allowed for by increasing the magnitude of the critical Richardson number as is currently done in COAMPSTM (Chen et al., 2003) where the critical bulk Richardson number is set at 0.5. In addition, COAMPSTM interpolates linearly between grid levels to estimate the exact height where the Richardson number exceeds the critical value. Thus, the diagnosed boundary layer height may not be at the grid levels.

As was discussed in Chapter III, comparison between the COAMPSTM diagnosed boundary layer height and observations indicates significant under-prediction of the boundary layer height. We theorize that this discrepancy is likely because either: 1) the boundary layer height was diagnosed inappropriately from the model output or 2) the boundary layer properties were predicted inappropriately. The work in this chapter intends to identify and improve the error caused by an inappropriate boundary layer top diagnostic scheme.

To find a better diagnostic indicator for boundary layer height, one needs a variable independent from the bulk Richardson number. For the stratocumulus-topped boundary layer, a natural choice is the cloud top. Since liquid water generally increases with height in stratiform marine clouds and rapidly drops to zero just above the maximum value (Albrecht et al. 1988), the cloud top can be considered as the height where cloud liquid water reaches a maximum. Figure 4.1 shows a comparison between the height of maximum liquid water content (cloud top height) and the boundary layer height from all DECS soundings made by the Twin Otter. Here the boundary layer height was selected manually from the height at which the largest gradients in total water mixing ratio and liquid water potential temperature are co-located. As can be seen in Figure 4.1, the two

variables are nearly the same with a mean difference of about 12 m. Thus the observations show that the cloud top height is indeed a good indicator for boundary layer height in this regime. Since we are primarily concerned with the CTBL in this study, this is a useful indicator for boundary layer height, while another approach such as the stability criteria or gradient strength would be more appropriate for the clear case.

C. COMPARISON OF OBSERVED AND SIMULATED BOUNDARY LAYER HEIGHT

Using cloud top height as a measure, boundary layer height was diagnosed using several different indicators including the Richardson number criteria and was compared to a variety of observed and modeled thermodynamic variables including the cloud top height, and the vertical gradients of liquid potential temperature gradient ($d\theta_l/dz$) and water vapor mixing ratio (dq/dz) based on the fact that largest gradients of these are at the boundary layer top in the typical marine CTBL. We refer to these methods as the inversion strength methods and the cloud top height method for consistency. The comparison shown in Figure 4.2 was done between the model and the observations for 450 model forecast soundings valid at the time and location of the sounding flight legs for the twenty DECS flights. The Richardson number-based method interpolates between grid points to estimate the exact height where the Richardson number exceeds the critical value while the inversion strength method is at the height of the closest grid point. Consequently, overlapping/clustering of data points at grid levels occurs so some of the spread is due to the revised methods being diagnosed on the discrete grid levels and the current method being interpolated between levels. However, even with taking the variance due to interpolated versus discrete grid level into account, the thermodynamic gradient methods show improvement. Vertical grid spacing is about 100 m as discussed in Chapter III.

Testing the sensitivity of the resultant boundary layer height on choices of the diagnostic criteria was done for each of the methods discussed above. Results shown in Figures 4.2b and 4.2c are considered the best results for the inversion strength methods, where an empirical value of 0.02 K m^{-1} were chosen as the criterion for θ_l gradient and

an empirical value of $-0.0065 \text{ g kg}^{-1} \text{ m}^{-1}$ was chosen for the q_t gradient. These critical gradient values are empirically derived for this dataset and would likely be sensitive to the strength of the subsidence and surface forcing when the CTBL is at approximate equilibrium.

The comparison between the cloud-top height and the other boundary layer diagnostics schemes suggests that the θ_l gradient method diagnoses boundary layer heights that are closest to the cloud top height with a difference of less than 20 m (Figure 4.2b). The Richardson number based boundary layer height is in general lower than the cloud top height by about 128 m (Figure 4.2a), while the boundary layer height based on total water gradient over-estimated the boundary layer height by about 80 m and had the largest scatter (Figure 4.2c). In the observations, excellent correlation was found between the maximum cloud liquid water mixing ratio and the inversion base, as expected from our conceptual model of the general structure of stratocumulus-topped boundary layers (e.g. Brost et al. 1982a and 1982b, Albrecht et al. 1988, Paluch and Lenschow 1991).

In comparing the observed inversion height to the modeled height, it was also found that, in addition to the low bias of 200 meters discussed previously, under certain conditions the Richardson number based method diagnoses a height 600-700 meters lower than observed. Further investigation determined that in these cases, a weakly stratified sub-cloud layer existed that met the criteria for non-turbulent flow. An example of the temperature and moisture structure in these cases is given in Figure 4.3. This structure could occur in a decoupling case, when the turbulence in the cloud layer is maintained by in-cloud forcing and non-surface generated mixing. While this height meets the definition of being the first non-turbulent layer from the surface, and may be useful in other applications such as determining electromagnetic propagation conditions, our interest is in reliably diagnosing the main capping inversion at cloud top. Using the inversion strength method would eliminate the false boundary layer definition in decoupling conditions.

D. AN ALTERNATIVE METHOD FOR DIAGNOSING THE MODEL BOUNDARY LAYER HEIGHT

Based on these results, an alternative method was formulated and implemented in COAMPSTM using the gradient method, which calculates the liquid potential temperature gradient (θ_l) to diagnose the boundary layer height and then bases the inversion height on the lowest level at which $d\theta_l/dz$ exceeds a critical value. This method seems to work well for the cloudy boundary layers where strong temperature gradient is found at the top of the boundary layer. However, it may be problematic in clear conditions or when the boundary layer top has a weak temperature gradient. Since the Richardson number-based boundary layer height works rather well for the clear boundary layer, for implementation in the 3-D COAMPSTM, we used a hybrid approach that adopts the θ_l gradient for the cloud-topped boundary layer and the Richardson number for the clear boundary layer. As an alternative, we simply used the cloud top height, defined as the level with maximum cloud liquid water, as the boundary layer height for the cloudy condition. This final approach was used for implementing explicit entrainment parameterization. Although the θ_l gradient method worked well as a diagnostic in the control runs, in single column testing of the explicit entrainment parameterization we found that any method which uses either a turbulence-based or thermodynamic gradient stability criteria would oscillate between grid points when the boundary layer was changing in height. This oscillation created stability problems and unrealistic entrainment velocities in the forecast model so the boundary layer height diagnostic was modified to determine the inversion from cloud top height and a relaxed critical Richardson number-based criterion above the level of maximum liquid water content. A logical, consistent, and stable method for determining boundary layer height on a discrete grid for the time-evolving boundary layer still needs further research. Furthermore, the methods used here are particular to our regime of interest and focus on the marine CTBL. A method that works equally well in identifying the boundary layer height for the CTBL, the dry convective boundary layer, and stable boundary layers over land and water is required, although the current Richardson-number based method is expected to work better in non-cloudy boundary layers without sub-cloud weakly stable layers.

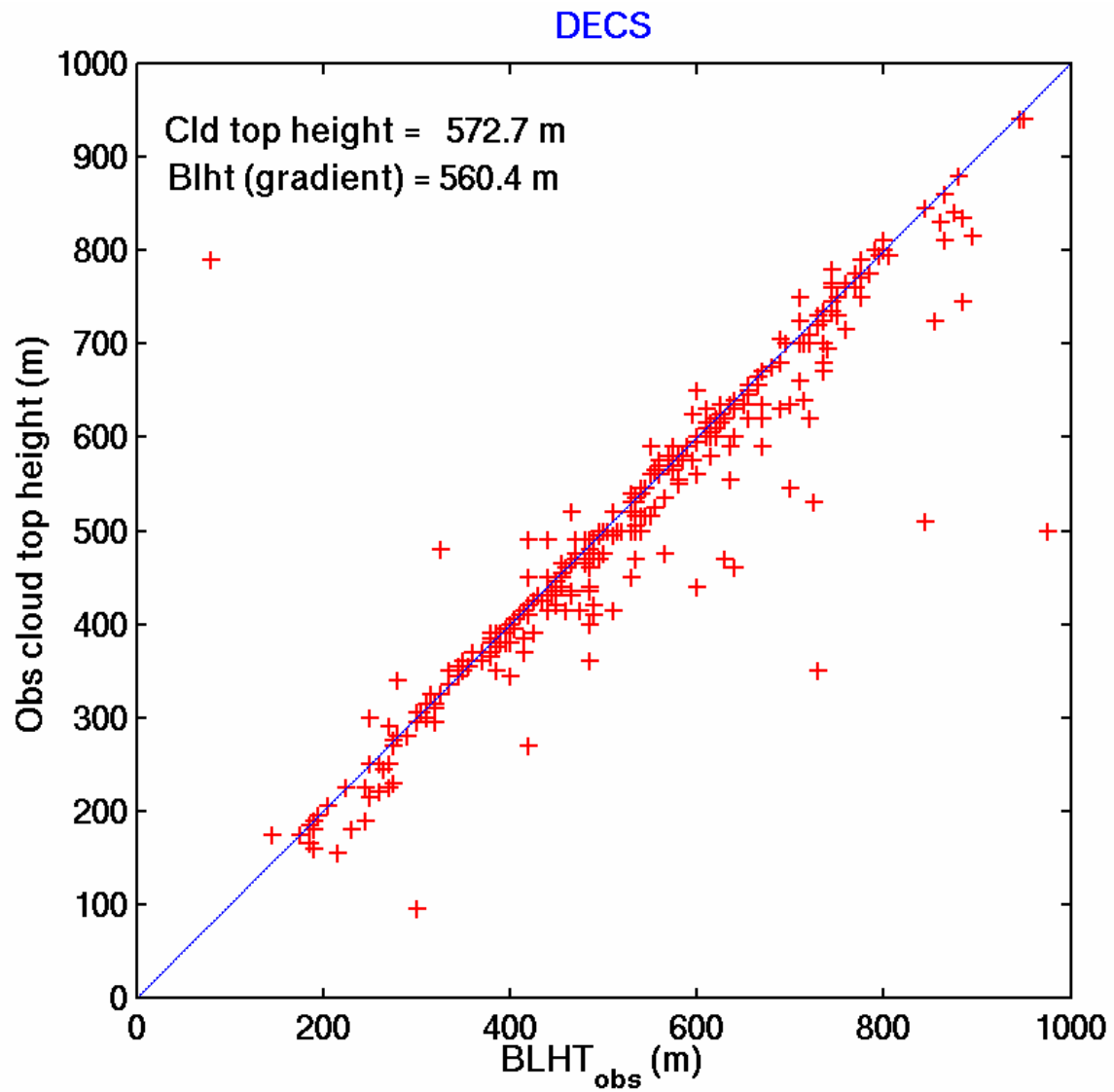


Figure 4.1. Comparison of the observed cloud top height and the observed inversion height based on the vertical gradient of virtual potential temperature.

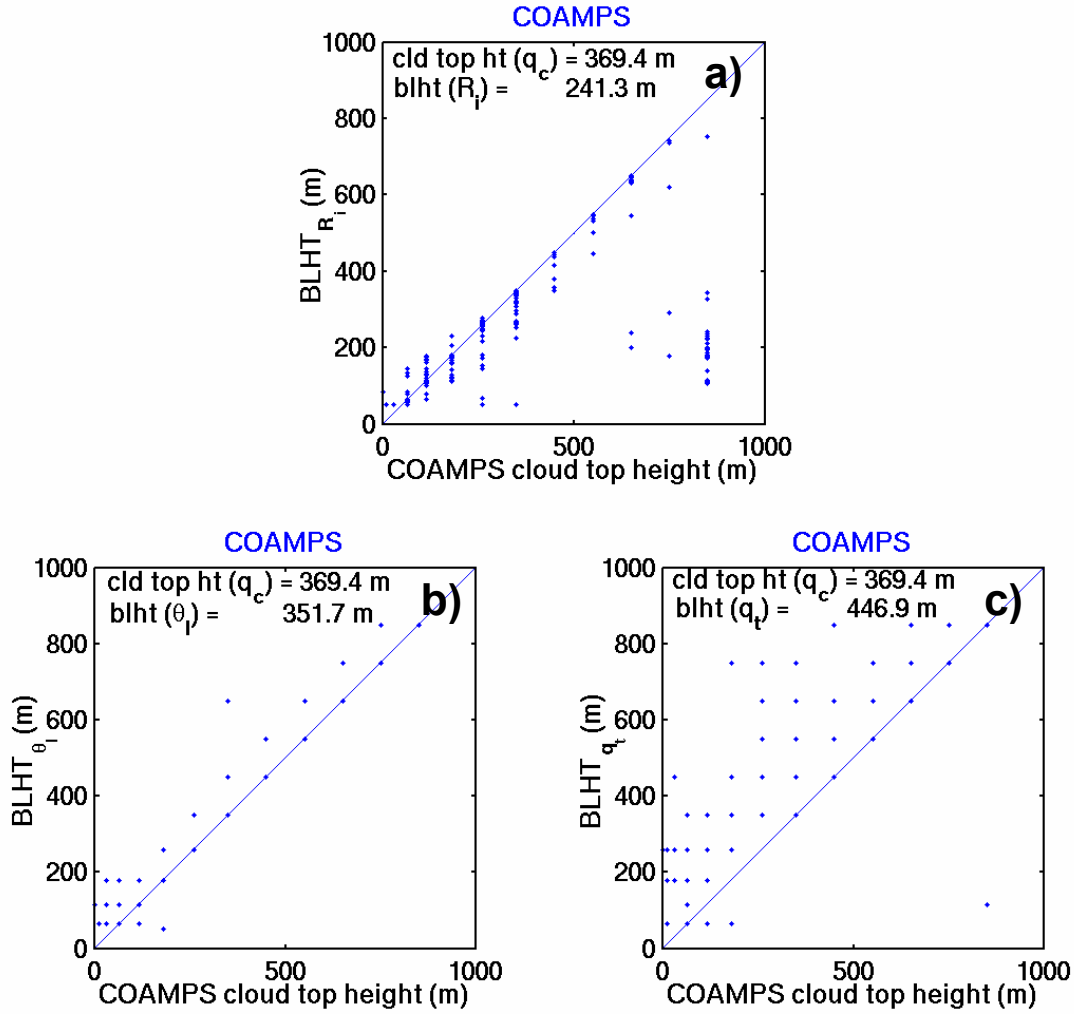


Figure 4.2. Comparison of a) the current method of determining the boundary layer height based on the lowest level at which the bulk Richardson number exceeds a critical value and revised methods based on vertical gradients of b) liquid potential temperature and c) total water mixing ratio exceeding an empirically derived critical value. In the case of weak inversions that do not meet the criteria, the new method defaults to the original method. Note that the liquid potential temperature gradient shows the best match with cloud top height and does not mis-diagnose the sub-cloud inversion as the boundary layer height.

July 14, 1999 180 UTC Sounding 14

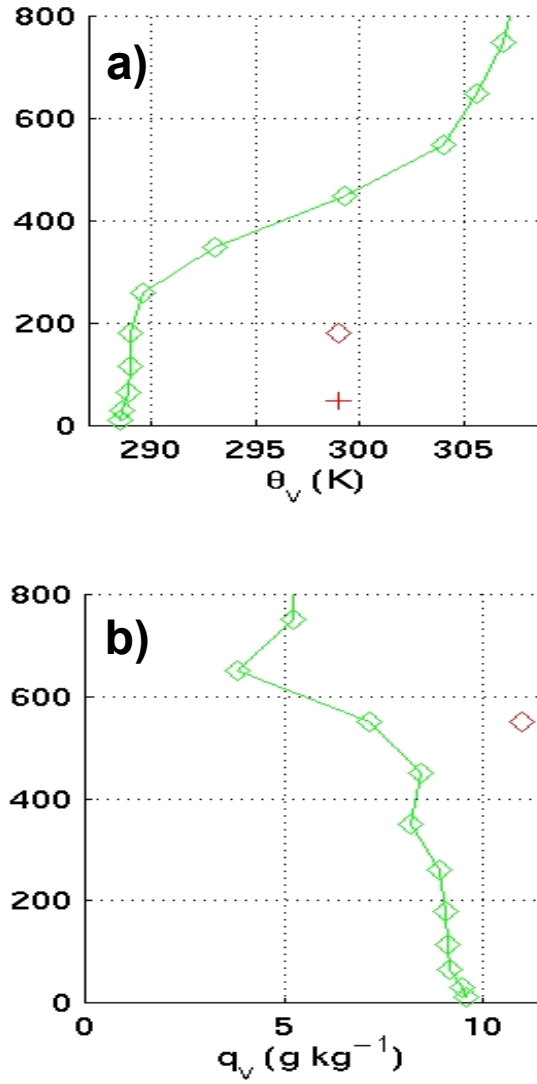


Figure 4.3. Example of mis-diagnosis of the boundary layer height using the current method in COAMPSTM. Diamond indicates the diagnosed height from the revised method based on the θ_l or q_v gradient. Plus sign is the result from the original method.

THIS PAGE INTENTIONALLY LEFT BLANK

V. EXPLICIT ENTRAINMENT PARAMETERIZATION

As discussed in Chapter II, the current COAMPSTM boundary layer parameterization represents the turbulent entrainment at the boundary layer top through the K closure, which we refer to as the implicit method. Such an approach has advantages because it is simple to implement since it requires no special treatment of the boundary layer top and the inversion thermodynamic structure, and it is a TKE-forced, physically based parameterization. However, it may not be able to deal with entrainment effectively without changing the mixing within the boundary layer. An effective treatment for the entrainment process is to implement an explicit entrainment parameterization (EEP). Implementing EEP provides us a framework that allows us to focus on the boundary layer top in order to realistically represent the entrainment process. In addition, EEP allows us to more easily test new parameterizations for entrainment velocity as they emerge.

There are three components to implementing an EEP: determining the altitude at which to apply entrainment flux; specifying ΔX , X being a predicted mean quantity; and incorporating the entrainment fluxes into COAMPSTM. In Chapter IV, we discussed various methods for correctly identifying the boundary layer height. In this chapter, we will focus on defining the boundary layer top jump conditions and implementation of EEP into COAMPSTM. Results from testing the EEP implementation in single column model (SCM) COAMPSTM will be presented to illustrate the role of EEP in modifying the boundary layer cloud and thermodynamics.

A. EXPLICIT PARAMETERIZATION CONCEPT AND FORMULATION

As discussed in Chapter II, representing entrainment flux at the CTBL top requires specification of both the entrainment velocity (W_e) and the inversion jump condition (δX). The latter is associated with changes in the quantity (X) across the inversion base. Figure 5.1 gives an example of the vertical variation of potential temperature and water vapor mixing ratio typically found across the inversion for the

CTBL. In this example, the observed change in virtual potential temperature is about 12 K in a layer of about 70 m in depth. The decrease in total water is about 4 g kg^{-1} within the same depth. These sharp variations justify the assumption of a discontinuity or “jump” condition usually implemented in one-dimensional mixed layer models. In reality, the inversion height undulates horizontally due to surface forcing inhomogeneity and mesoscale convective circulations (Atkinson and Zhang 1996), which may result in discrepancies between the model representation of the jump height as compared to point observations. Evidentially, such sharp gradients cannot be represented in operational mesoscale forecast models such as COAMPSTM which typically use a vertical spacing of 100 m or larger. To properly represent a jump across a 50 m entrainment zone, one would expect to need vertical resolutions on the order of 10-25m (2-4 ΔZ).

Because of the presence of the sharp inversion, the representation of entrainment fluxes becomes very sensitive to the vertical resolution of the model. Lenderink and Holtslag (2000) demonstrated that simple turbulence closure models such as a 1.5 order prognostic-TKE diagnostic-length scale (E-1 scheme) formulation can adequately represent entrainment at vertical spatial scales of 25 meters and temporal scales of 1 second, but degenerate rapidly when approaching the relatively coarse resolutions currently used in operational mesoscale prediction models of 100m and 120s. Consequently, special considerations are needed in representing the inversion jump condition in addition to using appropriate entrainment parameterizations. Lenderink and Holtslag propose representing the sub-grid jump condition by looking at the total energy, which is conserved, but requires taking into account the radiative flux divergence in addition to the thermodynamic fluxes.

Grenier and Bretherton (2001) proposed three specific methods employing conservation of total energy for representing entrainment at the inversion height at operational grid resolutions. As depicted schematically in Figure 5.2, these are the “prognostic inversion” using MABL depth as a prognostic variable, the “reconstructed inversion” using grid level thermodynamic variables to reconstruct the MABL height and capping inversion strength, and the “restricted inversion” forcing the inversion to lie on a flux level of the host model grid. The first method is not appropriate for models with

fixed vertical grid levels such as COAMPSTM and the third method, although the simplest to implement, did not perform well for the CTBL case using SCM tests of a 1.5 order turbulence closure model (TCM). We initially implemented the reconstructed inversion method in SCM testing in COAMPSTM, however, we were unable to produce a numerically stable three dimensional model, so we reverted to the simpler restricted method during initial development.

Both of these methods have been tested by Grenier and Bretherton (2001) with generally good results, although the reconstructed inversion method was found to be highly sensitive to the vertical advection scheme. In Grenier and Bretherton (2001), the reconstructed inversion method combined a 1.5 order TCM with an explicit entrainment parameterization by using the TCM to determine the fluxes at all levels below the grid level (M), which is the closest model level at or below the inversion height (i). For the next highest flux level (M+1/2), the entrainment velocity (W_e) is first calculated at the inversion using the Turner-Deardorff entrainment parameterization with a local closure assumption as discussed in Chapter II and depicted in Equation 2.5, repeated here as Equation 5.1 for clarity.

$$We = A_L \frac{e^{3/2}}{l^i \Delta_i b} \quad (5.1)$$

This entrainment rate is then related to the entrainment flux through Equation 5.2 below and extrapolated to the model flux level. The fluxes at level M+3/2 are assumed to be zero by definition. The term “reconstructed inversion” refers to the method of determining the appropriate values for the state variables at the inversion based on values at discrete grid levels. In this case a height weighted average based on the diagnosed inversion height (i) of the values at X_M and X_{M+1} is used for any scalar (X). In the restricted inversion method, the jump condition and the radiative flux and thermodynamic values for the entrainment parameterization are simply determined from the values at grid level.

As reported in Lock (2001), Lock et al. (2000), and Martin et al. (2000), the reconstructed inversion method has been implemented in the United Kingdom

Meteorological Office (UKMO) Unified Model (UKUM) with good results on the GCM scale in depiction of StCu to Cu transition and mixed results on the mesoscale in depiction of frontal and orographically forced stratus. The ABL parameterization in the UKUM is based on non-local TKE closure following Holtslag and Boville (1993) where the TKE profile is prescribed and the magnitude is diagnosed based on the surface forcing. The original scheme is modified by an additional profile to account for mixing driven by cloud top radiative cooling following the work reported in Van Meijgaard and van Ulden (1998). This entrainment scheme is modified as discussed in Lock (2001) to adjust for unphysical entrainment effects due solely to the numerical scheme resulting from calculating entrainment on separate grid levels from the model radiation, cloud microphysics and divergence. This effect, termed “numerical entrainment” is discussed in more detail in Lenderink and Holtslag (2000). Using a 1.5 order TCM in SCM tests as compared to LES results, Lenderink and Holtslag (2000) found that, at the coarse vertical resolutions found in operational prediction models, under-prediction of turbulence was compensated for by the numerics of representing large-scale subsidence and clouds in Eulerian grid boxes so that the resulting entrainment rates looked reasonable. This is highly undesirable in an operational setting and should be taken into account in explicit entrainment parameterizations. In our formulation we account for cloud top radiative cooling and evaporative enhancement but the sensitivity of the resulting boundary layer height in the mesoscale prediction model to the vertical advection scheme under subsidence discussed in Lenderink and Holtslag (2000) requires further research.

Forecast Time: 1999071016 UTC Observation Time: 15.58 Sounding 4

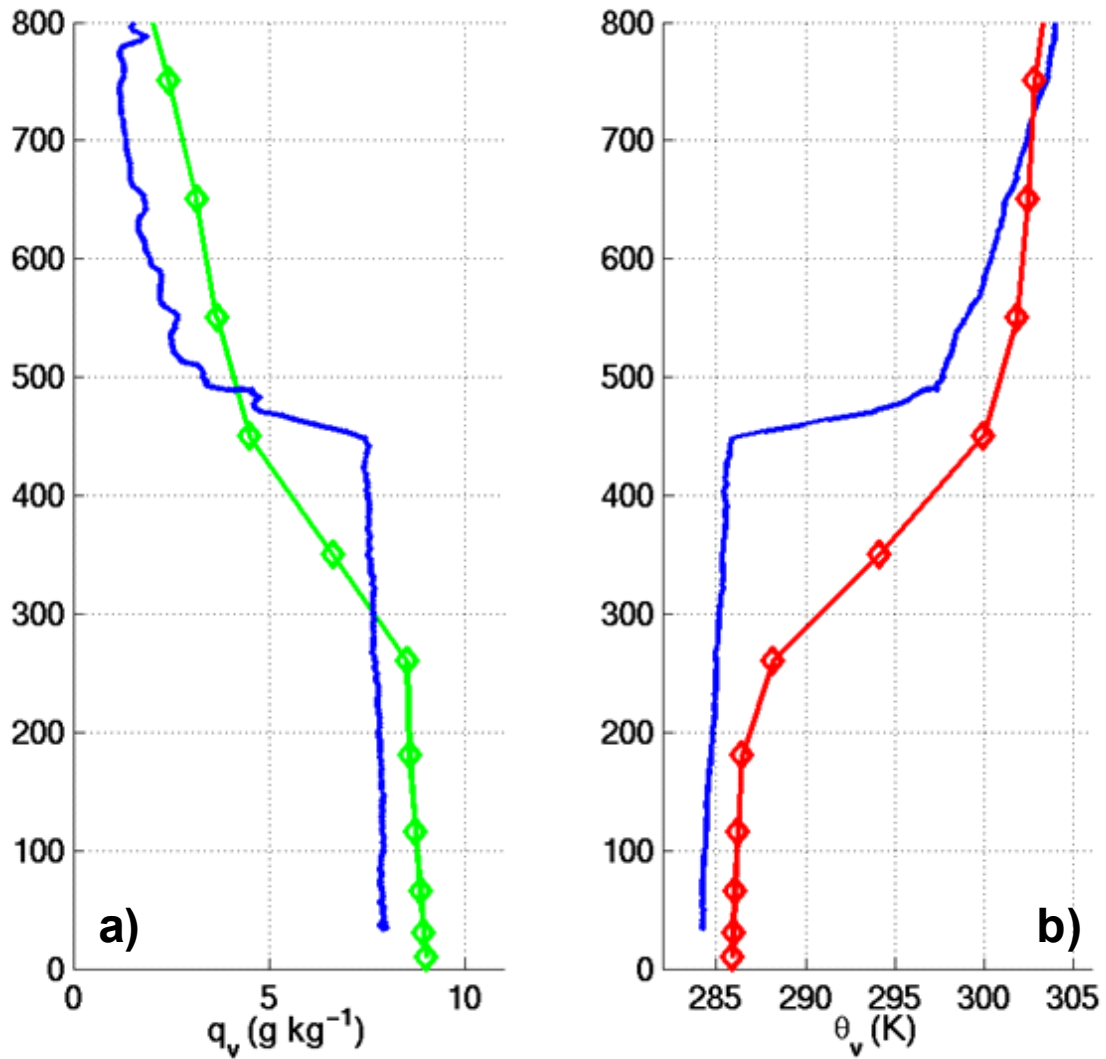


Figure 5.1. Example of observed (solid line) and modeled (diamond marker) profiles for a) water vapor mixing ratio (g kg^{-1}) and b) virtual potential temperature (K) for the stratocumulus topped boundary layer.

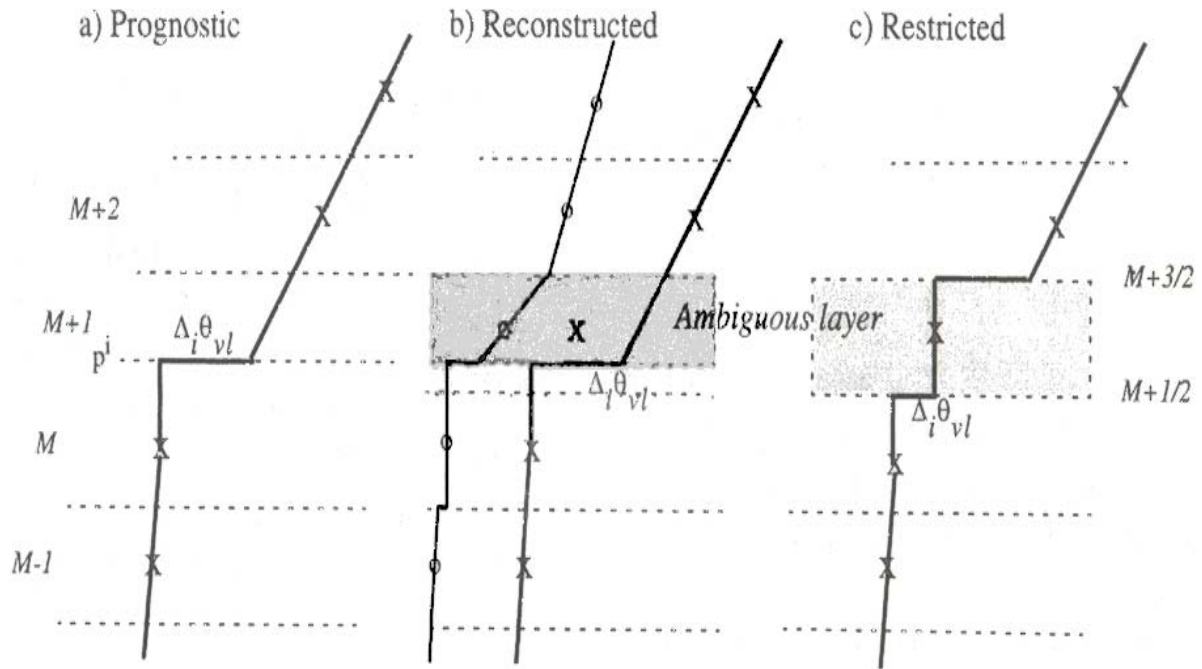


Figure 5.2. Sketch of the three approaches described in the text for treating the inversion in a numerical model. Dashed lines indicate flux levels, x's indicate grid levels. In (b), O denotes the profile of another arbitrary conserved scalar X. From Grenier and Bretherton (2001).

B. TESTING EEP IN SCM COAMPSTM

Following Grenier and Bretherton (2001), an explicit entrainment parameterization was coded and tested in COAMPSTM. Once the framework was developed, various methods for identifying the boundary layer height, parameterizing the entrainment velocity, and introducing the resultant fluxes back into the forecast model were tested. Our general approach was to diagnose the jumps in vertical gradients of the virtual liquid potential temperature gradient (θ_{vl}) and total water (q_t), which are conserved for moist adiabatic processes, and calculate the entrainment velocity from Equation 5.1. The entrainment flux for any scalar (X) can then be calculated from Equation 5.2. At the boundary layer top, the relationship in Equation 5.3 can be applied and once the entrainment fluxes for heat and total water are determined, a new eddy diffusivity constant (K_{H_INV}) can be calculated by inverting the flux-profile relationship as in Equation 5.4. COAMPSTM does not explicitly use the turbulent fluxes to predict the mean variables but rather calculates the eddy diffusivity (K_H , K_M , K_e) based on the predicted TKE from the budget equation. The resulting TKE, mixing lengths, vertical gradients of the scalar quantities, and surface fluxes are then passed to a linear solver which uses a tri-diagonal matrix to modify the vertical profile of the mean scalar quantities. Therefore, the entrainment diffusivity constant can then be used in place of the eddy diffusivity constant from the main TCM for both the prognostic equation in the TKE budget and in the scalar mixing routines for the next timestep.

Once the entrainment velocity is diagnosed, the entrainment flux for any scalar (X) is then determined from:

$$\overline{w'X'} = -W_e \Delta_i X \quad (5.2)$$

The effects of the explicit entrainment parameterization are introduced into the TCM in COAMPSTM by using the relation:

$$\overline{w'X'}_{INV} = -K_{H_INV} \frac{\Delta X}{\Delta z} \quad (5.3)$$

where K_{H_INV} is the eddy diffusivity at the boundary layer top. Combining Equation 5.2 and 5.3, we have:

$$K_{H_INV} = W_e \Delta z_{INV} \quad (5.4)$$

This is then used in place of the eddy diffusivity from the main TCM at the boundary layer top to further calculate buoyancy flux used to obtain the time rate of change in TKE and for turbulent mixing of scalar variables.

Special considerations were given to buoyancy flux just below the boundary layer top for coarse resolution mesoscale models. It is well recognized that cloud-top radiative cooling is a major forcing of turbulence in the cloudy boundary layers (e.g., Nicholls 1985, Lilly 1968). This radiative cooling, normally occurring in a layer of less than 100 m near the cloud top, cannot be well represented in general mesoscale models with a vertical resolution of 100 m or more. Therefore, it is advantageous to explicitly represent in-cloud radiative cooling in the buoyancy flux in order to capture the forcing of turbulence by cloud-top longwave cooling even at lower resolutions. Equation 5.6 below is used for buoyancy flux at the boundary layer top following Grenier and Bretherton (2001):

$$P_b^i = \frac{g}{\theta_{vl}} \left[\frac{\delta^{M+1} F}{C_p (\rho \Pi)^{M+1}} + \overline{w' \theta_v'^i} \right] \quad (5.6)$$

where P_b^i is the buoyancy production term in the TKE budget equation, $\delta^{M+1} F$ is the difference of the net radiative flux at the interface between cloud and clear, and $\overline{w' \theta_v'^i}$ is the entrainment flux.

In the single column model the effects of entrainment can be easily seen. Sensitivity tests were made on variables involved in the explicit entrainment parameterization. We first examined the sensitivity of the entrainment velocity formulation to the choice of the TKE value (e) in Equation 5.1. Strictly speaking, one should use the TKE at the diagnosed boundary layer top. However, because of the discontinuity involved when the boundary layer top jumps from one grid level to the next, using the TKE at the boundary layer top may introduce discontinuities in the results. Alternatively, we use the layer-averaged TKE in Equation 5.1 which reduces the discontinuity and reduces the tendency to produce unrealistically large entrainment

velocities when the inversion height is changing grid levels. Using the layer average reduces noise in the model and the growth of the boundary layer and the boundary layer thermodynamics remain about the same. In the full 3-dimensional model, it was found that the method for calculating the mean TKE would produce spurious values, so the results presented in this chapter were obtained using the TKE at one level below the inversion, the magnitude of which was found to be comparable to the mean TKE in the SCM.

Several formulations for calculating the entrainment velocity and introducing it into the mixing were tested. The results presented here use the TKE at one level below the inversion ($k_{\text{inversion}}+1$) in the calculation of the entrainment velocity, which is then introduced into the TKE budget equation as the eddy-mixing coefficient (K_H) at the inversion level. Analysis of the average TKE for the boundary layer compared to the value at $k_{\text{inversion}}+1$ indicates that this value is approximately equivalent to using the layer-integrated average TKE in Equation 5.1 and is easier to implement. The scalar mixing routines interpolate the K_H profile to flux levels before calculating the vertical gradient of the mean scalar quantity and the resulting fluxes. As this tends to reduce the effect of the explicit entrainment parameterization, which is now applied at the mean grid level rather than the flux level in the restricted inversion, the diagnosed K_{H_INV} was applied directly at the flux level in the mixing routines.

EEP implemented in COAMPSTM was tested in a SCM version of COAMPSTM before it was run in 3-D mode. The SCM testing allows us to understand the behavior of the new parameterization implementation. Figure 5.3 shows the initial/upper air conditions used to force the SCM simulations. Here, our SCM testing did not incorporate the effects of large-scale subsidence. Because large-scale subsidence is not included, an equilibrium solution is not expected even though the sea surface temperature remains constant ($T_{\text{sst}}=290$ K) and boundary layer growth continues through the simulation period.

The effects of vertical resolution were examined in the SCM with control and EEP tests done for 30 vertical levels at 100 m spacing in the boundary layer and 40 levels at 50 m spacing. We found that increased resolution resulted in faster boundary layer

growth and reduced liquid water content in both the control and EEP simulations (not shown), indicating that the implicit method approaches the explicit method at higher vertical resolutions. However very fine vertical resolution makes this sensitivity testing less applicable to development for use in operational mesoscale models.

The results from SCM testing are shown in Figures 5.4 to 5.10. Figure 5.4 shows a comparison of the cloud water between the control run and the EEP simulation. In addition to the elevated cloud layer, the EEP run produces less cloud water compared to the control run. Entrainment velocity and the associated fluxes are shown in Figure 5.5 and the cloud top jumps in liquid potential temperature ($\Delta\theta_l$) and total water (Δq_t) are shown in Figure 5.6. Here mean entrainment velocities (Figure 5.5a) are on the order of 0.5 to 3.0 cm s⁻¹ while larger values of 3 to 10 cm s⁻¹ are observed early in the simulation and just before the diagnosed inversion jumps to the next level. This range of entrainment velocities is generally larger than observed values of 0.4 cm s⁻¹ for similar conditions during the Dynamics and Chemistry of Marine Stratocumulus experiment (DYCOMS) (Stevens et al. 2003a) but, given the large uncertainty in field measurements of entrainment velocity, are still acceptable. The entrainment fluxes in the first 10 hours of cloud formation are large, with average values to about -75 W m⁻² for liquid water potential temperature flux and 100 W m⁻² for total water flux. Since Figure 5.6 shows reasonable values of the cloud top jump conditions in $\Delta\theta_l$ and Δq_t , this overestimate of entrainment flux is likely a result of strong turbulence in the early hours of cloud formations (Figure 5.7). The cloud top jump conditions in Figure 5.6 show a pattern of sharp increases in the jump strength followed by gradual decrease. This is because in a growing boundary layer, the boundary layer top is identified on a discrete grid level, at which the jump gradually decreases in magnitude due to entrainment mixing until the boundary layer top is diagnosed at the next higher level.

Development of the boundary layer based on bulk Richardson number in the original COAMPS and the restricted inversion height are shown in Figure 5.8. In both methods of defining the boundary layer height, the EEP simulation produces a higher boundary layer and higher cloud layer (Figure 5.4). In Figure 5.8a, after 34 hours of simulation we find a stable layer below the cloud base when the simulated boundary layer

is apparently decoupled, most evident in q_t profile shown in Figure 5.8d at hour 35 and 45. The decoupling is also represented by the double-peak feature in the TKE profile at hour 45 (Figure 5.9e). When entrainment is explicitly represented, the boundary layer tends to be better mixed in spite of a higher boundary layer. On the other hand, the boundary height diagnosed based on liquid water and/or θ_l gradient better represents the boundary layer height. The decoupling is more evident in the q_t gradient, although a slight change in the θ_l gradient, indicative of a weak sub-cloud stable layer, is also present.

The most significant effect of the EEP is to lift the cloud base height and increase the growth rate of the boundary layer height as can be seen by comparing Figures 5.9 a) and b) to Figures 5.10 a) and b). In addition to a faster growing boundary layer, the EEP simulation results in a higher and thinner cloud with liquid water confined to approximately one or two grid levels, while in the control run the cloud layer spreads over two or more grid levels. In general, the magnitude of buoyancy flux is reduced in the EEP run compared to the control run as seen in Figures 5.9 and 5.10 f) and g), however the buoyancy flux at the flux level immediately above the grid level with cloud water is enhanced. This is mainly due to our modification to buoyancy flux at the interface to explicitly anchor the long wave radiative cooling at the interface. This compensates for the negative heat flux introduced by enhanced entrainment so that the TKE in the boundary layer is maintained at approximately the same level in both simulations.

Overall, the testing of the EEP in the SCM COAMPS seems to yield reasonable results consistent with enhanced entrainment for STCU boundary layer. Our sensitivity tests suggest that the growth of the boundary layer is rather sensitive to the vertical grid resolution, especially in our SCM testing without large scale subsidence while the sensitivity to choice of the velocity scale (or TKE) used in the model is less significant.

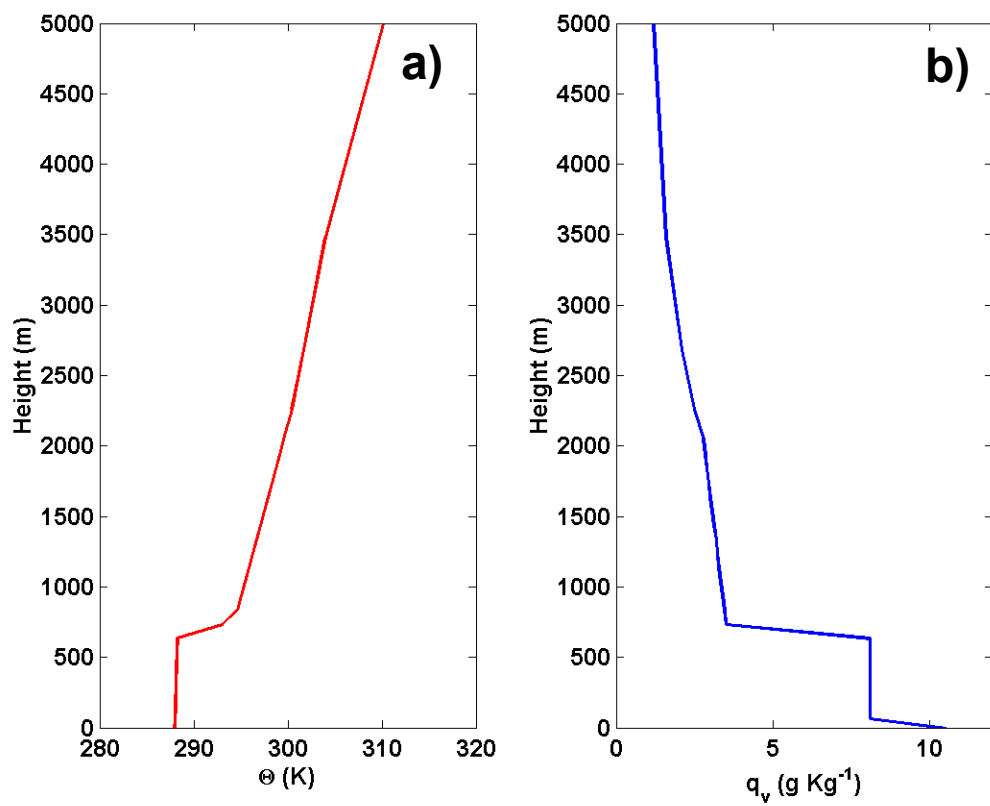


Figure 5.3. Vertical profiles of a) potential temperature and b) water vapor used to initialize the SCM COAMPS.

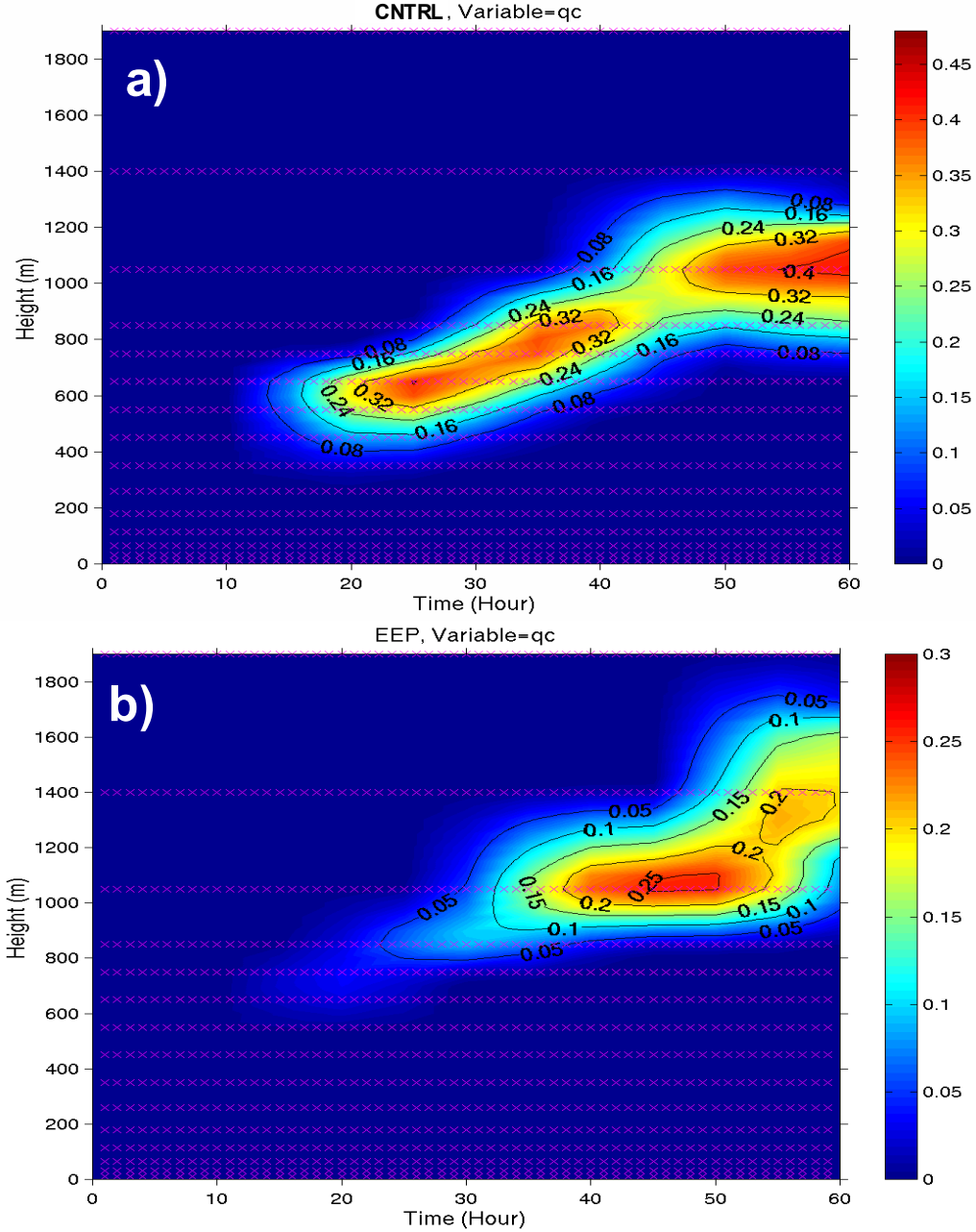


Figure 5.4. Time evolution of the vertical profiles of cloud liquid water mixing ratio ($g\ kg^{-1}$) from SCM tests for a) control run (CNTRL) and b) simulation with explicit entrainment parameterization (EEP). In both cases clouds begin to develop at hour 10, however the presence of a cloud layer triggers the EEP, which reduces the LWC for marginal cloud and delays the formation of significant cloud until 10 hours later in the EEP simulation.

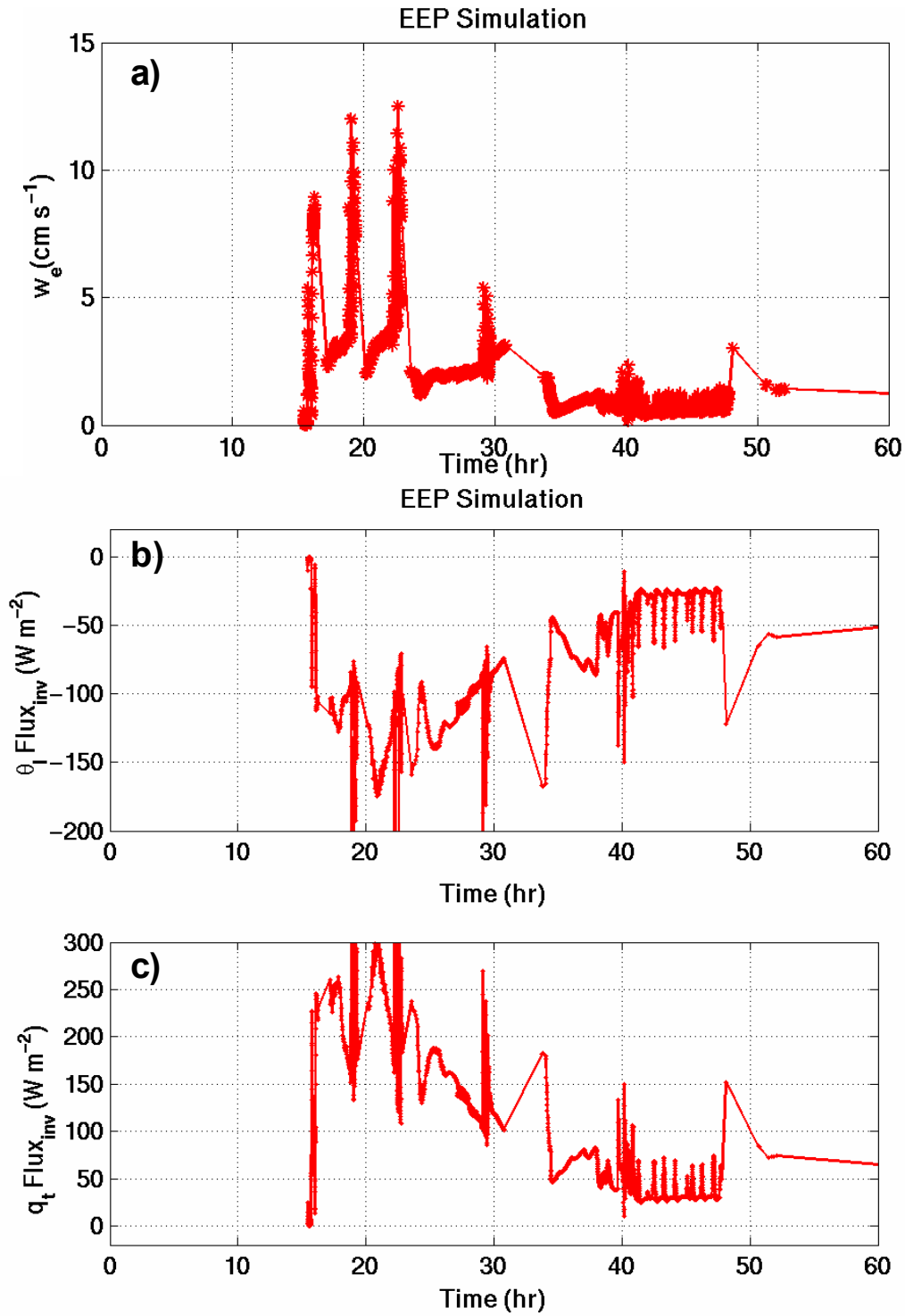


Figure 5.5. Entrainment velocity (cm s^{-1}) a) and entrainment fluxes (W m^{-2}) of liquid water potential temperature b) and total water c) from the SCM EEP simulation.

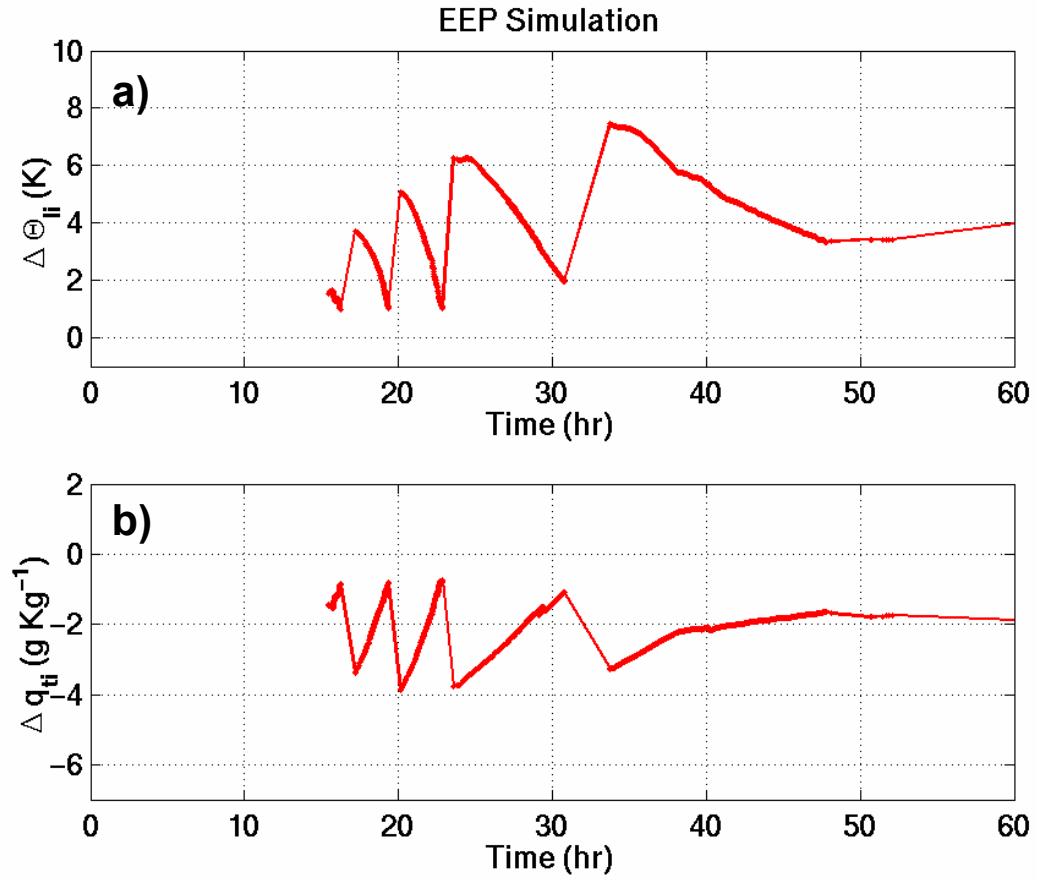


Figure 5.6. Jump condition in a) liquid potential temperature (K) and b) total water mixing ratio (g kg^{-1}) for the EEP SCM.

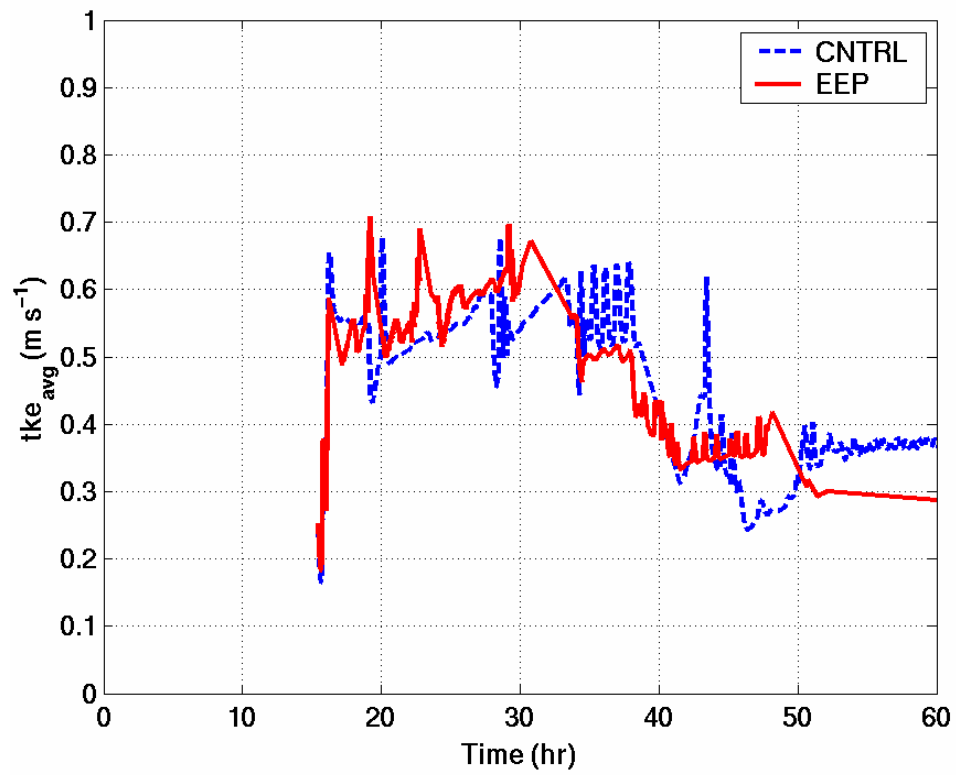


Figure 5.7. Time evolution of the vertically averaged square root of TKE (m s^{-1}).

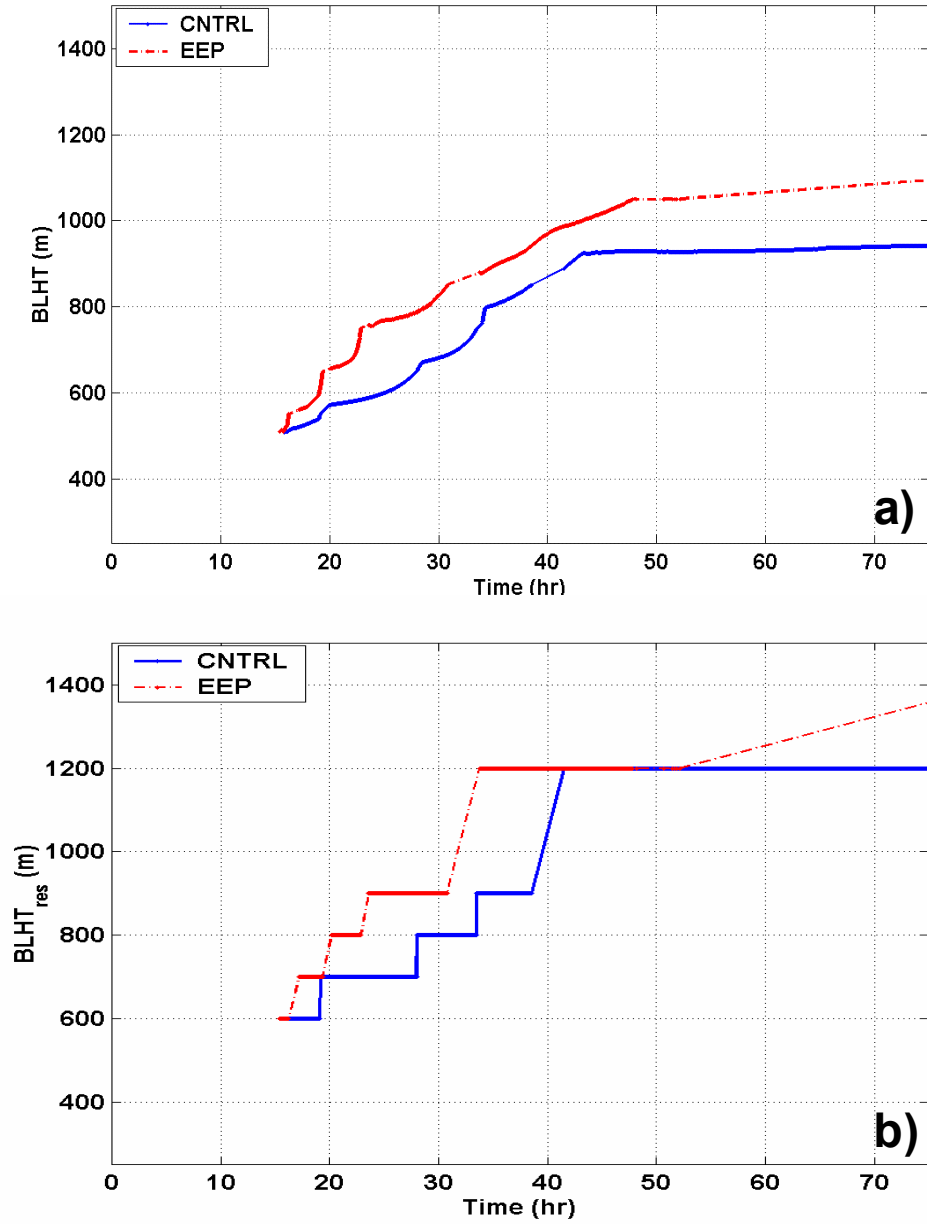


Figure 5.8. Diagnosed boundary layer height for the a) reconstructed inversion diagnosed using the Richardson number and b) boundary layer height restricted to flux level for SCM control and explicit entrainment parameterization (EEP) simulations. The Richardson number based boundary layer height is interpolated between the grid level at the inversion base and the next highest model level based on the strength of the thermodynamic gradient. The boundary layer height is only output when cloud is present and the jump condition for entrainment is met as discussed in the text, which accounts for gaps in the data just after the inversion level changes.

Control Simulation

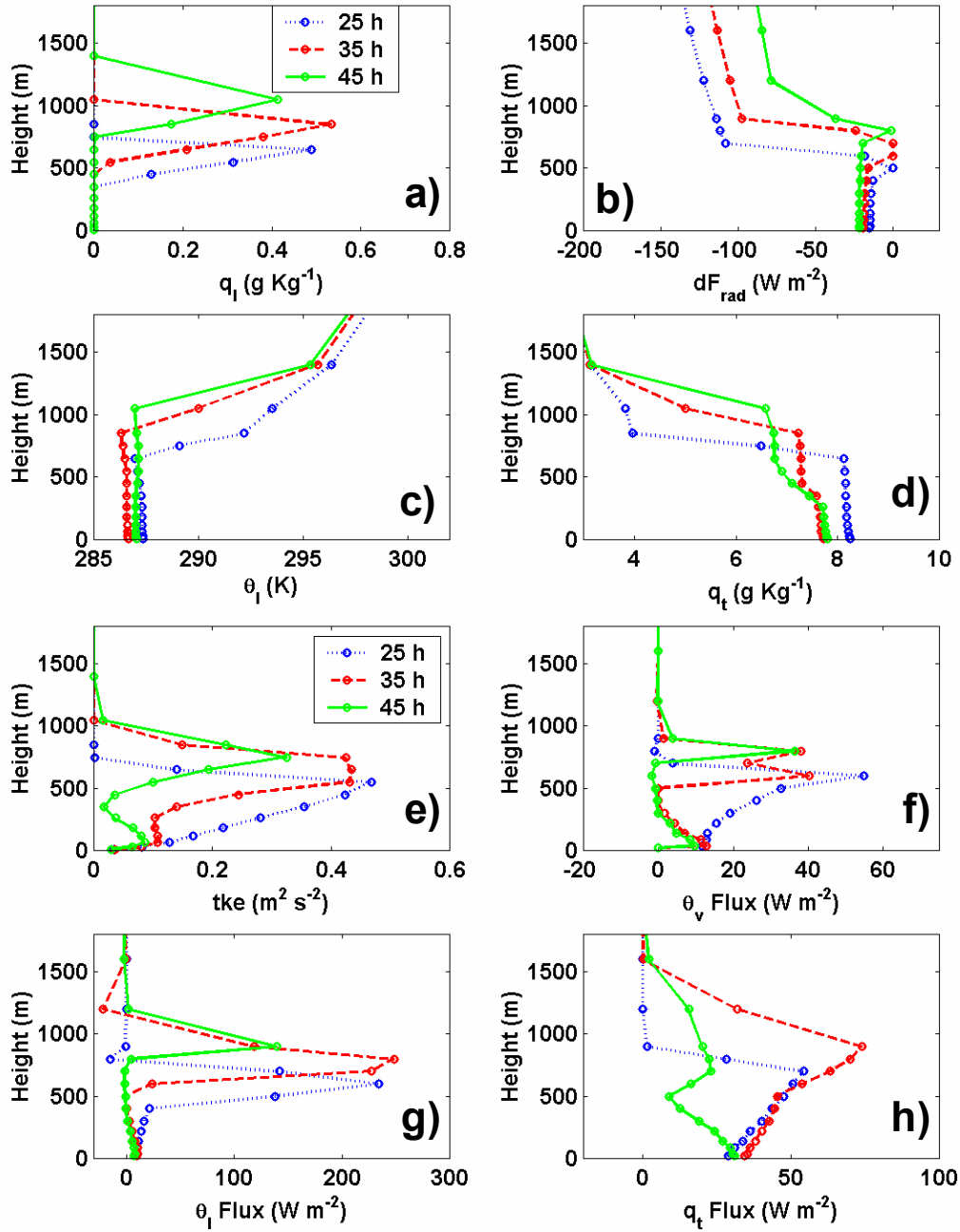


Figure 5.9. Time evolution (hours) of vertical profiles of mean and turbulence properties from the control run. (a) cloud liquid water content; (b) net radiative flux; (c) liquid water potential temperature; (d) total water specific humidity; (e) turbulence kinetic energy; (f) potential temperature flux; (g) liquid water potential temperature flux; and (h) total water flux.

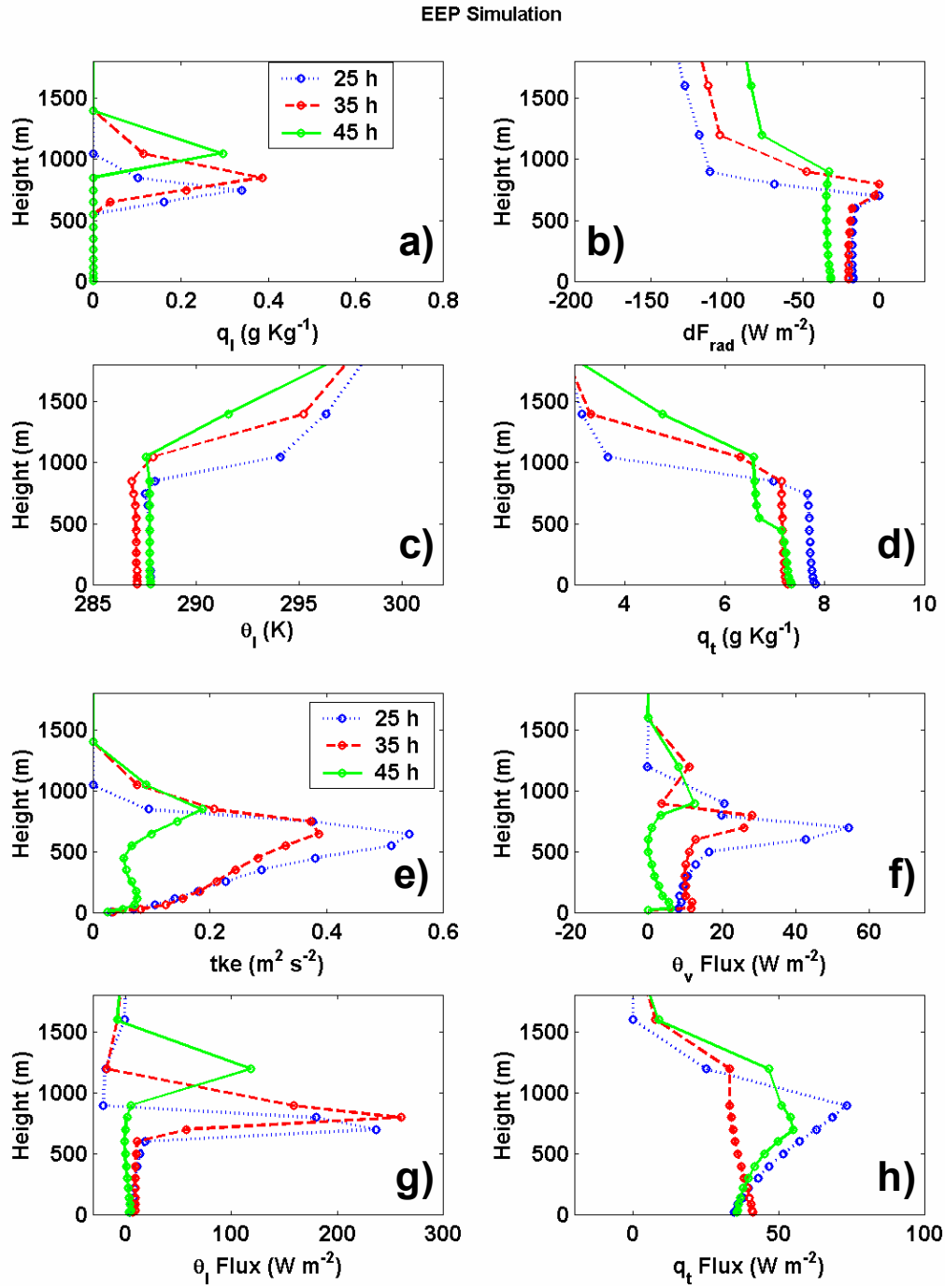


Figure 5.10. Same as in Figure 5.9., except for EEP simulation.

THIS PAGE INTENTIONALLY LEFT BLANK

VI. COAMPSTM SIMULATIONS WITH EXPLICIT ENTRAINMENT PARAMETERIZATION

Two phenomena that were frequently observed in the inner coastal zone during DECS were the onset and evolution of the MLLCJ and variations in the diurnal dissipation, reformation, structure and inland extent of the coastal stratus. As both of these are closely related to the entrainment process, model simulations of these events with and without an explicit entrainment parameterization make an interesting case study. Much of the current research (e.g. Bretherton et al. 1999, Moeng et al. 1999, Moeng 2000, Stevens et al. 2003a and 2003b) is primarily in nocturnal, buoyancy-driven marine boundary layers and stratocumulus transition while our study focuses on the daytime coastal zone structure as compared to observations.

A. CASE STUDY CONTROL RUN SIMULATIONS

In several of the flights during DECS a rapid rise in cloud base and lowering in cloud and inversion height was observed approximately 100 km from the coast. This rise in cloud base is consistent with decoupling and is supported by estimates of the lifting condensation level (LCL) based on mean parcel thermodynamic characteristics measured on the low level flight legs as reported in Kalogiros and Wang (2001). The LCL is the expected cloud base height for a parcel lifted adiabatically from the surface and is much lower than the observed cloud base, indicating that the cloud layer is separate from or decoupled from the surface fluxes. Decoupling frequently occurs when the cloud layer is heated due to solar radiation or increased entrainment of warm, dry inversion air or when the sub-cloud layer cools due to re-evaporation of drizzle, creating stable stratification. The rapid increase in cloud base may be indicative of decoupling, while the rapid lowering of cloud top and inversion height likely indicates increased subsidence. Further investigation from the simulation indicates this subsidence has a distinct mesoscale structure and is likely associated with the large-scale flow interacting with the terrain. The SCM simulations with EEP showed less tendency than the control run to decouple as

the boundary layer grew. This is likely due to increased in-cloud TKE and more turbulent transport between the cloud and sub-cloud layer in the EEP cases.

A 48-hour simulation implementing the explicit entrainment parameterization was generated for the period from 0000 UTC July 9 to 2400 UTC July 10, 1999. This period was chosen for the initial testing of EEP in the full three dimensional COAMPSTM because the synoptic conditions showed the typical summertime transition from a fully cloud covered MABL with minimal LLCJ signature on July 9 to moderately strong jet conditions and offshore clearing on July 10. Figure 6.1 depicts the evolution of the cloud fields for this period. In Figure 6.1.a) at 0000 UTC the region is characterized by clearing to the north and northwest with solid stratus to the south and offshore. Overnight the winds relax and a solid persistent stratiform cloud deck develops to the coast with nocturnal coastal and valley fog. By 0000 UTC on July 10 (late afternoon on July 9th local time) a narrow band of clearing can be seen in the satellite images in Figure 6.1.d) downstream of Cape Mendocino, Pigeon Point, and Point Sur indicative of the initial development of a coastal jet. During July 10th broad clearing occurs offshore, especially downstream of Cape Mendocino, indicative of a fully developed LLCJ while the CTBL persists in the inner coastal between Cape Mendocino and the California Bight. The cloud field on July 10th is more cumuliform or cellular in texture than on July 9th.

Figure 6.2 depicts the LWP evolution in the control run simulations. The control run produces a solid stratiform deck near the coast which matches well with the satellite observations but initiates the offshore clearing 6-12 hours too early. The boundary layer height diagnosed from the θ_1 gradient in Figure 6.3 shows higher boundary layer heights to the west and south to a maximum of 260 m with very low boundary layer heights of 155 m or less within 50 km of the coast. During the night (1200 UTC) the boundary layer is seen to lower over land, although little change is seen over water except for the development by 24 hours of a zone of lower heights offshore between 37 and 38 N, downstream of Cape Mendocino. This correlates well with both the surface wind speed and the wind speed at the inversion depicted in Figures 6.4 and 6.5. Although the timing is about 12 hours too early, the clearing and increased winds in the simulation seem to correspond well with satellite data depicting cloud dissipation and ship and buoy

observations depicting an increase in surface winds from 15 to 20 knots. Despite the differences in the synoptic scale offshore cloud field between the observations and the control run, our primary focus is in the coastal zone and the mesoscale structure of the boundary layer. In this region the simulation does reasonably well and can be used to compare with the observations and the results of explicitly parameterizing entrainment. It is expected that the differences between the control and EEP simulations will primarily be in the fine scale structure of the CTBL, which will be examined in the next section.

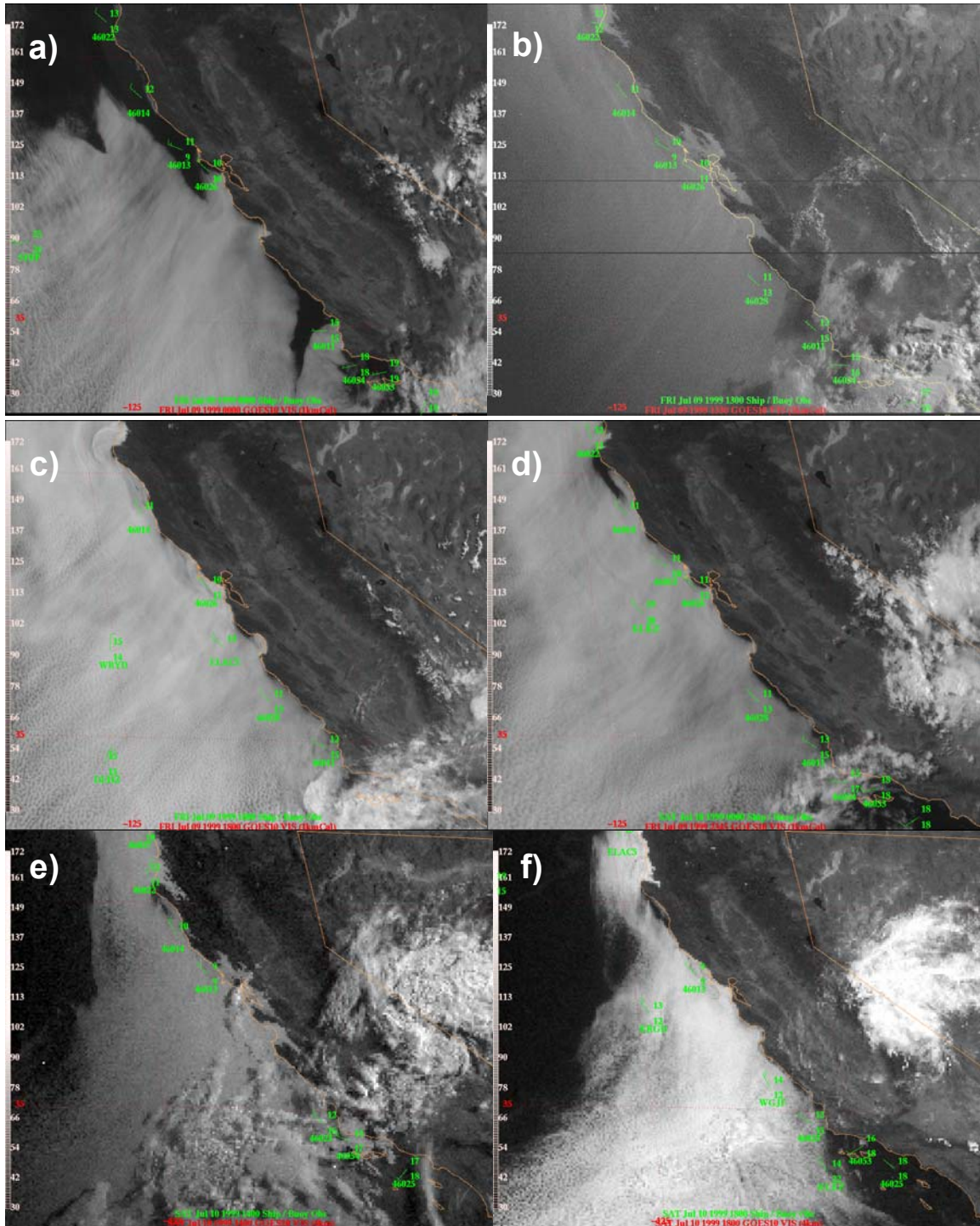


Figure 6.1: Visual satellite image and buoy observations for a) 0000, b) 1300, c) 1800, and d) 2400 UTC July 9, 1999 and e) 1400 and f) 1800 UTC July 10, 1999 depicting solid cloud cover and light surface winds transitioning to clearing offshore and stronger surface winds.

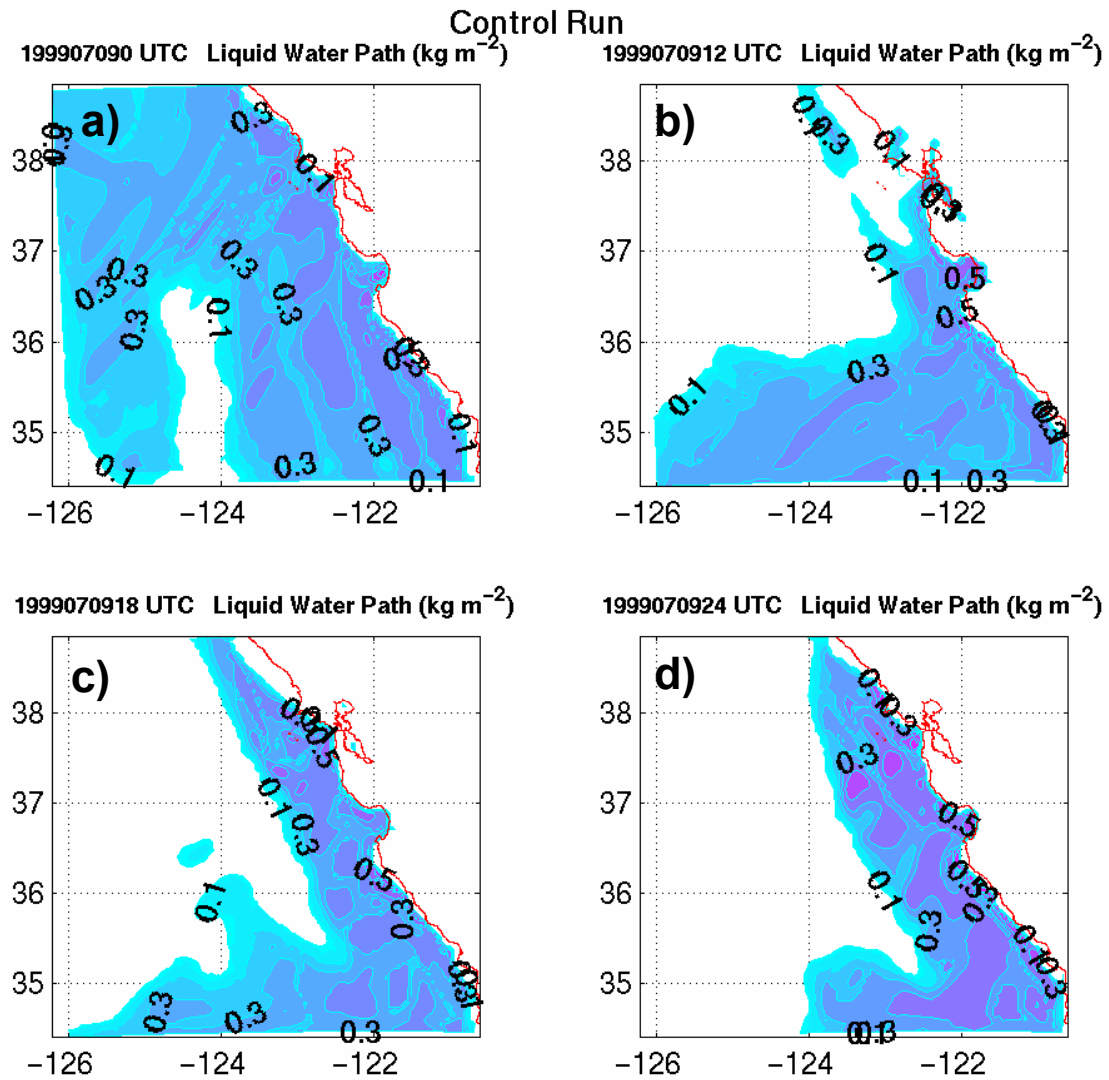


Figure 6.2. Control run forecast LWP (kg m^{-2}) for a) 0000, b) 1200, c) 1800, and d) 2400 UTC July 9, 1999 from an initial analysis at 0000 UTC depicting solid cloud cover in the inner coastal region with clearing propagating southward west of 124 N.

Control Run

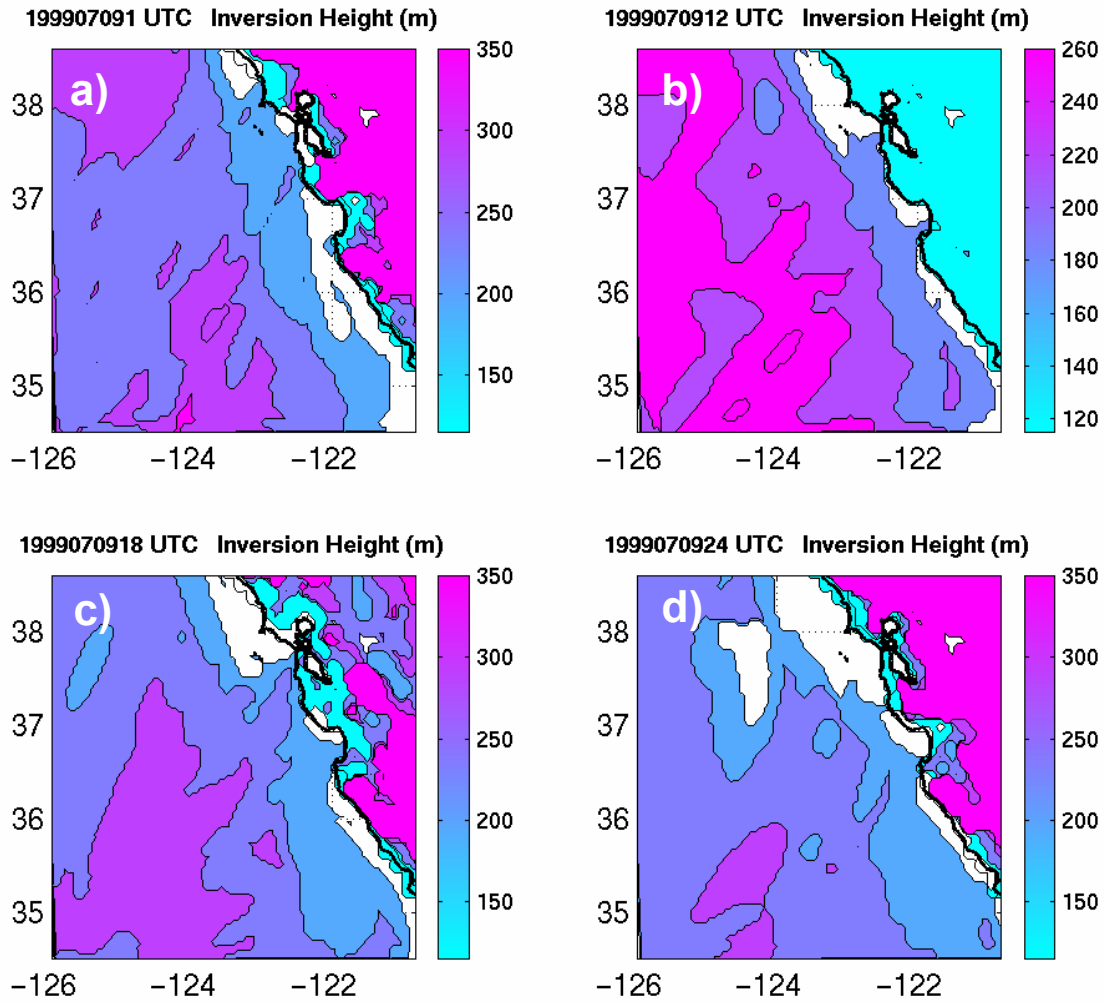
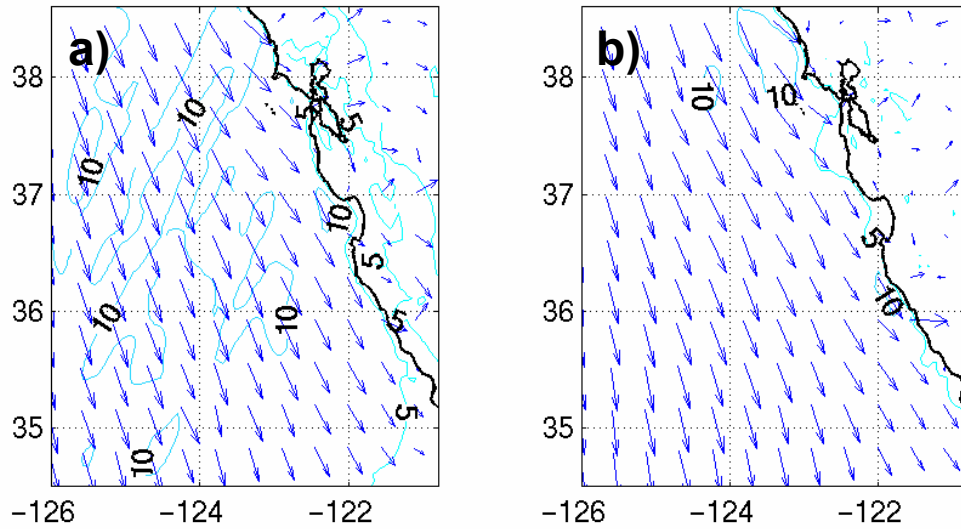


Figure 6.3. Control run inversion height (m) based on θ_1 gradient for a) 0001, b) 1200, c) 1800, and d) 2400 UTC July 9, 1999 depicting higher boundary layer heights offshore and nocturnal lowering over land. The boundary layer height diagnostic based on virtual potential temperature gradient is not produced at analysis time so the 0001 UTC field is substituted.

Control Run

199907091 UTC Windspeed at the Surface (m s^{-1}) 1999070912 UTC Windspeed at the Surface (m s^{-1})



1999070918 UTC Windspeed at the Surface (m s^{-1}) 1999070924 UTC Windspeed at the Surface (m s^{-1})

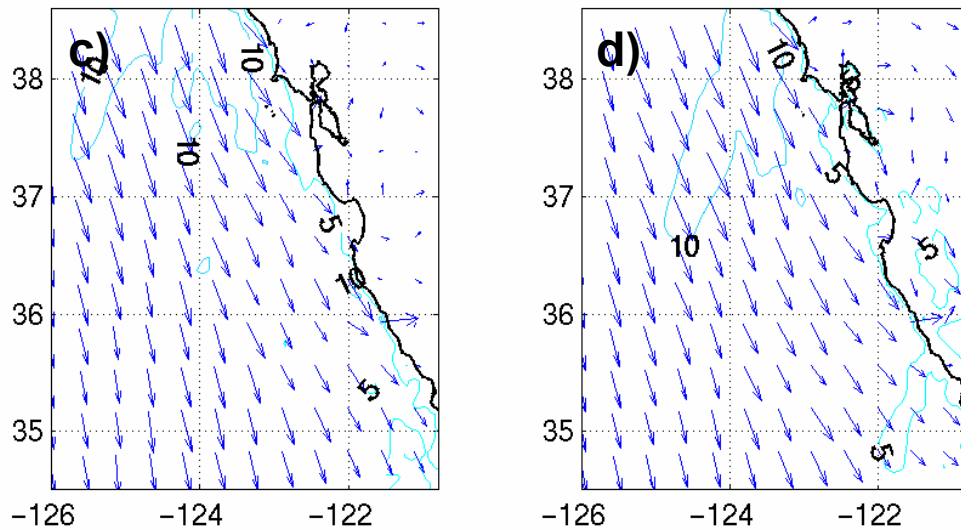
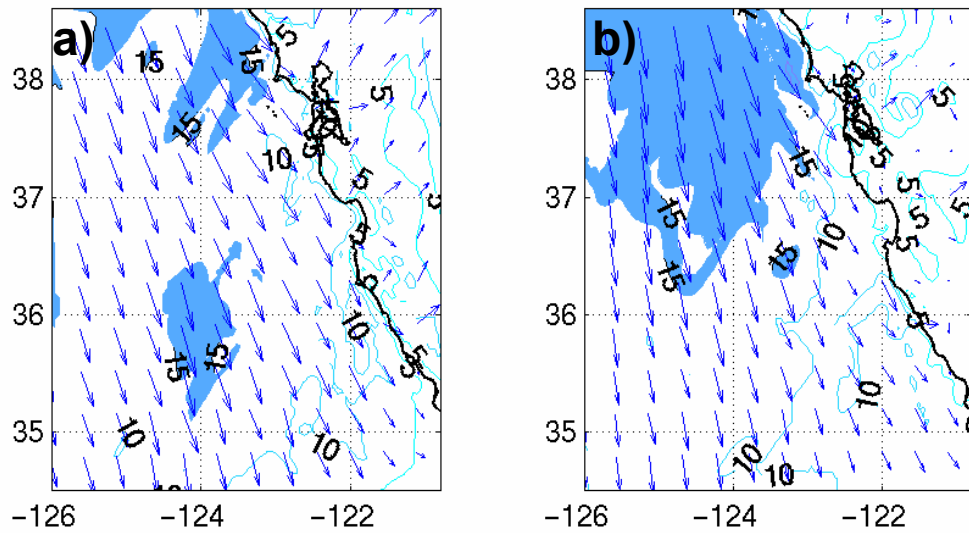


Figure 6.4. Control run surface wind speed (m s^{-1}) and direction (arrows) for a) 0000, b) 1200, c) 1800, and d) 2400 UTC July 9, 1999 depicting generally light winds along the coast increasing offshore.

Control Run

199907091 UTC Windspeed at Inversion (m s^{-1}) 1999070912 UTC Windspeed at Inversion (m s^{-1})



1999070918 UTC Windspeed at Inversion (m s^{-1}) 1999070924 UTC Windspeed at Inversion (m s^{-1})

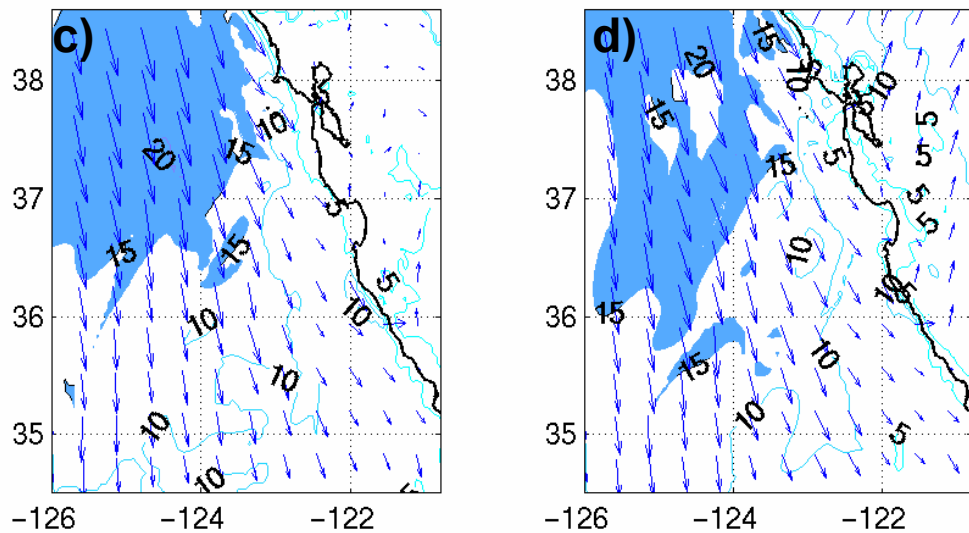


Figure 6.5. Control run windspeed (m s^{-1}) and direction (arrows) at the inversion height for a) 0000, b) 1200, c) 1800, and d) 2400 UTC July 9, 1999 depicting generally development of a coastal low level jet offshore.

B. CASE STUDY SIMULATIONS USING AN EXPLICIT ENTRAINMENT PARAMETERIZATION

1. Effects Of Explicit Entrainment On Simulating The Coastal Boundary Layer

Although the effect on total boundary layer growth was much smaller in the 3-D model than in the SCM, there was some modest improvement in the mean structure as compared to the observations. The LWP evolution in Figure 6.6 shows a similar trend, horizontal structure, and cloud edge for the EEP as in the control run, although absolute amounts are about 25% or 0.05 to 0.15 kg m⁻² lower except very close to the coast where both simulations show values in the 0.4 to 0.5 range. The wind speed and direction in Figure 6.7 and Figure 6.8 for the EEP simulations showed no noticeable difference from the control run, which is not unexpected as the current EEP formulation may not completely represent momentum mixing.

Figure 6.9 depicts the time evolution of the boundary layer in an east-west cross-section from Monterey Bay, approximately corresponding to the aircraft flight track. Although the EEP cloud top is not noticeably higher, the LWC is reduced and the cloud base is elevated, which better matches the observations. The obvious exception to this is within 25 km of the coast, where both simulations saturate the boundary layer to the surface and produce fog. This is the region of highest complexity and largest variance in the differences between and observed inversion heights and warrants further study.

Figure 6.10 depicts the difference in the height of the inversion base based on the liquid potential temperature gradient for the control and EEP simulations. In general the boundary layer is 50-100 m higher in the EEP simulations, especially between 122 and 124 degrees west, with a less noticeable effect very close to the coast where the boundary layer is lowest and SSTs are coldest. The exception to this is very close to the coast in the region of the MLLCJ, where the EEP actually produces lower boundary layer heights. Indications are that the current EEP underestimates entrainment in shear-dominant conditions. The role of shear in entrainment efficiency across the boundary layer top has been minimally explored in the literature and especially warrants further study.

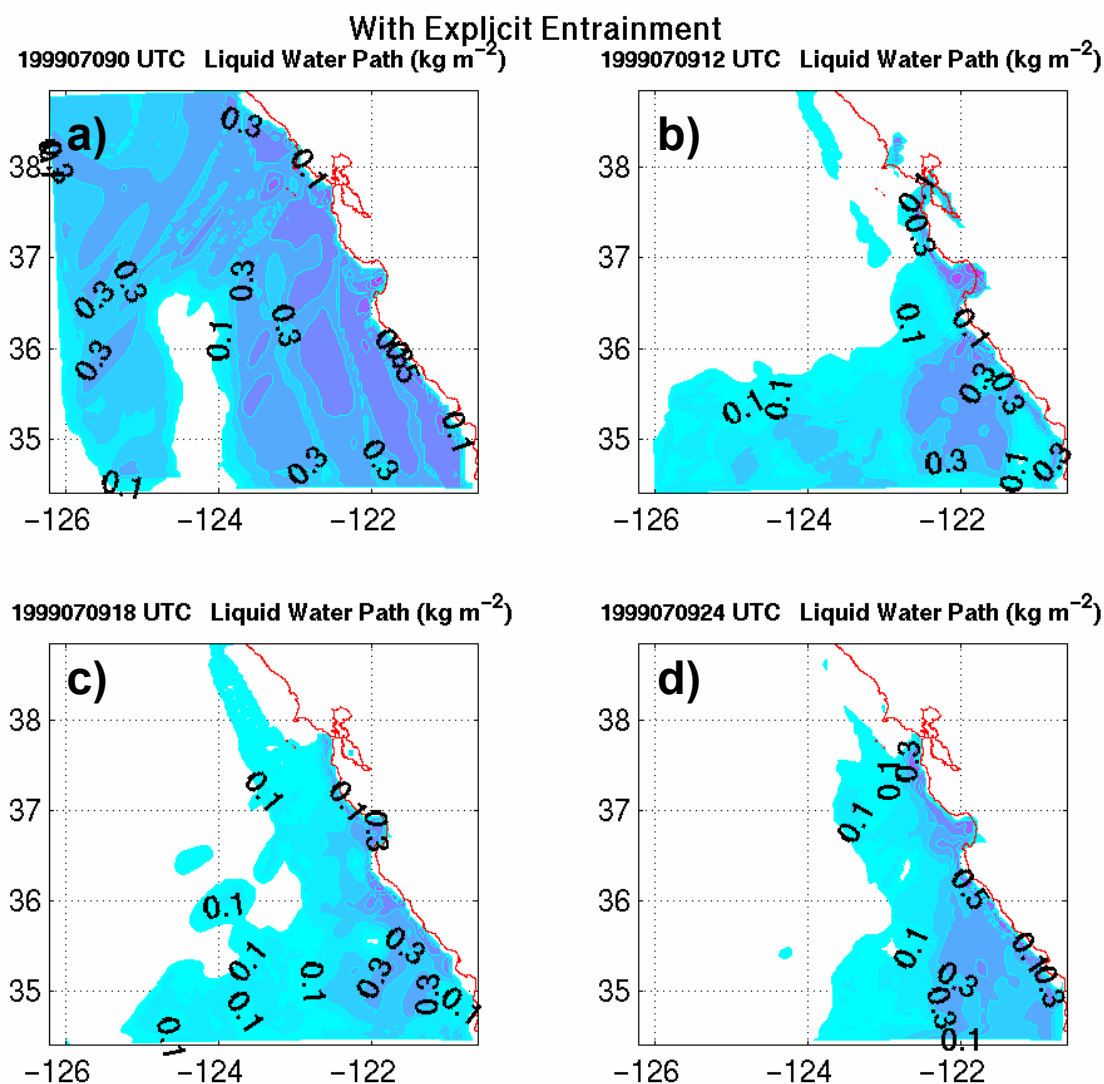
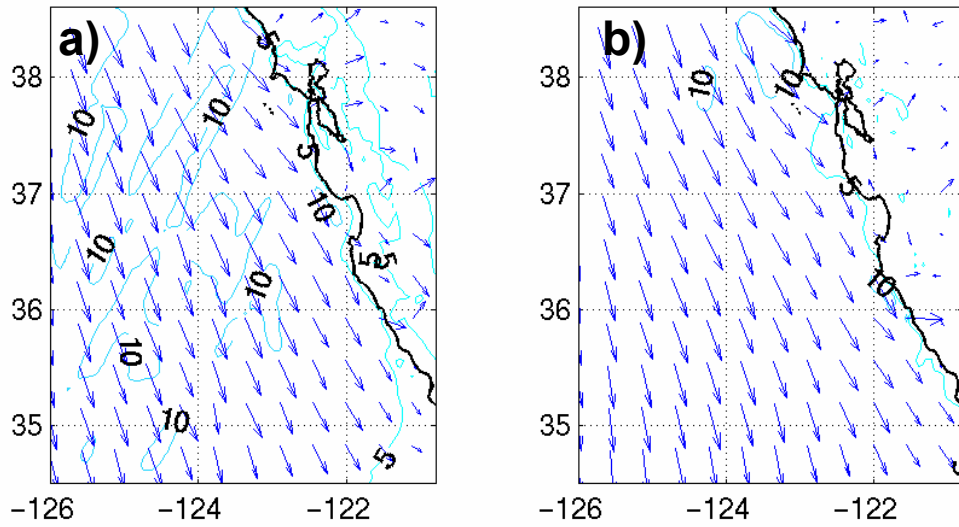


Figure 6.6. EEP simulation forecast LWP (kg m^{-2}) for a) 0000, b) 1200, c) 1800, and d) 2400 UTC July 9, 1999 depicting solid cloud cover in the inner coastal region with clearing propagating southward west of 124 N. Note cloud edge is similar to the control run but the LWP values are generally lower.

With Explicit Entrainment

1999070912 UTC Windspeed at the Surface (m s^{-1}) 1999070912 UTC Windspeed at the Surface (m s^{-1})



1999070918 UTC Windspeed at the Surface (m s^{-1}) 1999070924 UTC Windspeed at the Surface (m s^{-1})

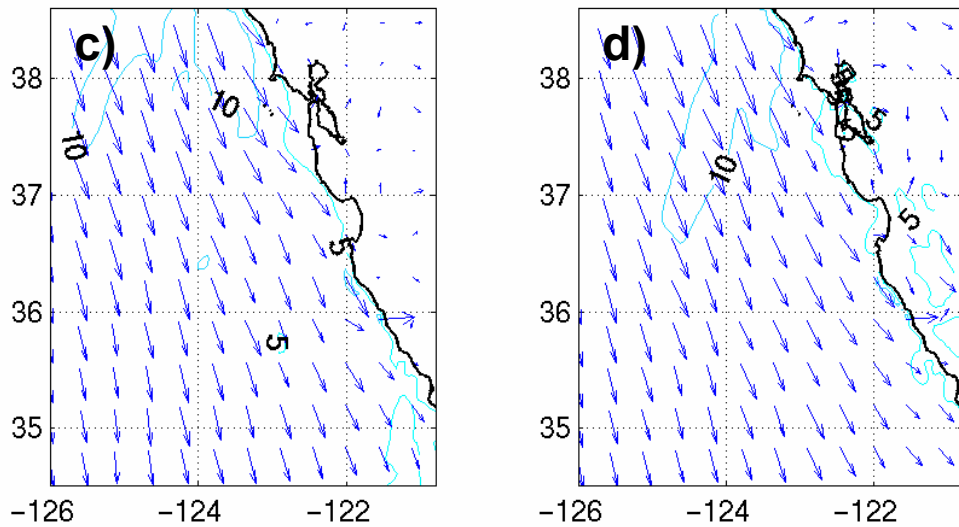
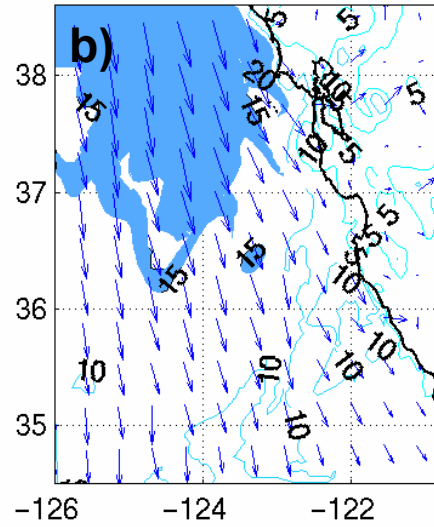
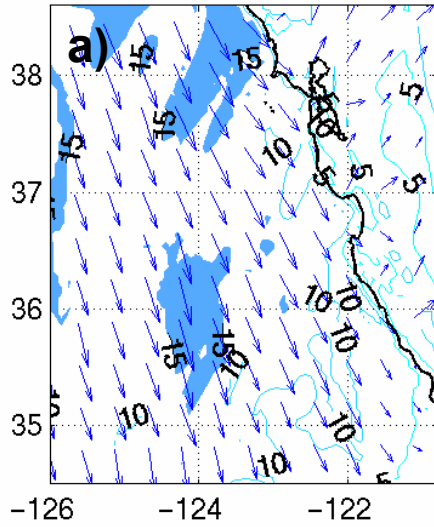


Figure 6.7. EEP simulation surface wind speed (m s^{-1}) and direction (arrows) for a) 0000, b) 1200, c) 1800, and d) 2400 UTC July 9, 1999 depicting generally light winds along the coast increasing offshore.

With Explicit Entrainment

1999070912 UTC Windspeed at the Inversion (m s^{-1})



1999070918 UTC Windspeed at the Inversion (m s^{-1})

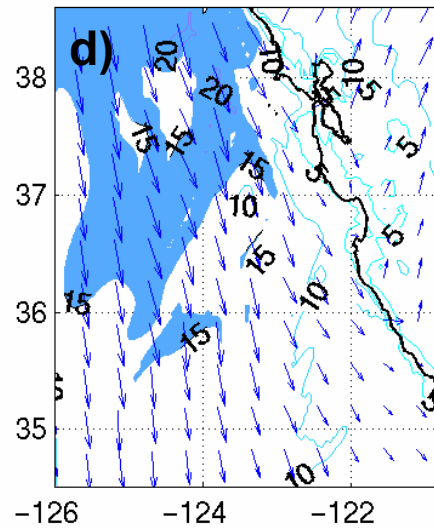
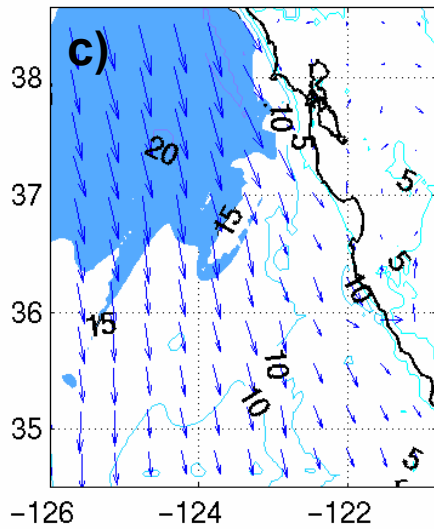


Figure 6.8. EEP simulation windspeed (m s^{-1}) and direction (arrows) at the inversion height for a) 0000, b) 1200, c) 1800, and d) 2400 UTC July 9, 1999 depicting the development of a coastal low level jet offshore.

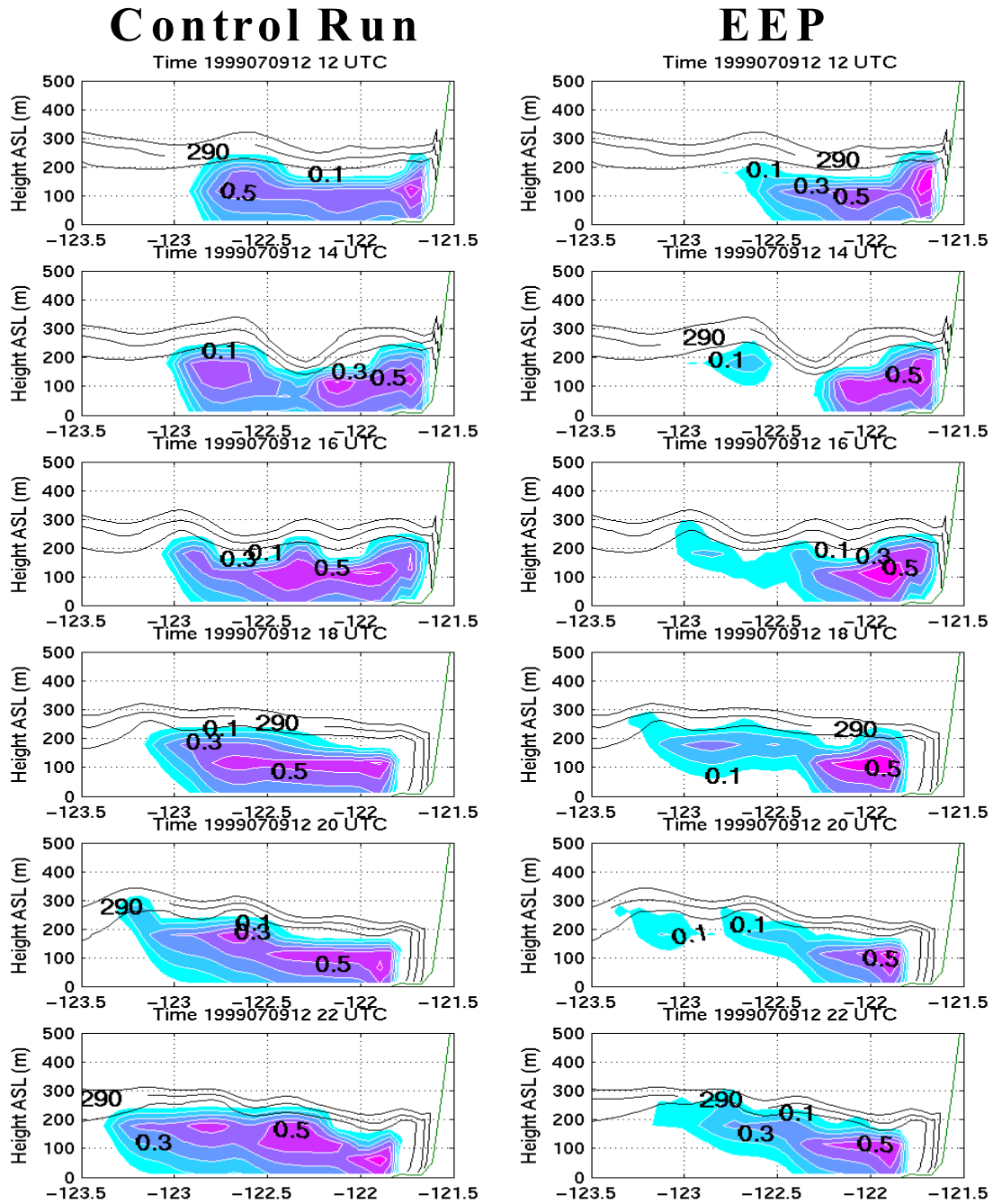


Figure 6.9: Time series contours of LWC (g kg^{-1}) (shaded) and θ_l (solid lines) for the control and EEP simulation along an east-west cross-section from Monterey Bay. Note the reduced LWC and higher cloud base in the EEP simulations.

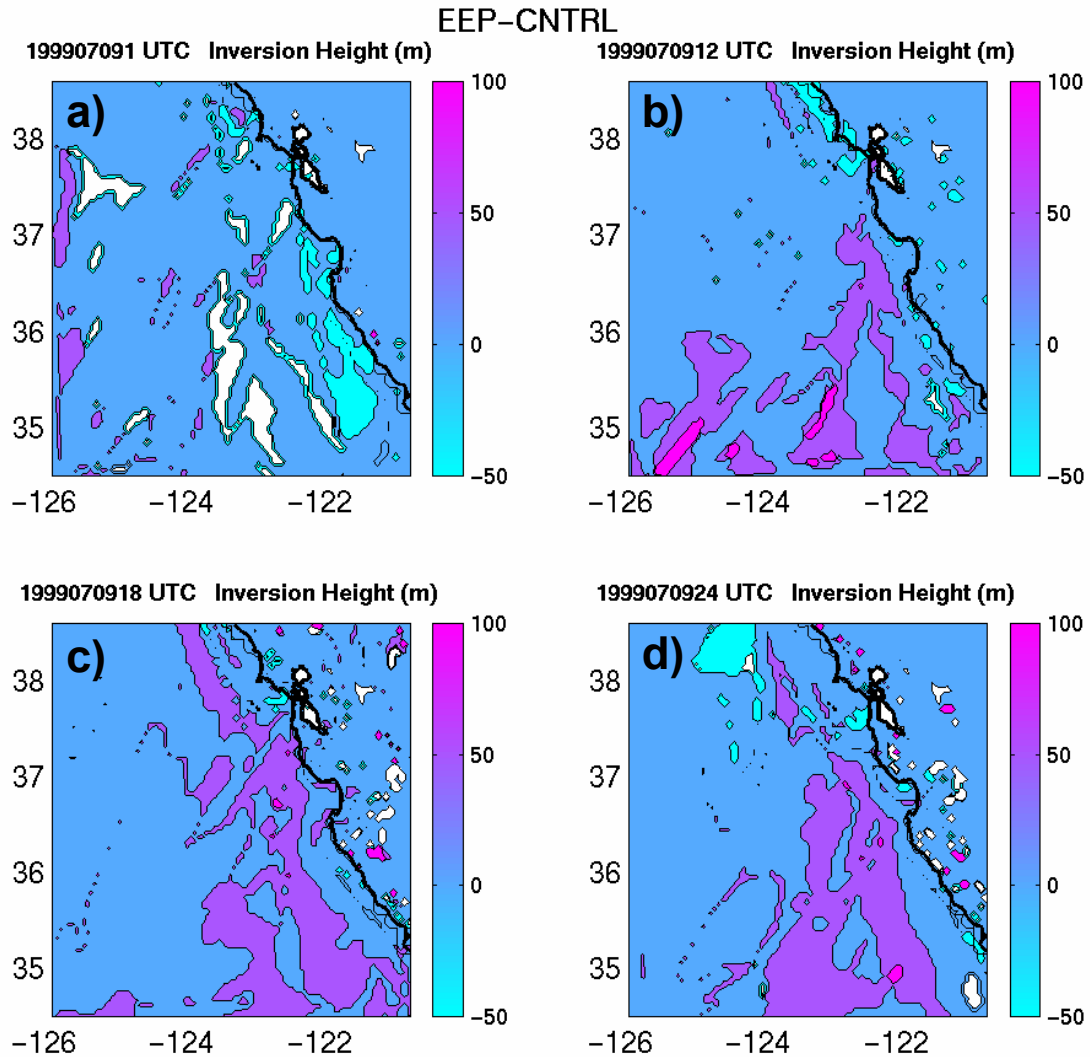


Figure 6.10. Difference between the diagnosed inversion height (m) in the control run and EEP simulation for a) 0001, b) 1200, c) 1800, and d) 2400 UTC July 9, 1999 from an initialization at 0000 UTC. Note the lower inversion height near the coast for the EEP during the early part of the simulation and the generally higher heights later on in the forecast.

2. Changes in the Resulting Turbulent Flux Profiles and Boundary Layer Structure

In order to better analyze the detailed effects of EEP as compared to the idealized SCM results, individual profiles were generated for the control and EEP simulations corresponding to the observed aircraft soundings. Figure 6.11 and 6.12 are two representative profiles of the mean boundary layer structure and the turbulent fluxes. The general wind and thermodynamic structure of the boundary layer was not seen to change nearly as much in the three dimensional model with EEP as in the SCM, possibly due to the effects of horizontal advection between cloudy and clear grid points. This is not unexpected as changes to the turbulence parameterization generally have the greatest effect in the fine scale and on long term equilibrium or climate scale. The mean boundary layer structure and mesoscale-to-synoptic variability respond much more strongly to the synoptic forcing and changes to the turbulence and in-cloud turbulent fluxes in a strongly subsiding environment are damped. In the three dimensional model, the EEP simulation depicted the same general trends and direction as in the SCM tests in that the cloud liquid water was reduced, the inversion was modestly higher by 1-2 grid levels (~100 m), and the TKE and turbulent fluxes were greater at cloud top and more negative just above cloud top. A sharpening of the potential temperature gradient at cloud top was also observed which was less noticeable in the SCM. As discussed in Paluch and Lenschow (1991), this sharpening of the inversion structure is characteristic of the STBL as a result of in-cloud TKE primarily generated by cloud-top radiative cooling responding to mean subsidence above the cloud. The SCM tests did not account for the presence of large scale subsidence acting against the growth of the turbulent boundary layer.

The TKE near the surface was similar or slightly reduced in the EEP cases but was larger at cloud top. The buoyancy flux was also larger in the cloud layer and larger in the negative sense above the cloud which is consistent with the SCM tests.

1999070917 17.23 Sounding 11

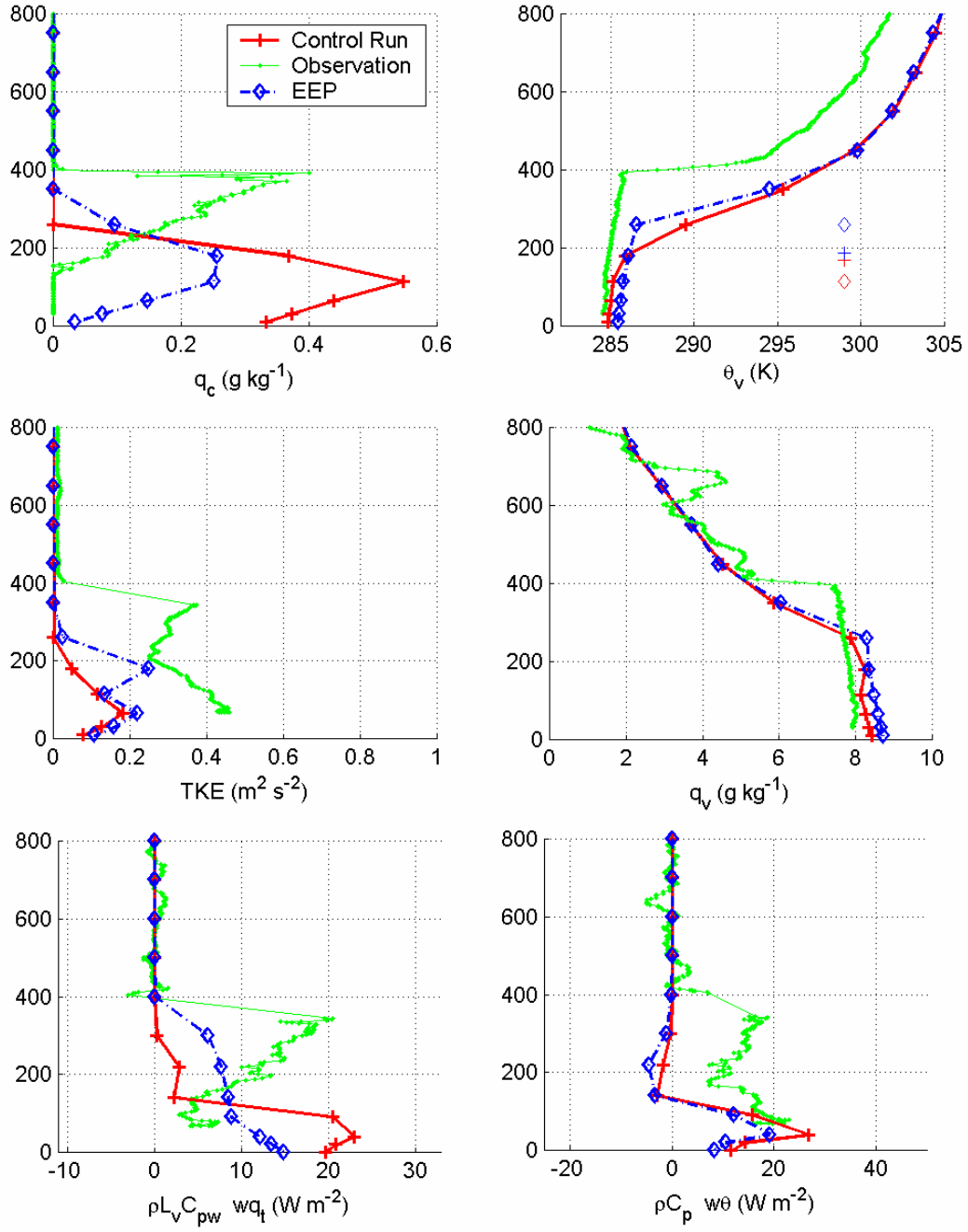


Figure 6.11. Model vertical profiles (diamonds) for control run (solid line) and EEP (dashed line) and observed sounding leg (dark thick line) for thermodynamic and turbulence structure in the coastal boundary layer.

1999070918 17.86 Sounding 15

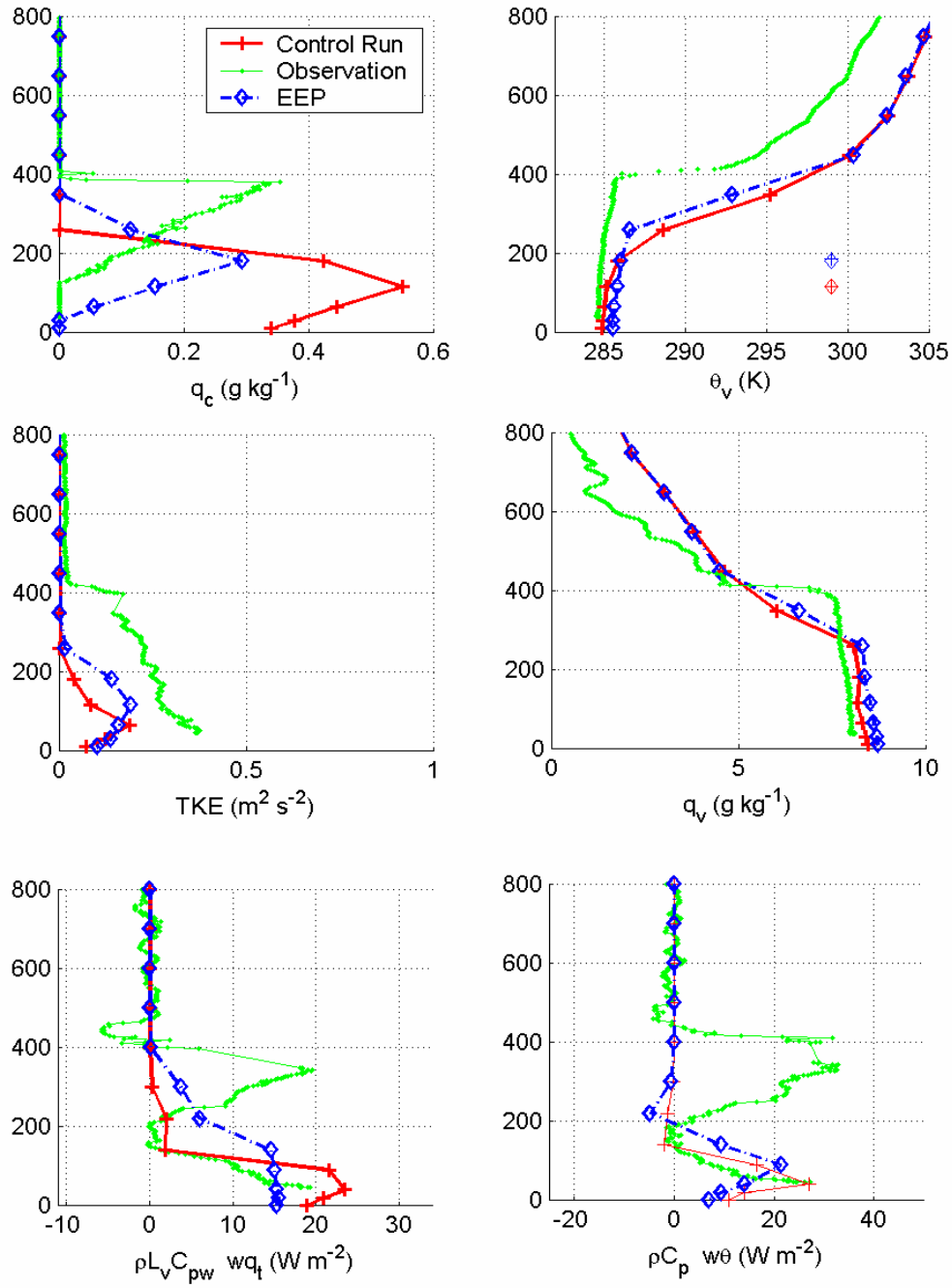


Figure 6.12. As in Figure 6.11 except for another location.

THIS PAGE INTENTIONALLY LEFT BLANK

VII. SUMMARY, CONCLUSIONS, AND RECOMMENDATIONS

A. SUMMARY AND CONCLUSIONS

This thesis research focuses on improving the understanding and representation of physical processes in the marine stratocumulus-topped boundary layer and their interaction with the coastal flow field. Careful analysis of the observed summertime cloud-topped boundary layer structure from the DECS field study supported our general conceptual model of the coastal zone including such features as the increase in boundary layer height southward and away from the coast and a sharp discontinuity in the temperature and moisture fields at cloud top. A general synoptic pattern was observed of uniform fog and stratus with a diurnal signature over land to within a few kilometers of the coast, followed by increasing low level winds and clearing over a 2-3 day period. It was observed that increases in the coast-parallel wind speed at the boundary layer top were coincident with a distinct mesoscale variability in the horizontal structure and diurnal dissipation of the cloud, especially within 100 km of the coast. This has been attributed to flow interaction with the terrain creating velocity minima, compression bulges, higher inversion heights and more persistent cloudiness upstream of points and expansion fans, clearing, and accelerations downstream of points. In general, the observations support this model, however it was noted that in the cloud topped boundary layer, the velocity maximum was frequently below the inversion, or the boundary layer velocities were nearly uniform with height to a minimum above the inversion. This is somewhat different than the expected structure of the low level coastal jet and warrants further study. In the clear boundary layer, the structure was more classic, with a well defined maximum in velocity at or just above the inversion height.

In the control run simulations COAMPSTM was used to simulate the atmospheric structure for the entire DECS period in order to better understand the observed patterns and assess the forecast model's ability to represent them. The model winds, cloud fields and boundary layer structure matched the observations quite well in the synoptic and diurnal evolution and horizontal variability, with the exception of some consistent biases in the inversion height and cloud liquid water content. More detailed analyses revealed

that the cloud-topped marine boundary layer height in COAMPSTM is, on average, underestimated by about 200 m and the liquid water content is over-estimated by about 25%, or about 0.15 g kg⁻¹. Furthermore, the model matched the observations in the clear marine boundary layer much more closely, indicating that the bias in the control run may be related to particular characteristics of the CTBL. These biases were not found to correlate well with distance from the coast, synoptic variability, or time of day, although the difference between the observations and the model was much higher with more spread close to the coast. This is expected as flow interaction with the terrain and land-sea interactions make this region particularly complex. The underestimate of the cloud top and base has greater operational impact near the coast because the boundary layer is in general rather shallow, resulting in COAMPSTM producing fog rather than the observed low stratus in the inner coastal zone.

The correlation with cloudy conditions implies that the bias is likely due to misrepresentation of cloud-related processes. The high LWC and low inversion top is consistent with under-representation of entrainment fluxes at cloud top. Therefore we implemented an explicit entrainment parameterization scheme to test this hypothesis. Following the work of Grenier and Bretherton (2001) we developed a framework within COAMPSTM to diagnose the entrainment velocity across the inversion, calculate the entrainment fluxes and represent the entrainment effects explicitly in the forecast model. We tested this framework in the convective stratocumulus-topped marine boundary layer in the single column model and found that, in the absence of subsidence, the explicit entrainment fluxes caused the boundary layer to grow faster than in the control run, the boundary layer was better mixed, the potential temperature was higher, the cloud layer was thinner and the liquid water and total water content was lower. These trends were consistent with explicit entrainment being more efficient than the implicit method used in the parent turbulence closure model at entraining warm, dry air into the cloud layer from above the inversion.

Some technical issues were examined in the SCM formulation and testing. These included several approaches for specifying the inversion height in a robust and consistent way. This is especially critical when the boundary layer is evolving rapidly and the

inversion strength and height is changing between discrete grid levels because inconsistent treatment results in incorrect entrainment flux and model noise. The most robust method was found to be direct diagnosis of the cloud top, which is simple to implement but restricts further study of entrainment with this EEP framework to the CTBL. Another critical area is the specification of the appropriate value for TKE in the explicit entrainment parameterization. TKE at cloud top, one level below cloud top and the layer averaged TKE were tested. Another possibility that was not explored is to use other estimates of the turbulent forcing such as the convective velocity scale (w^* , Stull 1988). Other technical issues that were addressed include the introduction of the eddy diffusivity mixing length consistently into the TKE prognostic equation and the turbulent mixing subroutines, specification of the thermodynamic structure of the sub-grid scale ambiguous layer that the inversion lies within, and accounting for key sub-grid scale processes such as evaporative enhancement of the TKE generation by mixing between cloudy and clear parcels and radiative flux divergence across a discontinuous boundary.

Once a reasonably stable and consistent scheme was developed for the SCM, a full three dimensional case study was run to explore the impact of the EEP with realistic forcing and horizontal variability. The explicit parameterization was found to produce trends qualitatively similar to the SCM in that the inversion layer was cooled and moistened, the inversion sharpened, and the cloud liquid water was reduced. The surface buoyancy and total water fluxes were reduced somewhat but the cloud-top TKE was increased. In some cases, the in-cloud total water and buoyancy flux was seen to increase and the negative buoyancy flux above cloud top became stronger. This resulted in a profile that better matched the observations. The actual cloud top was highly variable and increased moderately in some cases and decreased in others. Overall, the net effect was to lift the inversion by about one grid level, or 50-100 meters and reduce the LWC so that the surface layer was no longer saturated. The observations indicated that the cloud deck was frequently 100-200 meters thick, which is difficult to accurately represent when the model vertical grid resolution is the same magnitude.

B. RECOMMENDATIONS FOR FURTHER STUDY

This thesis work has established a basic framework for explicit entrainment implemented into COAMPSTM. Based on this framework, various formulations can be evaluated and observational data can be used to evaluate the appropriateness of the associated free parameters and constants originally derived from other field studies or LES data. As discussed in Chapter II, several researchers have developed schemes for calculating the entrainment velocity that are more sophisticated than the basic local closure implemented here that could easily be tested in the current framework. While most of the current entrainment research focuses on buoyancy effects from radiative and evaporative forcing, a complete parameterization should also include shear effects, for which it is expected that the MLLCJ interaction with the CTBL top and the frequently observed indicative cloud signature will make an excellent case study. The DECS dataset includes cloud radar, rawinsonde, ceilometer, RASS and profiler data as well as surface mesonet and aircraft data, which should facilitate the study of CTBL diurnal evolution as the high data rate aircraft sounding data available in many field studies can be augmented with excellent temporal coverage in the vertical at a fixed point. Furthermore, many of the efforts such as Grenier and Bretherton (2001) and Lenderink and Holtslag (2000) that combine explicit entrainment with a TCM were tested using single column models. As reported in Bretherton et al. (2004) and McCaa and Bretherton (2004), other researchers have examined the effects of explicit entrainment and shallow convective parameterizations on the climate scale mean structure of the summertime Eastern Pacific marine CTBL, however the mesoscale variability and vertical structure in the inner coastal is still relatively under studied. Implementing this approach in a three dimensional model with full physics will allow us to better understand the mesoscale effects of the three dimensional flow in the inner coastal zone. The resulting parameterization should be tested across a broad spectrum of regimes besides the summertime coastal marine CTBL before implementation in operational COAMPSTM.

LIST OF REFERENCES

- Albrecht, B. A., D. A. Randall, and S. Nicholls, 1988: Observations of marine stratocumulus during FIRE. *Bull. Amer. Met. Soc.*, **69**, 618-626.
- _____, 1989: Aerosols, cloud microphysics and fractional cloudiness. *Science*, **245**, 1227-1230.
- _____, C. S. Bretherton, D. Johnson, W. H. Schubert, and A. S. Frisch, 1995: The Atlantic Stratocumulus Transition Experiment -- ASTEX. *Bull. Amer. Meteor. Soc.*, **76** (6), 889-904.
- Atkinson, B. W. and J. W. Zhang, 1996: Mesoscale Shallow Convection in the Atmosphere. *Rev. Geophys.*, **34**, 403-431.
- Banta, R. M., L. D. Olivier, and D. H. Levinson, 1993: Evolution of the Monterey Bay sea-breeze layer as observed by pulsed Doppler lidar. *J. Atmos. Sci.* **50** (24), 3959-3982.
- Beardsley R. C., C. E. Dorman, C. A. Friehe, L. K. Rosenfeld, and C. D. Winant, 1987: Local atmospheric forcing during the Coastal Ocean Dynamics Experiment 1. A description of the marine boundary-layer and atmospheric conditions over a Northern California upwelling region. *J. Geophys. Res. – Oceans*, **92** (C2), 1467-1488.
- Bretherton C. S., M. K. Macvean, P. Bechtold, et al., 1999: An intercomparison of radiatively driven entrainment and turbulence in a smoke cloud, as simulated by different numerical models. *Q. J. Roy. Meteor. Soc.*, **125 B** (554), 391-423.
- _____, J. R. McCaa, and H. Grenier, 2004: A new parameterization for shallow cumulus convection and its application to marine subtropical cloud-topped boundary layers. Part I: Description and 1D results. *Mon. Wea. Rev.*, **132**, 864-882.
- Brost, R. A., D. H. Lenschow, and J. C. Wyngaard, 1982a: Marine stratocumulus layers. Part I: Mean conditions. *J. Atmos. Sci.* **39**, 800-817.
- _____, J. C. Wyngaard and D. H. Lenschow, 1982b: Marine stratocumulus layers. Part II: Turbulence budgets. *J. Atmos. Sci.* **39**, 818-836.
- Burk S. D. and W. T. Thompson, 1996: The summertime low-level jet and marine boundary layer structure along the California coast. *Mon. Weather. Rev.*, **124** (4), 668-686.
- Burk S. D., Haack T., Rogers L. T., Wagner L. J., 2003: Island wake dynamics and wake influence on the evaporation duct and radar propagation. *J. Appl. Meteorol.* **42**, 349-367.

- Chen, S. and Coauthors, 2003: COAMPSTM Version 3 Model Description – General Theory and Equations. NRL Publication NRL/PU/7500—03-448, May 2003, 145 pages.
- Cox, S. K., D. S. McDougal, D. A. Randall, R. A. Schiffer, 1987: FIRE-the first ISCCP Regional Experiment. *Bull. Amer. Meteor. Soc.*, **68** (2), 114-118.
- Cui, Z. M. Tjernström, and B. Grisogono, 1998: Idealized simulations of atmospheric flow along the central coast of California. *J. Appl. Meteor.*, **37**, 1332- 1363.
- Deardorff, J.W., 1972: Numerical investigation of neutral and unstable planetary boundary layers. *J. Atmos. Sci.*, **29**, 91-115.
- Deardorff, J. W., 1976: On the entrainment rate of a stratocumulus-topped mixed layer. *Quart. J. Roy. Meteor. Soc.*, **102**, 563-582.
- _____, 1980: Cloud top entrainment instability. *J. Atmos. Sci.*, **37**, 131-147.
- Dorman C. E., T. Holt, D. P. Rogers and K. Edwards, 2000: Large-scale structure of the June-July 1996 marine boundary layer along California and Oregon. *Mon. Weather. Rev.* **128** (6): 1632-1652.
- Fiedler, B. H., 2002: Grid Adaptation and its effect on entrainment in an E-I model of the atmospheric boundary layer. *Mon. Wea. Rev.*, **130**, 733-740.
- Fritz, S., P. Kollias, and B. A. Albrecht, 2001: Drizzle Characteristics from a surface-based 94 GHz radar. 30th International Conference on Radar Meteorology, AMS, Munich, Germany, 19-25 July 2001.
- Grenier, H. and C. S. Bretherton, 2001: A moist PBL parameterization for large-scale models and its application to subtropical cloud-topped marine boundary layers. *Mon. Wea. Rev.*, **129** (3), 357-377.
- Haack, T. and S. D. Burk, 2001: Summertime marine refractivity conditions along coastal California. *J. Appl. Meteor.*, **40**, 673- 687.
- Hilliker, J. L. and J. M. Fritsch, 1999: An observations-based statistical system for warm-season hourly probabilistic forecasts of low ceiling at the San Francisco International Airport. *J. Appl. Meteor.*, **38**, 1692- 1705.
- Hodur, R.M., 1997: The Naval Research Laboratory's Coupled Ocean/Atmosphere Mesoscale Prediction System (COAMPSTM). *Mon. Wea. Rev.*, **125**, 1414-1430.

- Holtzlag, A. A. M., and B. A. Boville, 1993: Local versus non-local boundary layer diffusion in a global climate model. *J. Climate*, **6**, 1825-1842.
- Jiang H. L., G. Feingold, W. R. Cotton, 2002: Simulations of aerosol-cloud-dynamical feedbacks resulting from entrainment of aerosol into the marine boundary layer during the Atlantic Stratocumulus Transition Experiment. *J. Geophys. Res.-Atmos.* **107** (D24), AAC 20-1 – 20-11, art. no. 4813.
- Kain, J.S., and J.M. Fritch, 1990: A one-dimensional entraining/detraining plume model and its application in convective parameterization. *J. Atmos. Sci.*, **35**, 1070-1096.
- Kalogiros J. A. and Q. Wang, 2001: The California low-level coastal jet and nearshore stratocumulus. Fourth Conference on Coastal Atmospheric and Oceanic Prediction. AMS November 6 – 9, 2001, St. Petersburg, FL.
- Kalogiros J. A. and Q. Wang, 2002: Calibration of a radome-differential GPS system on a twin otter research aircraft for turbulence measurements. *J. Atmos. Ocean Tech.* **19**: 159-171.
- Khairoutdinov, M. and Y. Kogan, 2000: A new cloud physics parameterization in a Large-Eddy Simulation model of marine stratocumulus. *Mon. Wea. Rev.*, **128**, 229-243.
- Kindle J. C., R. M. Hodur, S. deRada, J. D. Paduan, L. K. Rosenfeld, and F. Q. Chavez, 2002: A COAMPSTM (TM) reanalysis for the Eastern Pacific: Properties of the diurnal sea breeze along the central California coast. *Geophys. Res. Lett.* **29** (24), AAC 56-1 – 56-4, art. No. 2203.
- Klein, S. A., and D. L. Hartmann, 1993: The seasonal cycle of low stratiform cloud. *J. Climate*, **6**, 1587-1606.
- Kollias, P. and B. Albrecht, 2000: The turbulence structure in a continental stratocumulus cloud from millimeter-wavelength radar observations. *J. Atmos. Sci.* **57**, 2417-2434.
- Kong F.-Y., 2002: An experimental simulation of a coastal fog-stratus case using COAMPSTM model. *Atmos. Res.* **64**, 205-215.
- Konor, C. S. and A. Arakawa, 2001: Incorporation of moist processes and a PBL parameterization into the generalized vertical coordinate model. Technical Report **102**, University of California Los Angeles, Department of Atmospheric Sciences, UCLA, Box 951565, Los Angeles CA 90095-1565, 63pp.
- Koracin D., C. E. Dorman, 2001: Marine atmospheric boundary layer divergence and clouds along California in June 1996. *Mon. Weather Rev.* **129** (8), 2040-2056.

- Koracin D, J. Lewis, W. T. Thompson, C. E. Dorman, and J. A. Businger, 2001: Transition of stratus into fog along the California coast: Observations and modeling. *J. Atmos. Sci.* **58** (13), 1714-1731.
- Leidner, S. M., D. R. Stauffer, and N. L. Seaman, 2001: Improving short-term numerical weather prediction in the California coastal zone by dynamic initialization of the marine boundary layer. *Mon. Wea. Rev.*, **129**, 275- 294.
- Lenderink, G., and A. A. M. Holtslag, 2000: Evaluation of the kinetic energy approach for modeling turbulent fluxes in stratocumulus. *Mon. Wea. Rev.*, **128**, 244-258.
- Lenschow, D. H., I. R. Paluch, A. R. Bandy, R. Pearson, S. R. Kawa, C. J. Weaver, B. J. Huebert, J. G. Kay, D.C. Thornton, A. R. Driedger, 1988: Dynamics and Chemistry of Marine Stratocumulus (DYCOMS) Experiment. *Bull. Amer. Meteor. Soc.*, **69**, 1058–1058.
- Lilly, D. K., 1968: Models of cloud-topped mixed layers under a strong inversion. *Quart. J. Roy. Meteor. Soc.*, **94**, 292-309
- _____, 2002a: Entrainment into mixed layers. Part I: Sharp-edged and smoothed tops. *J. Atmos. Sci.* **59** (23), 3340-3352.
- _____, 2002b: Entrainment into mixed layers. Part II: A new closure.. *J. Atmos. Sci.* **59** (23), 3353-3361.
- Lock, A. P., and M. K. MacVean, 1999: The parameterization of entrainment driven by surface heating and cloud-top cooling. *Quart. J. Roy. Meteor. Soc.*, **125**, 271-299.
- _____, A. R. Brown, M. R. Bush, G. M. Martin, and R. N. B. Smith, 2000: A new boundary layer mixing scheme. Part II: Tests in climate and mesoscale models. *Mon. Wea. Rev.*, **128**, 3200–3217.
- _____, 2001: The numerical representation of entrainment in parameterizations of boundary layer turbulent mixing. *Mon. Wea. Rev.*, **129**, 1148-1163
- Lock, A. P. 2000: A new boundary layer mixing scheme. Part I: Scheme description and single-column model tests. *Mon. Wea. Rev.*, **128**, 3187–3199.
- Louis, J.F., M. Tiedtke and J.F. Geleyn, 1982: A short history of the operational PBL parameterization at ECMWF. *Workshop on Planetary Boundary Parameterization, ECMWF, Reading*, 59-79. (Available from the European Center for Medium Range Weather Forecasts, Shinfield Park, Reading RG2 9Ax, U.K.)
- _____, 1979: A parametric model of vertical eddy fluxes in the atmosphere. *Bound.-Layer Meteor.*, **17**, 187-202.

- Lu, R. and R. P. Turco, 1994: Air pollutant transport in a coastal environment 1. 2-dimensional simulations of sea-breeze and mountain effects. *J. Atmos. Sci.* **51** (15), 2285-2308.
- Martin, G. M., M. R. Bush, A. R. Brown, A. P. Lock, and R. N. B. Smith, 2000: A new boundary layer mixing scheme. Part I: Scheme description and single-column model tests. *Mon. Wea. Rev.*, **128**, 3187–3199.
- McCaa, J. R. and C. S. Bretherton, 2004: A new parameterization for shallow cumulus convection and its application to marine subtropical cloud-topped boundary layers. Part II: Regional simulations of marine boundary layer clouds. *Mon. Wea. Rev.* **132**, 883-896.
- Mechem, D. B., and Y. L. Kogan, 2003: Simulating the transition from drizzling marine stratocumulus to boundary layer cumulus with a mesoscale model. *Mon. Wea. Rev.*, **131**, 2347-2360.
- Mellor, G., and Yamada, 1974: A hierarchy of turbulence closure models for planetary boundary layers. *J. Atmos. Sci.*, **31**, 1791-1806.
- _____, 1982: Development of a turbulence closure model for geophysical fluid problems. *Rev. of Geophys. and Space Phys.*, **20**, 851-875.
- Miller, D. K., D. L. Walters, and A. Slavin, 2001: Evaluation of a turbulent mixing length parameterization applied to the case of an approaching upper-tropospheric trough. Ninth Conference on Mesoscale Processes. AMS July 30 –August 2, 2001, Ft. Lauderdale, FL.
- Moeng, C.-H., 1976: A large-eddy simulation for the study of planetary boundary layer turbulence. *J. Atmos. Sci.*, **41**, 2052-2062.
- _____, P. P. Sullivan, and B. Stevens, 1999: Including radiative effects in an entrainment-rate formula for buoyancy driven PBLs. *J. Atmos. Sci.*, **56**, 1031–1049.
- _____, 2000: Entrainment Rate cloud fraction, and liquid water path of PBL Stratocumulus clouds. *J. Atmos. Sci.*, **57**, 3627-3643.
- Nuss, W. A., P.E. Mantey, A. Pang, and D. D. E. Long, 1996: The Real-Time Environmental Information Network and Analysis System (REINAS), Preprints 12th Conference on Interactive Information and Processing Systems (IIPS) for Meteorology, Oceanography and Hydrology, Atlanta, February (1996).

- Paluch, I. R, and D. H. Lenschow, 1991: Stratiform cloud formation in the marine boundary layer. *J. Atmos. Sci.*, **48**, 2141-2158.
- Penner, J. E. and Co-authors, 2001: Aerosols, their direct and indirect effects. In: Climate Change 2001: The Scientific Basis. Contribution of Working Group I to the Third Assessment Report of the Intergovernmental Panel on Climate Change. Houghton, J.T., Y. Ding, D.J. Griggs, M. Noguer, P.J. van der Linden, X. Dai, K. Maskell, and C.A. Johnson (eds.). Cambridge University Press, Cambridge, United Kingdom and New York, NY, USA, 881pp.
- Rados, K, Q. Wang, J. Kalogiros, S. Wang, D. Khelif, and C. Friehe 2002: Evaluation of marine boundary layer parameterizations in COAMPS using the JES experiment data set. Fifteenth Symposium on Boundary Layers and Turbulence. AMS July 15 – 19, 2002, Wageningen, NT.
- Ralph, F. M., L. Armi, J. M. Bane, C. E. Dorman, W. D. Neff, P. J. Neiman, W. Nuss, and P. O. G. Persson, 1998: Observations and analysis of the 10–11 June 1994 coastally trapped disturbance. *Mon. Wea. Rev.*, **126**, 2435–2465.
- Randall, D. A., 1980: Conditional instability of the first kind upside-down. *J. Atmos. Sci.*, **37**, 125-130.
- Stevens D. E. and C. S. Bretherton, 1999: Effects of resolution on the simulation of stratocumulus entrainment. *Q. J. Roy. Meteor. Soc.*, **125 B** (554), 425-439.
- Stevens, B. 2002: Entrainment in Stratocumulus Topped Mixed Layers. *Quart. J. Roy. Meteor. Soc.*, **128 B** (586), 2663-2690.
- _____, and Coauthors, 2003a: Dynamics and Chemistry of Marine Stratocumulus DYCOMS-II. *Bull. Amer. Meteor. Soc.*, **84** (5), 579-594.
- _____, D.H. Lenschow, I. Faloona, C-H. Moeng, D.K. Lilly, B. Blomquist, G. Vali, A. Bandy, T. Campos, H. Gerber, S. Haimov, B. Morely, and D. Thorton, 2003b: On Entrainment Rates in Nocturnal Marine Stratocumulus. *Quart. J. Roy. Meteorol. Soc.*, **129 B** (595), 3469-3493.
- Stull, R.B., 1988: *An Introduction to Boundary Layer Meteorology*. Kluwer Academic Publishers, 666 pp.
- Therry, G. and P. LaCarrère, 1983: Improving the kinetic energy model for planetary boundary layer description. *Bound.-Layer Meteor.*, **25**, 63-88.
- Thompson, W. T., 2002: COAMPS™ PBL and surface parameterizations. COAMPS™ Training and Workshop, 4-6 September 2002, Naval Research Laboratory, Monterey, CA.

- Turton, J. D. and S. Nicholls, 1987: A study of the diurnal variation of stratocumulus using a multiple mixed layer model, *Quart. J. Roy. Meteor. Soc.*, **113**, 969-1009.
- Twomey, S., 1977: The influence of pollution on the short wave albedo of clouds. *J. Atmos. Sci.*, **34**, 1149-1152.
- van Meijgaard, E., and A. P. van Ulden, 1998: A first-order mixing condensation scheme for nocturnal stratocumulus. *Atmos. Res.*, **45**, 253–273.
- Wang, S. and Q. Wang, 1994: Roles of drizzle in a one-dimensional third-order turbulence closure model of the nocturnal stratus-topped marine boundary layer. . *J. Atmos. Sci.*, **51**, 1559-1576.
- Wang, Q., 2002: Evaluation of surface flux and boundary layer parameterizations in COAMPS™ using aircraft observations. Naval Research Laboratory 6.2 Review, 13-15 March 2002, Monterey, CA.
- Wetzel, M. A., W. T. Thompson, G. Vali, S. K. Chai, T. Haack, M. J. Szumowski, and R. Kelly, 2001: Evaluation of COAMPS™ forecasts of coastal stratus using satellite microphysical retrievals and aircraft measurements. *Wea. Forecasting*, **16**, 588-599.
- Whisenant, M. K., 2003: Turbulence parameterizations for convective boundary layers in high-resolution mesoscale models. Ph.D. Dissertation, 148 pp., Dept. of Meteorology, Naval Postgraduate School, Monterey, CA.

THIS PAGE INTENTIONALLY LEFT BLANK

INITIAL DISTRIBUTION LIST

1. Defense Technical Information Center
Ft. Belvoir, Virginia
2. Dudley Knox Library
Naval Postgraduate School
Monterey, California
3. Dr. Qing Wang
Department of Meteorology
Naval Postgraduate School
Monterey, California
4. Dr. Carlyle H. Wash
Department of Meteorology
Naval Postgraduate School
Monterey, California
5. Dr. Wendell Nuss
Department of Meteorology
Naval Postgraduate School
Monterey, California
6. Dr. Douglas Miller
Department of Meteorology
Naval Postgraduate School
Monterey, California
7. Dr. Peter C. Chu
Department of Oceanography
Naval Postgraduate School
Monterey, California
8. Dr. Shouping Wang
Naval Research Laboratory
Monterey, California
9. Dr. Don Walters
Department of Physics
Naval Postgraduate School
Monterey, California

10. Dr. Sue Chen
Naval Research Laboratory
Monterey, California
11. Dr. Stephan R. de Roode
Institute for Marine and Atmospheric Research Utrecht
Utrecht, The Netherlands
12. LCDR Daniel P. Eleuterio
546 Port Harwick
Cula Vista, CA 91913